The Dissertation Committee for Bruce Child Frederick Certifies that this is the approved version of the following dissertation:

Submarine Sedimentary Basin Analyses for the Aurora and Wilkes Subglacial Basins and the Sabrina Coast Continental Shelf, East Antarctica

Committee:

Donald D. Blankenship, Supervisor

Ian W. D. Dalziel

Sean P. S. Gulick

Clark R. Wilson

Duncan A. Young

Submarine Sedimentary Basin Analyses for the Aurora and Wilkes Subglacial Basins and the Sabrina Coast Continental Shelf, East Antarctica

by

Bruce Child Frederick, B.A, M.S.

Dissertation

Presented to the Faculty of the Graduate School of

The University of Texas at Austin

in Partial Fulfillment

of the Requirements

for the Degree of

Doctor of Philosophy

The University of Texas at Austin
August 2015

Dedication

To my family: parents John and Laverne Frederick; and my sister Paige Frederick-Pape. I could never have completed this herculean task without your ceaseless love and support!

Acknowledgements

While life is a journey of education and experience there are scant moments where you find the time to slow down enough to thank those who have contributed to your success. Perhaps we often do not take the time as it remains a daunting task identifying individuals who served as positive role models in life while providing their friendship and knowledge so selflessly. That said, in advance, if I have overlooked anyone along the way I do apologize.

As with any child, lifelong success depends primarily on a solid ethical, loving foundation and for that I owe my immediate family more than I can ever repay in kind. To my parents John and Laverne Frederick, and my sister Paige Frederick-Pape and her husband Brian Pape, I would have never been able to complete this journey without your love and support along the way! Often unsung, but certainly not forgotten, are many teachers and mentors from my childhood upbringing on St. Croix, USVI. Exceptional Good Hope School teachers included Ms. Marty Savard and Ms. Martha Dumican who provided me the mathematical and literature foundation to pursue ever advanced collegiate degrees. Other Crucian characters and longtime friends are to be commended including a multitude of neighbors who quickly became extended family as I grew up thousands of mile away from my cousins, aunts , and uncles, (namely the Bulls, Bothes, Suhs, Rubishs, Lockwoods, Petkes, Lawaetzs, Maults, and Woods), and especially Capt. Rudy Harvey who fostered my love and respect for the ocean while guiding me through adolescence and into adulthood.

Coincidentally, had it not been for two exceptional oceanography professors at Colgate University (Drs. Paul Pinet and Charles McClennen), I might never have become a geologist, go on to pursue the PhD in geophysics, or explore the Antarctic continent several times over. I would not be where I am today without the support and guidance of many in the Colgate University Geology Department including notably Drs. Bruce Selleck and Jim McLelland who wrote many a reference letter and always fostered a love of science encouraging me to take roads less travelled. Along the way, these scientific journeys introduced me to others in the field of Antarctic science whose friendship and expertise will endure long after my University of Texas-Austin tenure; Drs. Eugene Domack and Amy Leventer of University of South Florida and Colgate University, respectively, have gone above and beyond the call with regard to selflessly supporting and encouraging my scientific endeavors throughout my career.

Naturally, and most notably, I want to thank my supervisor and friend, Dr. Don Blankenship. Don saw potential in me long before anyone else at UT did, and demonstrated incredible patience and understanding through what was to be a personally challenging first year of graduate school for me. In addition, I want to personally thank each of my examining and dissertation committee members including Drs. Ian Dalziel, Sean Gulick, Duncan Young, and Clark Wilson. I will always be grateful for your mentorship and guidance through the years and for your ceaseless encouragement to test and retest hypotheses in order to produce the most comprehensive scientific assessment of the Wilkes Land sedimentary basins, both subglacial and submarine.

I am also especially grateful to academic colleagues and friends across the US and Australia, from Dr. Alan Aitken providing exceptional expertise with respect to conjugate margin geology and geophysical response, to Mr. David Gwyther for selflessly offering friendship and physical oceanographic expertise including constraints along the Sabrina Coast, and to Dr. Rodrigo Fernandez whose friendship and expertise in high-latitude glacial marine geology proved incomparable during my assessment of the region. All were willing to share resources and collaborate on NSF proposals in working toward a more comprehensive understanding of Wilkes Land geology under the Antarctic icecap and ocean. A special thanks as well to countless others at UTIG who served as collaborators and/or mentors along the way, particularly: Scott Kempf, Dan Duncan, Mark Wiederspahn, Joseph Yeh, Philip Guerrero, Marcy Davis, Stephen Saustrup, and Thomas Richter. Our conversations not only assisted my research endeavors, but also helped shape my continued personal and professional development. Thank for you for ever-open doors!

Special thanks to my fellow graduate students for their support, camaraderie and solutions provided toward the consistent series of struggles and confusions along the way. Through life's journeys, I can honestly say that I am honored to have encountered the following friends along the way including those that left the largest impact: Russell Carter, Terence Campbell, Tricia Alvarez, Brad Gooch, Jamin Greenbaum, Marie Cavitte, Enrica Quartini, Chad Greene, and Gail Gutowski.

Submarine Sedimentary Basin Analyses for the Aurora and Wilkes Subglacial Basins and the Sabrina Coast Continental Shelf, East Antarctica

Bruce Child Frederick, Ph.D.

The University of Texas at Austin, 2015

Supervisor: Donald D. Blankenship

This dissertation focuses on the Wilkes Land region of the East Antarctic Ice Sheet (EAIS) that is predominantly characterized by two large subglacial basins, the Aurora Subglacial Basin (ASB) to the east and the Wilkes Subglacial Basin (WSB) to the west and immediately adjacent to the Transantarctic Mountains (TAM). The ASB and WSB are expansive covering an estimated 750,000 and 980,000 square kilometers, respectively. In addition, their bedrock geometry places them an average of 1.25 km below present day sea level, raising the possibility of fundamental instability through grounding line retreat.

Subglacial sediment deformation has long been known to facilitate faster ice flow and significantly impact basal ice conditions including geothermal heat flux, groundwater flow, and frictional heat flux. Recently acquired aerogeophysical data over the interior ASB and WSB document extensive subglacial sedimentary basins that can be distinguished as smaller subbasins, each associated with adjacent topographic highlands and EAIS dynamics. The volumes of these interior subglacial subbasins vary between 26,349 +/- 10,885 km^3 and 398,082 +/- 164,454 km^3 in the ASB and 7,188 +/- 2,940 km^3 and 128,094 +/- 52,399 km^3 in the WSB (based upon 20% porosity values). Notably, the character of the basins varies substantially between the more southern ASB and WSB interiors and the more marginal, northern ASB and WSB reflective of different dynamic ice histories across geologic time.

ASB sedimentary basin volumes, derived from airborne gravity and magnetic data with ice-penetrating radar constraints, are contrasted with recently acquired high-resolution marine seismic sequence stratigraphy collected on the Sabrina Coast continental shelf. With targeted geologic sampling of outcropping strata, megasequence sediment volumes are estimated for a finite area adjacent to the Totten Glacier/Moscow University Ice Shelf catchment draining the ASB interior. Preglacial, temperate/polythermal glacial, and polar glacial sediment volumes of 278.6 +/- 148.8 km^3, 570.6 +/-51.9 km^3, and 1,658 +/- 389 km^3, respectively, combined with a multitude of diagnostic glacial tunnel valleys, unconformities, and geologic data, reinforce recent dynamic Pliocene EAIS hypotheses for the Wilkes Land margin.

Table of Contents

List of Tables

List of Figures

Chapter 1: Introduction

1.1 MOTIVATION AND OBJECTIVES

Improving the accuracy of global climate change models ultimately depends on accurately quantifying basal ice constraints in the cryosphere. Subglacial sediment has long been recognized to motivate faster ice flow and modulate geothermal heat flux to basal ice [*Blankenship et al.*, 1986; *Siegert and Dowdeswell*, 1996]]. With a prominent increase in anthropogenic CO_2 emissions since the 1950s [*IPCC*, 2013], there is increased scrutiny on the efficiency and accuracy of global climate models to replicate polar ice dynamics across geologic time with changes in climate and ocean forcing stimuli.

Cryospheric regions particularly susceptible to runaway retreat due to climate change forcing include basins with grounded ice below sea level and interior-sloping bed configurations. While West Antarctica has long been recognized and well-studied for its characteristic submarine-based ice sheet with 3.3 m of equivalent sea level rise [*Bamber et al.*, 2009], the expansive Wilkes and Aurora subglacial basins in Wilkes Land, East Antarctica with similar bed conditions have had only limited aerogeophysical coverage since the advent of global positioning systems (GPS) leading to significant variability in eustatic estimates from this region ranging from 3 to 14 m [*Hill et al.*, 2007; *Pollard and DeConto*, 2009; *Cook et al.*, 2013; *Gomez et al.*, 2010]].

Estimating the character, distribution and thickness of subglacial sedimentary basins in the Wilkes and Aurora Subglacial Basins using aerogeophysical datasets across a geographic expanse exceeding 5,425,000 km^2 with an average icecap thickness exceeding 2.5 km and no geologic outcrops in the study area for corroboration was a significant challenge. Workflows were developed using multiple aerogeophysical datasets to isolate potential field sources for the Wilkes Land interior basins such that 3D sedimentary basin isopachs could be estimated. To help constrain the inherently non-unique airborne potential field inversion process, sedimentary basin models of the interior Wilkes and Aurora Subglacial Basins were examined relative to marine geophysical and geologic data collected on the Sabrina Coast continental shelf. Established climate and dynamic ice hypotheses for the Wilkes Land region are now evaluated against the resultant interior subglacial sedimentary isopach models and the high resolution sequence stratigraphic record of the Wilkes Land continental shelf for the first time.

1.2 STRUCTURE OF THE DISSERTATION

This dissertation is organized into a series of publication-submitted and publication-ready manuscripts addressing the aforementioned objectives, with the exception of Chapter 2 which presents the study area and the datasets used in this dissertation. The geologic history of Wilkes Land, East Antarctica is introduced in detail, including shared history with the South Australian conjugate margin and the evolution of the East Antarctic Ice Sheet (EAIS). Historical aerogeophysical datasets in addition to more recent University of Texas-Austin Institute for Geophysics (UTIG) sponsored surveys such as *Investigating the Cryospheric Evolution of the Central Antarctic Plate* (ICECAP) and IceBridge are reviewed in conjunction with data from the most recent interdisciplinary 2014 RVIB *Nathaniel B. Palmer* Totten Glacier System and Marine Record of Cryosphere-Ocean Dynamics cruise with research scientists from UTIG, Colgate University, University of South Florida (USF), Lamont Doherty Earth Observatory (LDEO), Texas A&M University (TAMU), University of Aveiro, and Geoscience Australia.

Chapter 3 presents the first subglacial sedimentary basin isopachs for the Aurora Subglacial Basin (ASB) derived using inverse aerogeophysical techniques [Frederick et al., (in review) *Journal of Geophysical Research*]. Workflow methodologies are established to process datasets and reduce noise while vertically and laterally constraining the model. This chapter isolates key components of the airborne gravity signal, determines magnetic depth to basement (DTB), examines subglacial topographic roughness, and finally establishes an iterative 2D methodology to determine subglacial sedimentary basin character in three dimensions. Implications for existing fluvial, temperate/polythermal-glacial, and polar-glacial hypotheses are discussed.

Chapter 4 presents the first subglacial sedimentary basin isopachs for the Wilkes Subglacial Basin (WSB) derived using inverse aerogeophysical techniques collected during 3 different surveys over the course of 15 years [Frederick et al., (pending coauthor review) Earth and Planetary Science Letters]. Prior to implementing the previously-established ASB aerogeophysical data workflow, the WSB aerogeophysical datasets had to be preprocessed including the establishment of a common map projection, instrument elevation, and sampling interval. This chapter establishes topographic, lithospheric, and structural contributions to the gravitational response, defines magnetic DTB for vertical model constraint, isolates subglacial basin topographic roughness for lateral model constraint, and finally presents the resultant 3D subglacial sedimentary isopach solution. Implications for existing WSB dynamic ice models are discussed.

Chapter 5 investigates ASB-derived sediment presently deposited in sequence on the Sabrina Coast continental shelf [Frederick et al., (pending coauthor review) Geochemistry, Geophysics, Geosystems]. Three primary megasequences are described based on their inherent sequence stratigraphy and related depositional facies. Interpretation of the first high-resolution multichannel seismic (MCS) actively shot on the Sabrina Coast continental shelf, proximal to the Moscow University Ice Shelf (MUIS), Totten Glacier and Reynolds Trough, is supported by initial sedimentological and paleontological information from shallow, targeted geologic cores collected at key stratigraphic outcrops on the seafloor. Structure contour and isopach maps are presented for key horizons and sequences. Swath multibeam bathymetry and marine gravity data are utilized to constrain the seafloor topography and basement surfaces (where not evident in MCS records), respectively. A 3D structural model is developed to estimate sediment volumes for the three megasequences representing fluvial, temperate/polythermal-glacial and polar-glacial facies. Depositional sequences are discussed relative to existing hypotheses concerning EAIS-related glacial dynamics since the Oligocene.

Chapter 6 discusses the overall conclusions of the dissertation and presents additional avenues for future work. Initial results showed that Wilkes Land subglacial sedimentary basins can be divided into smaller subbasins with distinct sediment thicknesses and distributions characteristic of the ice sheet dynamics of the particular basin. Interior subbasins are generally characterized by more substantial sedimentary deposits resulting from longer-term dynamic temperate/polythermal alpine glaciation associated with adjacent highlands. Hydraulically downgradient subbasins proximal to the current ice sheet margin are generally more sediment starved with substantial deposits restricted to subglacial fjords and troughs potentially evident of more channelized subglacial hydraulics [*Schroeder et al.*, 2013] and/or more frequent EAIS advance-retreat cycles through the Plio-Pleistocene [*Cook et al.*, 2013; *Mengel and Levermann*, 2014] than has previously been hypothesized for the ASB.

Chapter 2: History of Wilkes Land Study Area

2.1 STUDY AREA LOCATION

East and West Antarctica, identified based upon hemisphere (Figure 2.1), are each covered by one contiguous ice cap containing some 98% of the Earth's fresh water accounting for approximately 70 meters of sea level rise [*Williams and Hall*, 1993]. Despite the vast expanse of the present-day 26.5×10^6 km^3 ice sheet, each hemisphere has maintained significantly disparate geologic and glaciologic histories. While the West Antarctic hemisphere has long garnered the focus of scientific investigations with its characteristic marine ice sheet grounded mostly below sea level [*Bentley*, 1964; *Drewry*, 1983; *Lythe and Vaughan*, 2001; *Fretwell et al.*, 2013], the East Antarctic ice sheet was often considered glaciologically static and perhaps less relevant to eustatic fluctuations since the mid-Neogene.

However with observations illustrating a potentially more dynamic EAIS [*Young et al.*, 2011], scientific focus has shifted to two large Wilkes Land submarine basins (Figure 2.2) to the west of the Transantarctic Mountains (TAM), namely the WSB and ASB. Complex ice flow model algorithms depend substantially on accurate representations of basal ice dynamics for which data has been historically scarce across the ASB and WSB due to the remoteness much of this area of Wilkes Land. To best comprehend the basal conditions beneath an average of 2.5 km of EAIS ice in this region, I began by analyzing the subglacial geology and tectonic history of East Antarctica and specifically the ASB and WSB regions in particular.

Figure 2.1: Antarctica Topographic Contour Map showing East and West and Antarctic hemispheres and the Study Area location (http://lima.nasa.gov). Elevation contours shown at 500 m interval.

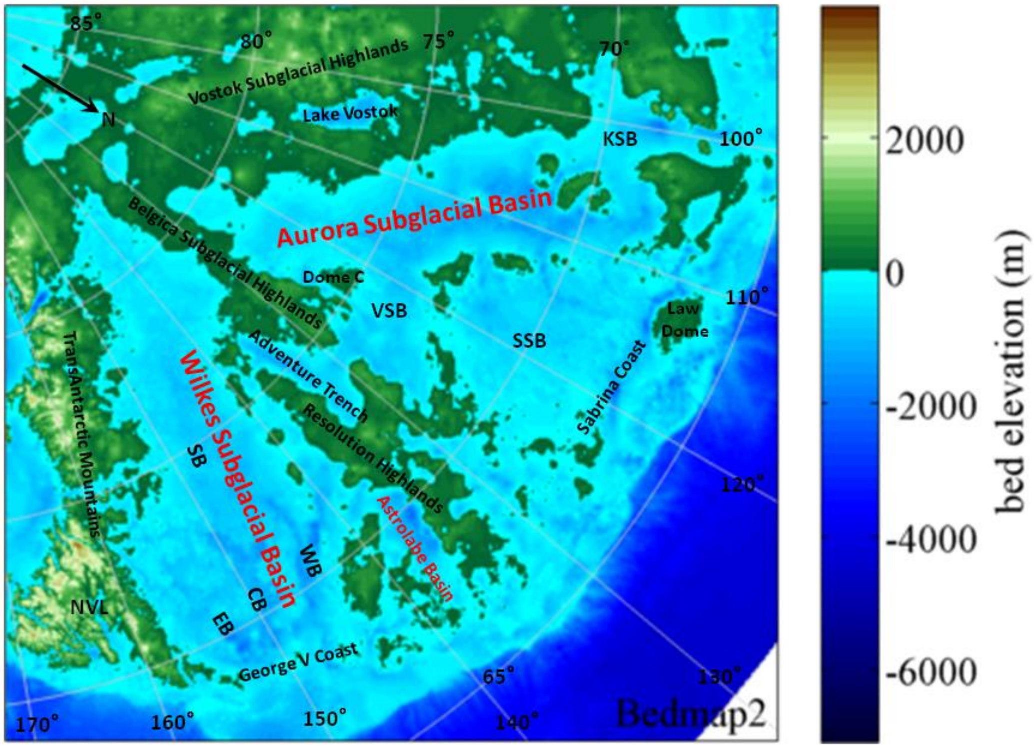

Figure 2.2: Wilkes Land bedrock topography [*Fretwell et al.*, 2013]. Antarctica coastline includes ice shelves. Major bedrock features labeled including: WSB=Wilkes Subglacial Basin; SB=Southern Basin; WB=Western Basin; CB=Central Basin; EB=Eastern Basin; NVL=North Victoria Land.

2.2 WILKES LAND TECTONIC HISTORY – PRECAMBRIAN TO PRESENT

The Wilkes Land region of the East Antarctic craton, from Law Dome to North Victoria Land, share common ancestry as part of East Gondwana where present day East Antarctica butted against Southern Australia. Specifically, the Gawler Craton (South Australia) and the Terre Adelie Craton (East Antarctica) represented fragments of a larger, ancient continental block called the Mawson Continent [*Fanning et al.*, 1999], that shared geologic similarities including Archaean (> 2.4 Ga) and Proterozoic (2.0-1.7 Ga) basement and basins [*Peucat et al.*, 1999].

2.2.1 Precambrian to Early Mesozoic

From 1.1 Ga, East Antarctica and Australia (as part of East Gondwana) had a similar tectonic history [*Veevers*, 2000] remaining coupled as Laurentia separated. All continents subsequently reassembled by 550 Ma to form Pangaea. However, the relict lithospheric sutures established during major Precambrian magmatic and metamorphic activities (the last major thermal event affecting the Mawson Continent), ultimately contributed to the location and development of a rift system in central Gondwanaland (Figure 2.3).

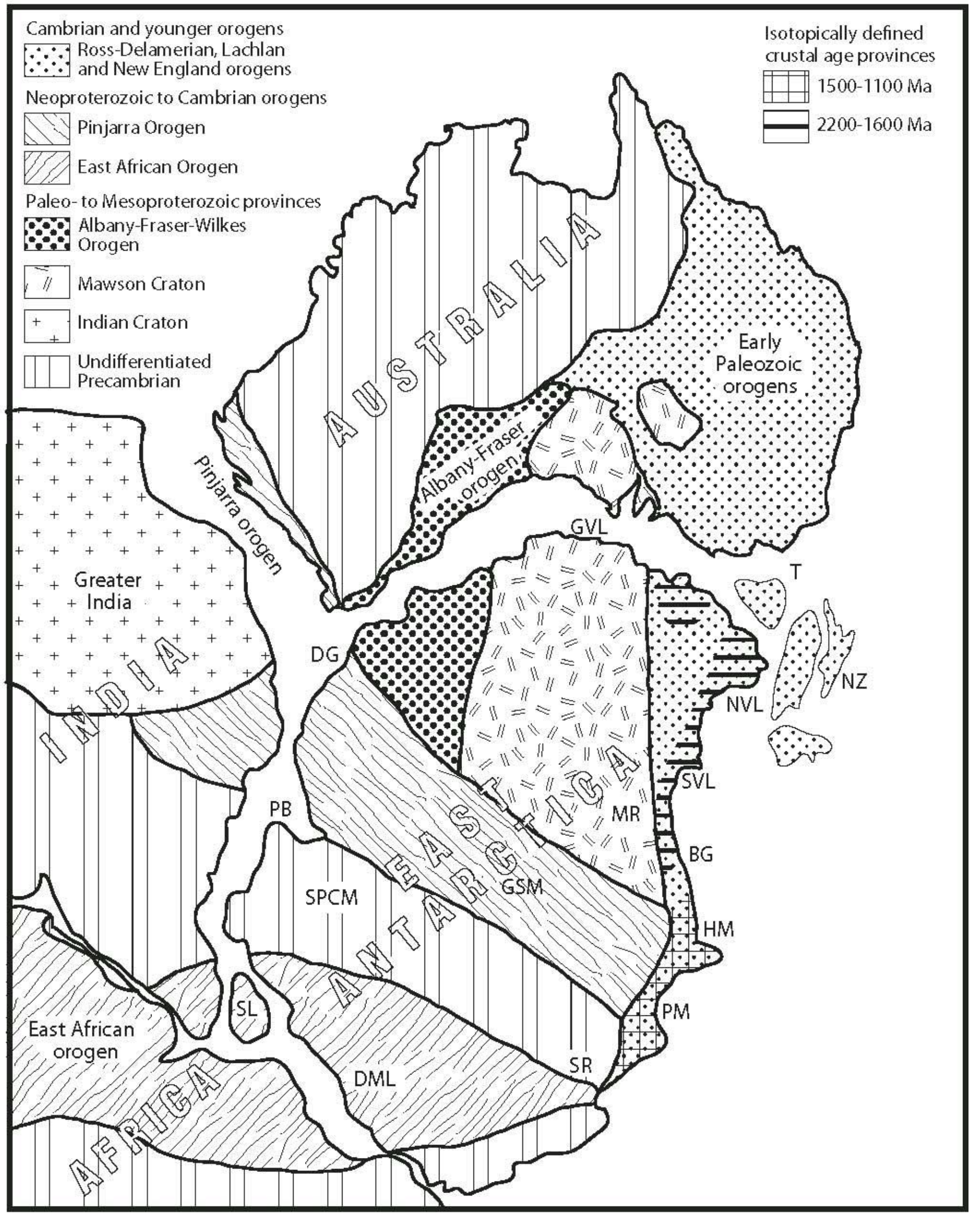

Figure 2.3: Map of East Antarctica in a Gondwana reconstruction (after Fitzsimons, 2003), showing ages of shields and orogens . BG=Beardmore Glacier, DG=Denman Glacier, GVL=George V Land, DML=Dronning Maud Land, HM=Horlick Mountains, MR=Miller Range, NZ=New Zealand, PB=Prydz Bay, PM=Pensacola Mountains, SL=Sri Lanka, SPCM=Southern Prince Charles Moutains, SR=Shackleton Range, SVL=Southern Victoria Land, T=Tazmania [*Goodge*, 2007].

The cause of separation of East and West Gondwana remains enigmatic. A potential link between large igneous Mesozoic-age provinces and Gondwana plate tectonic activity has been hypothesized due to the proximity of these igneous rocks to previously active plate boundaries and continental margins [*Storey et al.*, 2013]. Mantle magma plumes were either unroofed as a result of plate tectonic processes leading to continental separation [*White and McKenzie*, 1989] or were the cause of the Gondwana breakup [*Morgan*, 1971]. Many relict igneous provinces including continental and ocean basin flood basalts, giant dyke swarms, volcanic rifted margins, oceanic plateaus, ocean ridges, and seamount chains, were emplaced along crustal rift sutures (Figure 2.4) associated with the Marion, Kerguelen and Reunion mantle plumes in the Late Jurassic [*Lawver et al.*, 1992]. These impacted lithospheric structures would again play a critical role in the location and magnitude of subsequent extensional deformation [*van Wijk et al.*, 2008] acting as a precursor to the tectonic development of the present-day Wilkes Land subglacial basins.

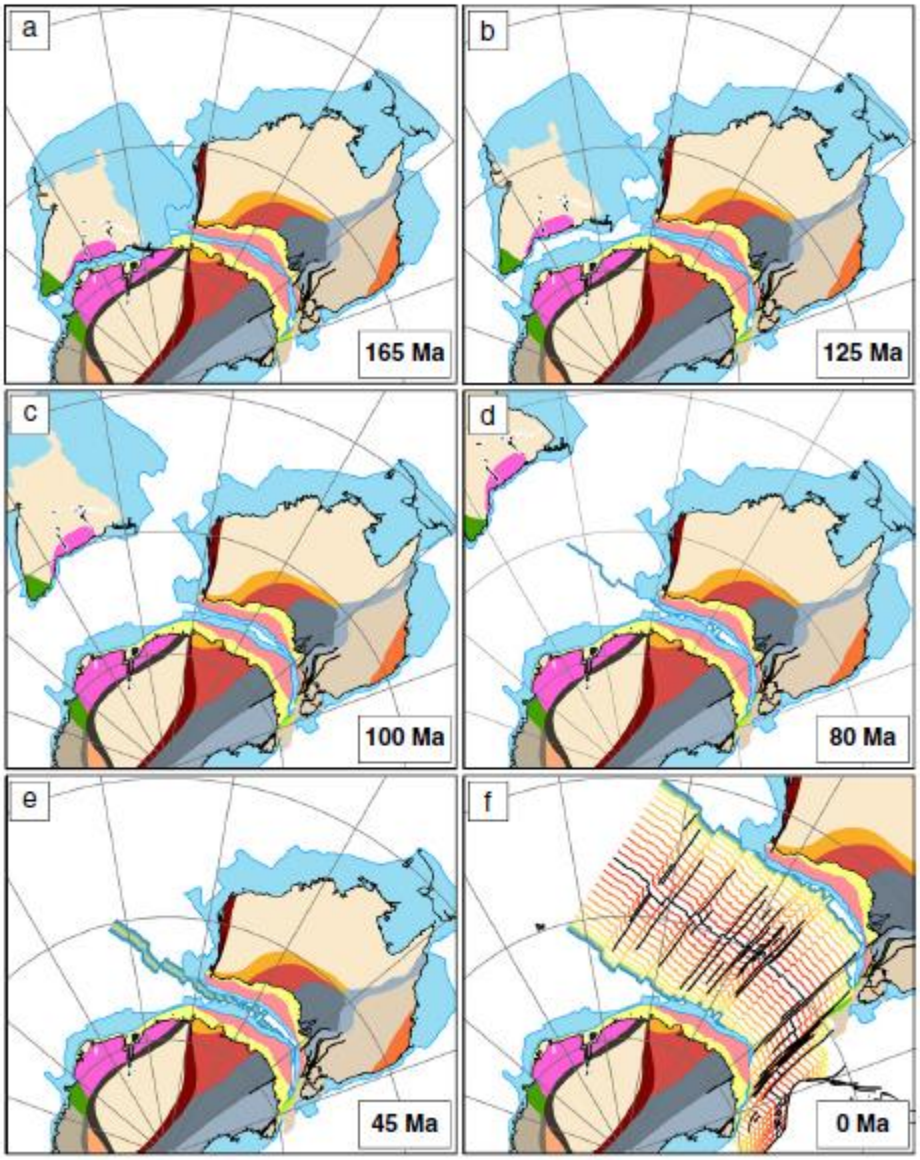

Figure 2.4: Reconstruction of Antarctica-Australia-India breakup from the initiation of rifting during the Late Jurassic (165 Ma) to Present [*White et al.*, 2013].

2.2.2 Jurassic to Paleogene

Jurassic to Early Cretaceous rifting and extension of the Wilkes Basin, in particular, led to crustal thinning and regional denudation of 2-3 km [*Lisker*, 2002]. By the late Cretaceous, sea floor spreading between Antarctica and Australia had commenced at a rate of about 5 mm/yr (half rate) as evidenced by magnetic anomalies in the Southern Ocean [*Tikku and Cande*, 1999]. This sea flooring spreading rate continued until the mid-Eocene when it increased to about 15 mm/yr, by the late Eocene the rate increased again to 24 mm/yr until the early Oligocene when the half rate sped up to 34 mm/yr [*Royer and Rollet*, 1997]. Kumar et al. [2007] proposed that the penetration of the lithospheric roots determined the rate of drift between continents during the breakup of Gondwanaland, with the thinnest continental crustal blocks achieving the greatest speeds.

Tectonic province boundaries trending perpendicular to the present-day Antarctic coastline are evidenced in Australia with the western Wilkes Land (in the vicinity of Casey Station) lithosphere comparable to the Albany-Fraser Orogen of Western Australia and the Terre Adelie basement comparable to the Gawler Craton of South Australia. Reading [2004] examined high-fidelity waveforms from teleseismic earthquakes to estimate the crustal thickness at Dumont D'Urville Station was 42 km with a significant low-velocity region in the deep crust, while the crustal thickness at Casey Station was 30 km with a fairly sharp Moho.

This late Cretaceous tectonic activity separating Australia and East Antarctica gave subsequent rise to additional extension in the West Antarctic Rift (WAR) system, causing the separation of the non-cratonic West Antarctica from the cratonic East Antarctica and prompting the thermodynamic uplift of the TAM in the early Eocene. Substantial episodic uplift pattern evidence from apatite fission-track data indicates denudation in the Early Cretaceous, Late Cretaceous, and Cenozoic separated by periods of relative tectonic stability [*Stump and Fitzgerald*, 1992]. These tectonic episodes would have undoubtedly impacted the formation of the hinterland basins immediately to the west, including the WSB and perhaps the ASB. Fitzgerald and Stump [1997] subsequently attributed the three TAM denudation episodes to regional tectonic events, specifically: 1) Early Cretaceous - southward translation of the Ellsworth-Whitmore Mountains block of West Antarctica relative to East Antarctica, 2) Late Cretaceous - extension in the Ross Embayment between East and West Antarctica, and 3) Eocene - rejuvenated faulting, magmatism, and deformation within the Victoria Land Basin.

This final episode of Eocene TAM tectonism occurred coincident with a major plate reorganization event (between 50-53 Ma) at Hawaii-Emperor bend time. By combining fracture zone and magnetic anomaly identifications, [*Whittaker et al.*, 2007] defined a new set of plate boundaries and computed finite rotations with 95% confidence intervals to describe an improved plate motion history between Australia and East Antarctica. They argue that these relative plate motion changes were initiated by the subduction of the Izanagi-Pacific ridge at 55 Ma that then caused forces acting on the Pacific plate to change from ridge-push to slab-pull. It was this change in Pacific plate motion that then caused the cessation of Tasman Sea spreading at 52 Ma and increased slab pull north of Australia such that Australia began to drift due north (as opposed to NW) away from East Antarctica.

2.2.3 Late Eocene to Present

By the late Eocene, the culmination of the East Gondwana fragmentation events during the Cenozoic and the evolution of the circum-Antarctic seaway would have profound climatic and geomorphologic impacts on the ASB, WSB, and adjacent East Antarctic basins. Two prominent tectonic events in the Paleogene had dramatic climatic impacts globally; the first such event occurred in the mid to late-Eocene with the closure of the equatorial Tethys Seaway. The closure of the Tethys had the effect of cooling global oceanic (and hence atmospheric) temperatures by diverting warmer westward oceanic circulation south of Africa (45° South).

The second set of significant tectonic events in the Paleogene occurred with the opening of the Australian-Antarctic seaway about 30 Ma, particularly the detachment of the South Tasman Rise from the margin of East Antarctica, and the opening of the Drake Passage. Both tectonic events were major factors in the development of the Antarctic Circumpolar Current (ACC) that prompted the thermal isolation of East Antarctica [*Kennett et al.*, 1974], and the late-middle Miocene expansion of the East Antarctic ice sheet. There is some evidence to suggest that there was in fact a shallow to mid-level seaway (approximate 1 km depth) across the South Tasman Rise as early as 50 Ma, however ocean bathymetry did not exceed the 2 km depth required for significant ACC development and climate change until the mid-Oligocene [*Lawver and Gahagan*, 2003].

Through the Neogene and Quaternary, the geomorphology of the ASB, WSB and surrounding Wilkes Land subglacial basins was more significantly impacted by the formation of ephemeral to permanent ice caps and the associated glaciofluvial denudation than by substantial tectonic activity. However, the location and significance of inherited lithospheric sutures, faults, rifts and other structural zones of weakness across the East Antarctic craton cannot be understated as they continued to substantially impact the size, scope and character of associated Wilkes Land sedimentary basins.

2.3 EAST ANTARCTIC ICE SHEET

With pole-ward oceanic circulation patterns and initiation of the ACC by the late Paleogene, cooler ocean waters were able to hold more CO_2 in solution, leading to a substantial decline in atmospheric CO_2 levels [*DeConto and Pollard*, 2003] from an estimated 2000 ppm in the early Eocene to 800 ppm by the late Eocene [*Pearson and Palmer*, 2000]. This dramatic decline from extreme atmospheric greenhouse conditions to more temperate climates was recorded in marine geologic record including stable oxygen isotope data [*Zachos et al.*, 2001] and the first ice-rafted debris [*Ehrmann et al.*, 1991]. Based upon additional evaluation of ice-rafted debris (IRD), subglacial topography, and numerical models, it is highly probable that Antarctic Cenozoic glaciation initiated on the alpine peaks of the Gamburtsev Mountains [*Bo et al.*, 2009].

The DeConto and Pollard [2003, 2009] models, specifically, confirmed the inception of small, dynamic ice caps on these highlands through the Late Tertiary until the eventual amalgamation of these temperate glaciers into one expansive EAIS (Figure 2.5). During the subsequent Pleistocene epoch, glacial-interglacial climate cycles occurred across 41,000 year and 100,000 year cycles with an apparent greater frequency than during the Neogene [*Lisiecki and Raymo*, 2005]. With the majority of the Plio-Pleistocene ice sheet advance characterized as a temperate/polythermal glacial regime, the ASB and WSB and associated subglacial sedimentary basins would have been dominated by glacio-fluvial erosional-depositional processes. Braided to meandering streams would have been common since the early to mid-Miocene, with seasonal flooding prompted by glacial melt. These early ice sheets would have been ablated by melting, rather than iceberg calving [*Anderson*, 1991], with wet-based sliding the dominant erosion mechanism. Young et al's [2011] recent identification of large fjords in the ASB reinforce this dynamic EAIS hypothesis with local temperate/polythermal ice caps emanating from the Vostok and Dome C subglacial highlands to dramatically impact the geomorphology of Wilkes Land.

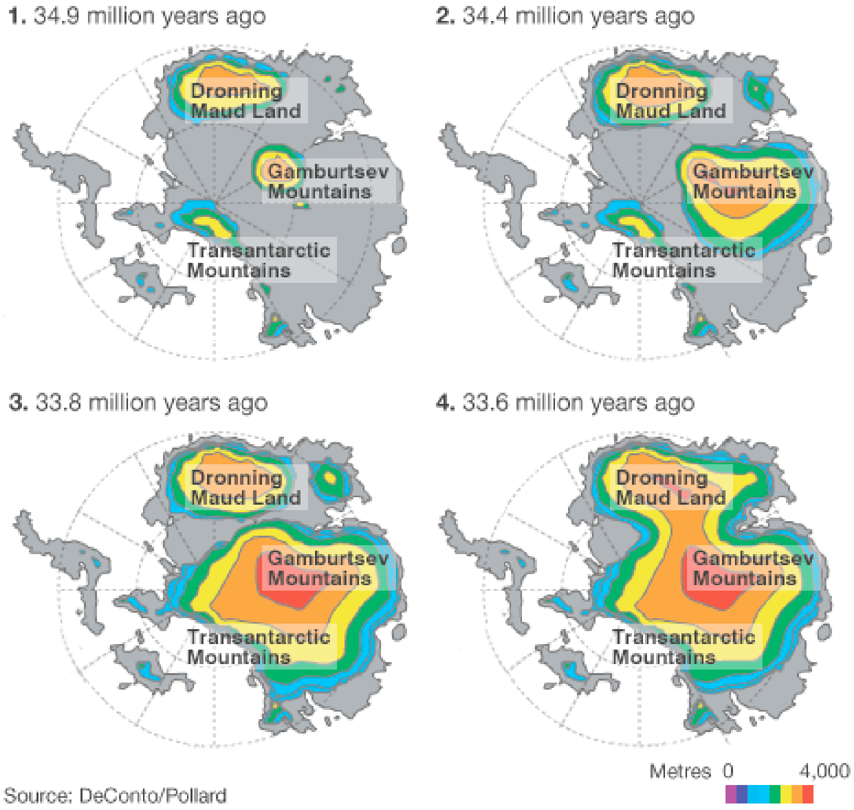

Source: DeConto/Pollard

Figure 2.5: Modelling the initiation of the EAIS: 34.9 Ma to 33.6 Ma [*Amos*, 2006]. Note the alpine to temperate/polythermal glacial conditions impacting Wilkes Land as early as 34 Ma.

Chapter 3: Distribution, Thickness, and Character of Aurora Subglacial Sedimentary Basins, Wilkes Land, East Antarctica

3.1 ABSTRACT

Here I present a detailed subglacial sedimentary basin model for the ASB that defines four distinct subbasins within the catchment with between 3.7 km to potentially as much as 12.5 km of sediment thickness. Each subbasin is proximal to associated subglacial highlands, bolstering the hypothesis of distinct temperate/polythermal alpine glacial regimes as sediment source areas dictating regional denudation. Basin-wide tectonics determined the expanse and depth of these fault-controlled catchments, providing lithologic and structural boundaries to basin evolution, and thereby dictated ice sheet stability. EAIS boundary conditions, including the distribution, thickness, and character of subglacial sedimentary basins, dictate the rate of glacial advance and retreat. These ASB sedimentary basin models support the current hypothesis of early Miocene to Oligocene dual-stage convergent ice flow leading to the geomorphologic development of interior fjords amidst a mountain-block landscape, but may also suggest Pliocene-age EAIS advance-retreat cycles across the Sabrina Subglacial Basin (SSB) resulting in comparatively reduced sediment volumes and basin axis correlating to subglacial channels and hydraulic pathways leading into the present day Totten Glacier catchment. The sedimentary basin models introduced here provide for significantly greater EAIS ice sheet model accuracy by establishing quantifiable limits for subglacial hydrologic and

geothermal flux estimates essential in modeling the polar, deep interior basal ice dynamics that presently dominate the Wilkes Land region.

3.2 INTRODUCTION

Topography, sediment distribution and heat flux are all key boundary conditions governing the dynamics of the EAIS. EAIS stability is most at risk in Wilkes Land across vast expanses of marine-based catchments including the 750,000 sq km expanse of the ASB region (Figure 3.1). Numerical ice sheet models require accurate deformable sediment distribution and lithologic character constraints to estimate overall flow velocities and potential instability. Although subglacial sediment is a key constraint dictating basal ice dynamics *[Alley et al.,* 1987*; Blankenship et al.,* 1986*]* for the EAIS [*DeConto and Pollard,* 2003], sedimentary basin distribution, thickness and lithologic character of the ASB remains a matter of considerable speculation.

Prior ice penetrating radar analyses by Drewry [1976], Siegert et al. [2005], and Wright et al [2012] identified basal reflection data in the ASB consistent with weak erodible sediments, but historical literature estimates for sediment load and character remain scant. As such, potential ASB impact to eustatic fluctuations on a geologic timescale may be underestimated. Subglacial sedimentary deposits directly impact basal topography, thermal flux and effective stress, all key constraints for numerical ice models [*DeConto and Pollard,* 2003]. *Lees* [1910] was the first to recognize that topography alone impacted geothermal flux with intensification in valleys and attenuation along ridges as the isotherms distort at base of a valley [*van der Veen et al.*, 2007]. However, the presence of sizeable subglacial sediment and sedimentary basins can mitigate these isotherm irregularities by providing less topographic relief, increased probability of elevated pore pressures, and a corresponding reduction in effective stress leading to sub-ice till deformation, shear, and corresponding faster ice flow [*Blankenship et al.,* 1986].

Basal melting and shear stress zones beneath large ice flows is a direct function of pressure-dependent sediment viscosity associated with bedrock topography. Basal drag induced by bedrock bumps sticking into the base of the overlying ice can support significantly elevated basal shear stresses, impacting ice and subglacial hydraulic flow patterns [*Alley et al*., 1987]. When ice slides over a bedrock bump, elevated compressive stress generated on the upstream side versus the lee results in a stress differential increasing the probability of subglacial sediment accumulation on the upstream side of the bump and ice cavitation on the lee [*Schoof*, 2007]. This dynamic ice response to physical bedrock surface irregularities provided initial insight into the theoretical formation of subglacial water-filled cavities and potential subglacial till distribution.

Young et al. [2011] presented a detailed morphology of the subglacial landscape of the ASB (Figure 3.1) identifying a vast fjord-incised basal topography carved over a succession of ice sheet configurations dramatically different from the present EAIS. Such modulated ice advance-retreat cycles across the ASB over the millennia have been postulated as the primary mechanism for bed depression over-deepening and the development of interior sloping valley floors that promote additional ice sheet instability and increase susceptibility of rapid outlet glacier retreat to the interior resulting from climatic or oceanic forcing [*Young et al*, 2011]. As an example, Mengel and Levermann [2014] recently replicated runaway ice sheet retreat conditions of some 1000 km into the adjacent WSB interior with the simulated removal of 25,000 GT of ice from the front of the Cook and Mertz/Ninnis grounding lines during the Pliocene. Recent work by Aitken et al [2014] identified potential locations for subglacial sedimentary subbasins across the ASB region, including the Knox, Aurora, Sabrina and Vincennes, but Wilkes Land subglacial basal conditions are often further complicated with the presence of complex dendritic hydraulic drainage networks and associated subglacial lakes. With bed elevations exceeding 1 km below present day sea level, 2-4.5 km of overlying ice sheet, and background regional geothermal heat flux on the order of 50 mW m^{-2}, the ASB region gives rise to the greatest concentration of identified subglacial lakes in Antarctica [*Siegert et al., 2005; Wright and Siegert,* 2011; *Wright et al*., 2012; *Wright and Siegert,* 2012; *Carson et al.,* 2013].

In this study I provide the first quantitative estimates for extent, thickness and potential character of the sedimentary basin deposits lying beneath the EAIS within the ASB complex. The distribution, disposition, and magnitude of any such potential subglacial sedimentary deposits is an important control to establishing accurate basal hydraulic and geothermal flux models which, in turn, facilitate more accurate regional ice and climate models. To evaluate subglacial sedimentary basin boundaries, area, volume, and potential depositional controls, I integrate over 75,000 line kilometers of aerogeophysical data collected as part of NASA's IceBridge program and the UTIG ICECAP program. My purpose is to provide a subglacial sedimentary baseline from which I might begin to more accurately estimate and evaluate ASB subglacial sediment quantity, distribution and character in a geomorphologic context and provide comparison to existing regional cryospheric and morphodynamic hypotheses.

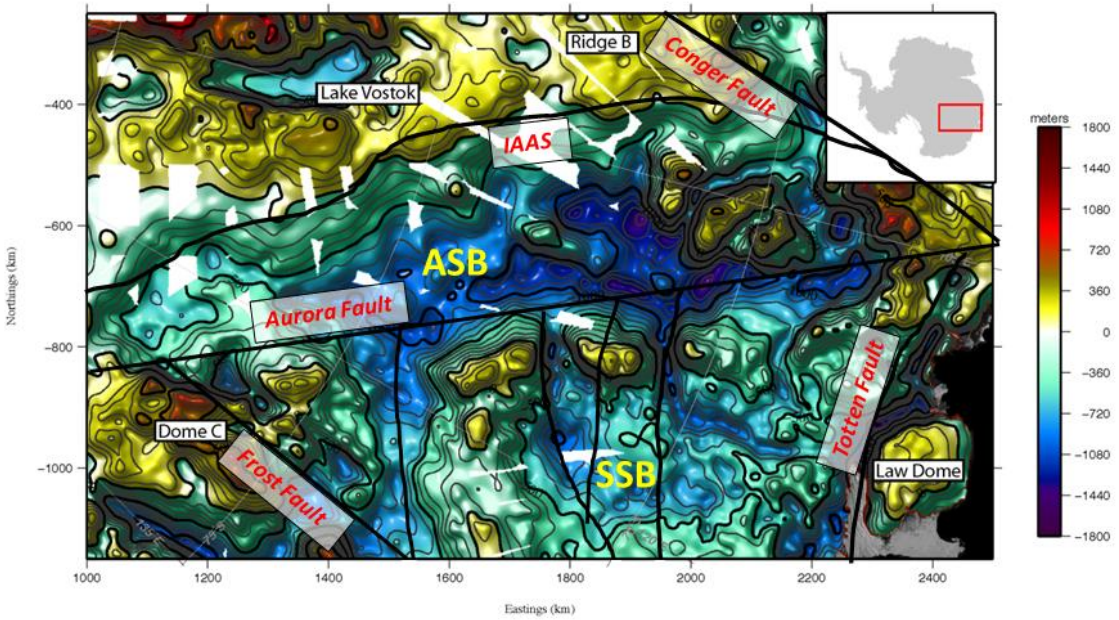

Figure 3.1: Aurora Subglacial Basin unrebounded bed topography [*Young et al.*, 2011] with Regional Faults [*Aitken et al.*, 2014] illustrating basin morphology and mountain block fjords. Aerogeophysical sounding data presented as meters relative to World Geodetic System 1984 (WGS-84) and gridded at 2 km using a natural neighbor approach. IAAS=Indo-Australo-Antarctic Suture.

3.3 DATA RECOVERY AND PREPROCESSING

The ICECAP and IceBridge aerogeophysical data utilized in this ASB study were collected across five austral field seasons between 2008-2013 (Data available through the National Snow and Ice Data Center:

http://nsidc.org/data/icebridge/data_summaries.html). The airborne surveys maintained consistent instrumentation and processing techniques throughout the program, with the exception of the final ICECAP field season where the Bell BGM-3 gravity meter was replaced with a Canadian Microgravity-Gravitational Technologies GT-1A [*Blankenship et al.*, 2014]. The GT-1A, a 3-axis Schuler-tuned system, showed significantly improved resolution, accuracy, and recovery from aircraft dynamics versus the BGM-3.

Gravity data reduction and preprocessing was performed in accordance with methodologies developed and detailed in Holt et al. [2006] and Richter et al. [2001]. Raw gravity data from the BGM-3 was mapped with concurrent GPS data, time stamped, and then corrected for vertical or horizontal aircraft accelerations and pitch, roll, and yaw. An Eötvös correction was then applied to account for the acceleration resulting from the Earth's rotation relative to WGS-84 such that the gravity meter and the source were vertically aligned. The gravity signal was then corrected for aircraft altitude using the theoretical spheroid gravity algorithm developed by Featherstone [1995]. Instrument drift was also accounted for using a portable Lacoste and Romberg gravity meter to tie the aircraft parking site to base station landmarks established at McMurdo and/or Casey Stations, as appropriate. Final edits of the preprocessed gravity results were completed by cross-over error assessment, visual analysis of the plotted data, and root-mean-squared (RMS) analysis. Often the beginning of a line had to be trimmed to reduce the RMS, or in some cases, entire lines had to be removed from the dataset because of excessive in-flight turbulence.

3.4 METHODS

The resultant free-air gravity disturbance for the ASB was leveled to Gravity field and steady-state Ocean Circulation Explorer (GOCE) satellite data (http://www.esa.int/SPECIALS/GOCE/index.html) elevation of 3 km above the ellipsoid to provide consistent spectral content using Generic Mapping Tools (GMT) and the average altitude of each flight line to determine the degree of continuation [*Wessel and Smith*, 1998]. At the 3 km upward continued elevation, the closest bedrock sources yield an expected resolvable geologic wavelength of ~6 km for ideal flight conditions based upon calculations for different basin widths using formulas developed by Childers et al. [1999]. Following leveling and upward continuation, RMS crossover errors were reduced to less than 3 mGals with an estimated spatial resolution of 9 km. Resultant upward-continued free-air gravity data were subsequently gridded at 2 km using a natural neighbor approach, and plotted (Figure 3.2) with GMT.

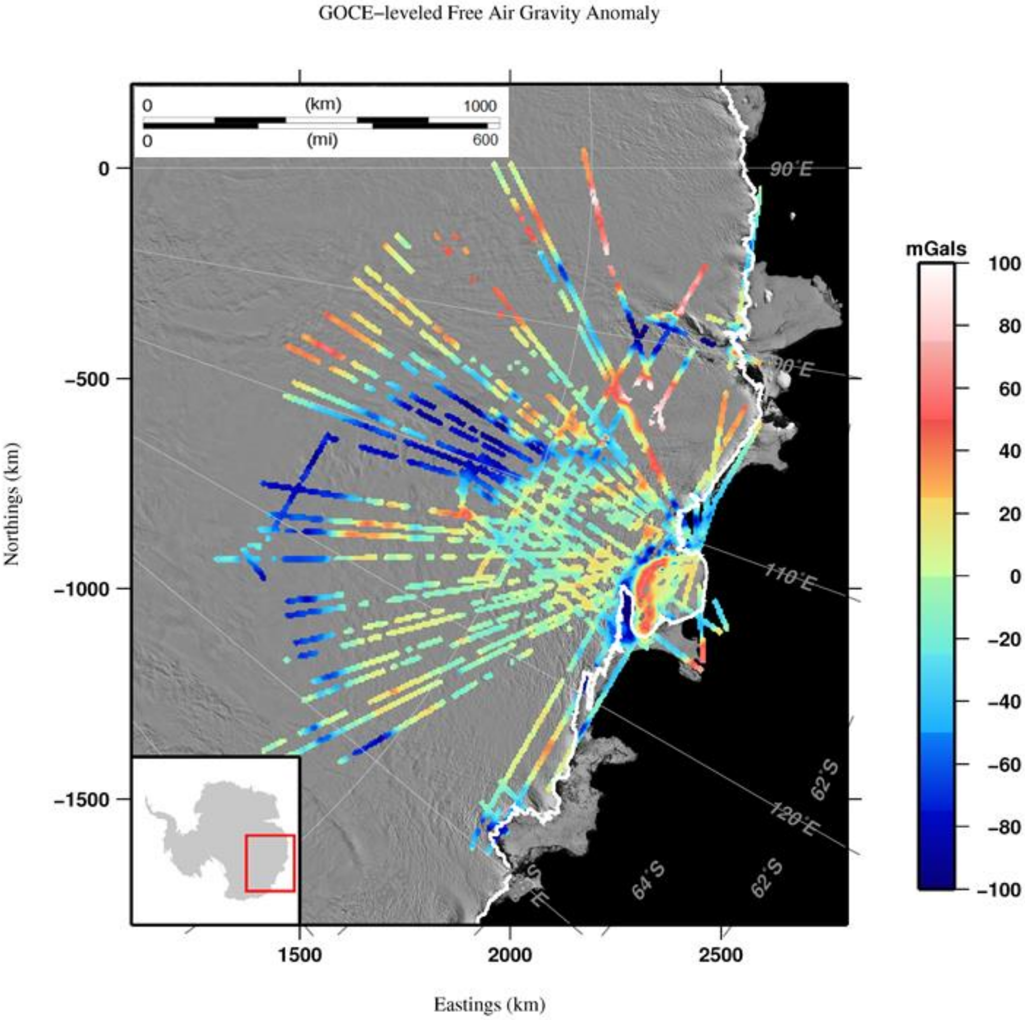

Figure 3.2: Aurora Subglacial Basin Free-Air Gravity (mGals) leveled to GOCE dataset elevation in a Polar Stereographic 71 (PS71) projection illustrating the topographic bias inherent to free air anomalies with the subglacial basins appearing blue-green. Background image is the Moderate Resolution Imaging Spectroradiometer (MODIS) Mosaic of Antarctica [*Scambos et al.*, 2007].

Prior to additional gravity data processing, Bedmap2 models for ice surface and bed topography were improved with the incorporation of ICECAP ice-penetrating radar data collected during ICECAP field seasons 2010-2013. This updated Bedmap2 dataset for the ASB was subsequently incorporated into a 3D structural model for Bouguer and Airy Isostatic gravity data correction as well as 2D and 3D forward and inverse gravity modelling techniques.

Complete terrain-corrected 3D Bouguer gravity anomalies were derived using Paradigm's GOCAD software suite in conjunction with a Geophysics extension developed by MiraGeoscience to enhance deep crust gravitation response. Bouguer gravity results are gridded and displayed in Figure 3.3 using similar resolution and techniques as for free-air gravity results. Ice and bedrock model densities of 0.92 g/cc and 2.67 g/cc, respectively, were established in accordance with prior research in the nearby Lake Vostok region [*Filina et al.*, 2006]. The GOCAD Geophysics algorithms are designed to estimate the gravitational effects of topography using spherical coordinate modeling and a Gaussian-Legendre Quadrature integration methodology with least squares accuracy [*von Frese et al.*, 1981]. By integrating each observation point on the surface with the buried object being modeled of uniform density $\Delta\sigma$, the gravitational effect Δg in spherical coordinates $(ø,\theta,r)$ may be approximated by:

$$\Delta g(ø,\theta,r) = \Delta ø'_l \Sigma_l \{\Delta \theta'_j \Sigma_j (\Delta r_i \Sigma_i [(G/R^2)(\partial R/\partial r)\Delta\sigma] A_i) A_j\} A_l, \qquad (1)$$

where

G is the gravitational constant;

R is the distance between the source and observation points;

r is the radial distance vector between the center mass of the Earth and the observation point coordinates;

(A_i, A_j, A_l) are the Gauss-Legendre quadrature weights [*Stroud and Secrest*, 1966].

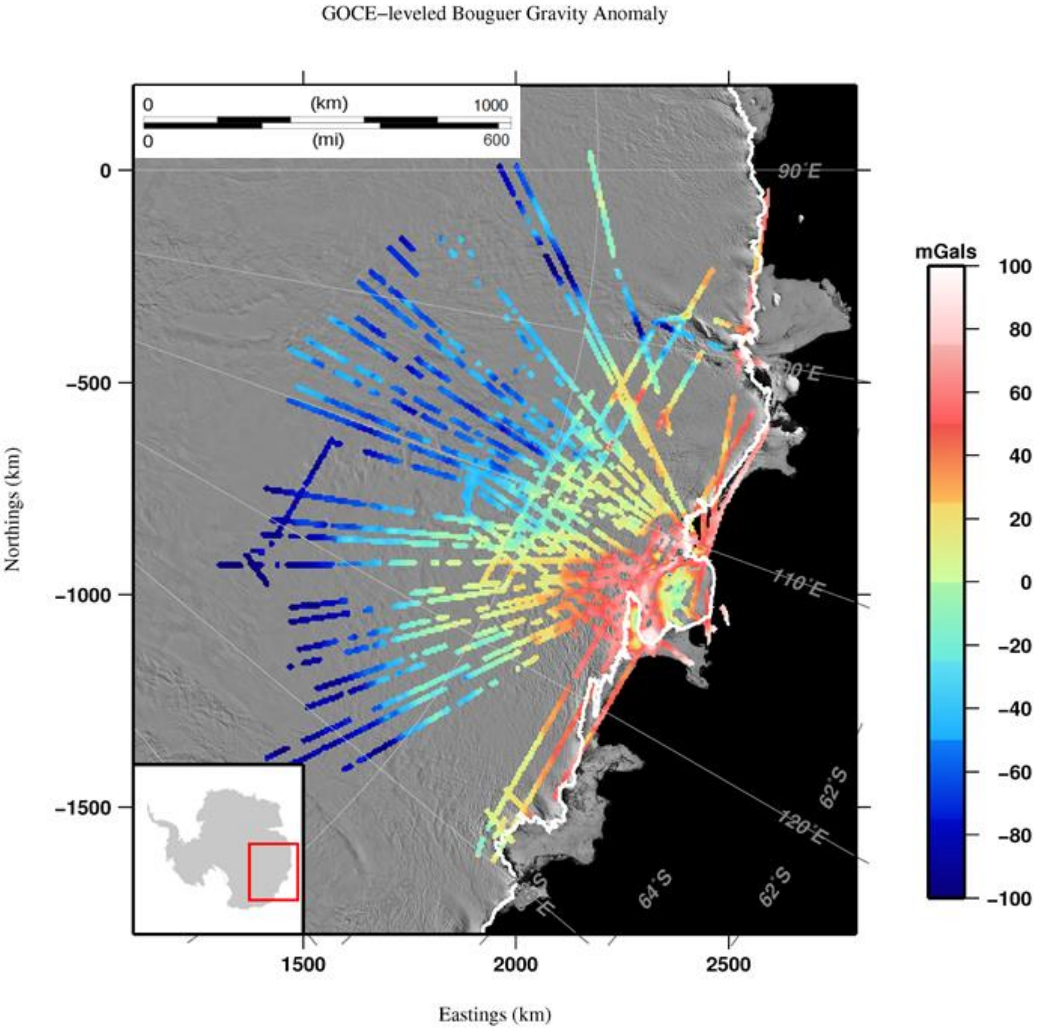

Figure 3.3: Aurora Subglacial Basin Bouguer Gravity (mGals) anomaly leveled to GOCE dataset depicting characteristically thinner lithosphere (red) along the passive margin boundary versus the thicker Proterozoic age East Antarctic craton (blue). Background image is the MODIS Mosaic of Antarctica [*Scambos et al.*, 2007].

Initial Airy isostatic gravity anomalies were calculated by adding the Moho surface to the 3D structural model [*Jachens and Griscom*, 1985] providing a conservative baseline based on a simple, smoothed, Airy correction. Subsequent Airy isostatic corrections implemented an elastic thickness component of 110 km [*Stern and ten Brink*, 1989] to better account for the limited downward Moho deflection of a Proterozoic craton due to ice load (Figure 3.4). Resultant Moho depths of 32-37 km were found consistent with recently published estimates in the Wilkes Land region *[Lloyd et al., 2013; Baranov and Morelli,* 2013]. GOCAD Geophysics software was then employed to calculate the residual gravity anomaly based on the revised 3D structural model using ice, bedrock and mantle densities of 0.92 g/cc, 2.67 g/cc, and 3.3 g/cc, respectively, with ICECAP airborne free-air gravity data input.

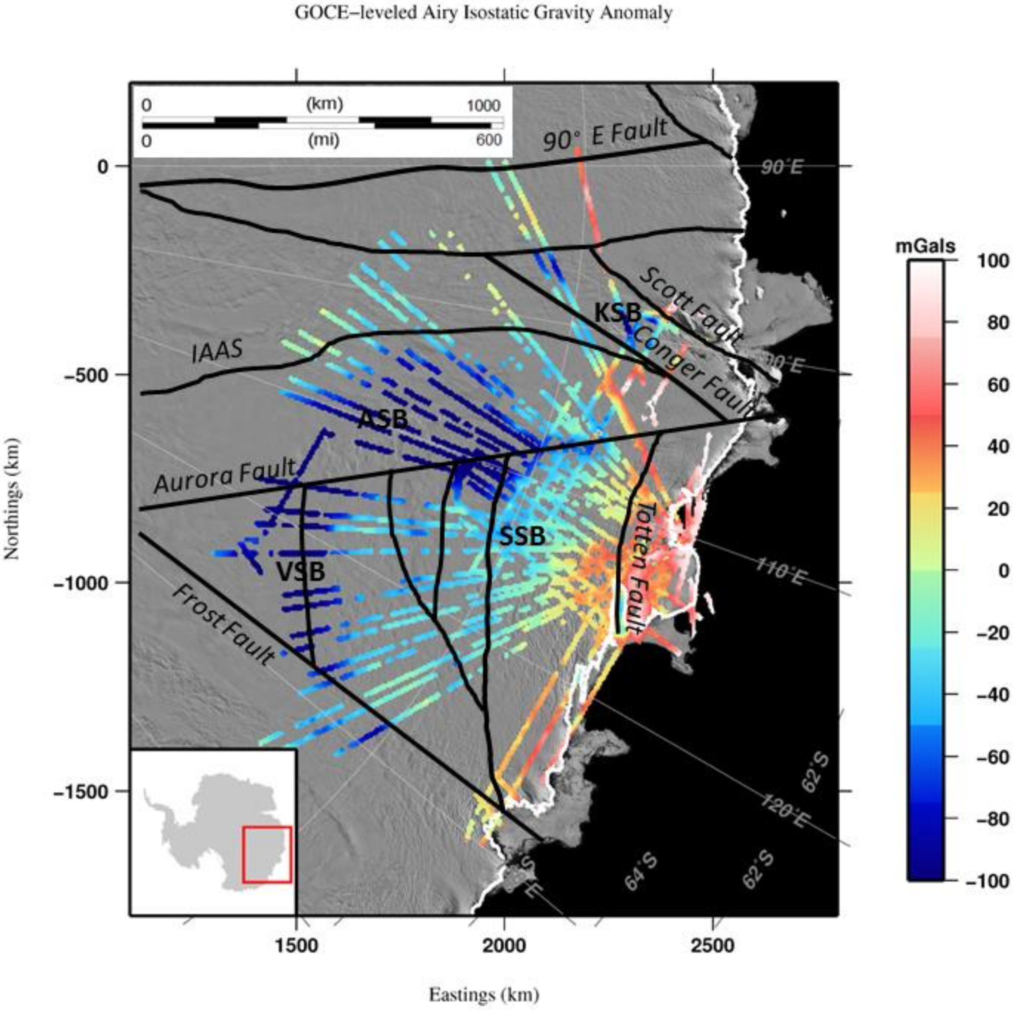

Figure 3.4: Aurora Subglacial Basin Residual Airy Isostatic Corrected Gravity (mGals) anomaly leveled to GOCE dataset with Regional Faults [*Aitken et al*, 2014] indicating gravitational deficiencies relative to the simplified regional lithospheric structure model in the interior subbasins: ASB=Aurora Subglacial Basin, VSB=Vincennes Subglacial Basin, KSB=Knox Subglacial Basin, SSB=Sabrina Subglacial Basin, IAAS=Indo-Australo-Antarctic Suture. Background image is the MODIS Mosaic of Antarctica [*Scambos et al*., 2007].

Spectral analyses of free-air gravity data were completed to provide a direct density estimate of the crust structure based upon prior work in West Antarctica by Damiani et al [2014] with methodologies developed by Fairhead and Okereke [1988], Karner and Watts [1983], and Spector and Grant [1970]. The radial power spectrum of the free-air gravitational response was plotted as the natural log of power versus wavenumber. Least squares line segments were fit to slope breaks to determine representative crustal density boundary depths using the equation $h= -s/4\pi$ (Figure 3.5), where h = depth to source and s = slope of the (natural log) energy spectrum.

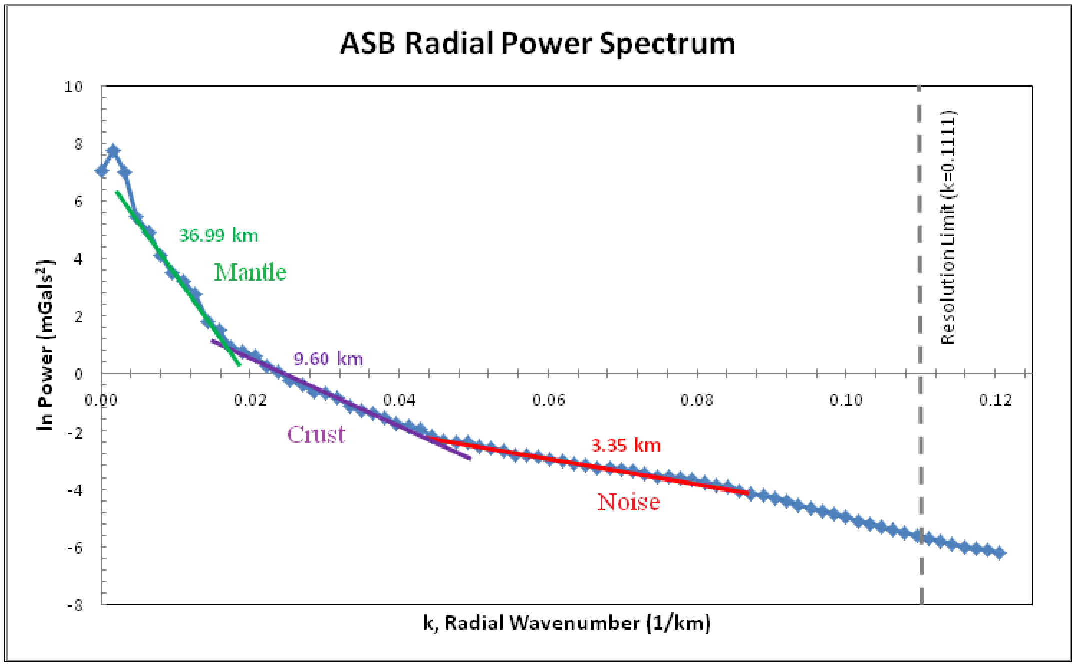

Figure 3.5: Aurora Subglacial Basin Free-Air Gravity Radial Power Spectrum Depth Estimates showing two distinct gravitational source areas – crust (purple) and mantle (green).

With each resultant slope being indicative of the power spectrum characteristic of a specific crustal interface, and the breaks in slope identifying a change in density at a specific wavelength or wavenumber [*Damiani et al.*, 2014; *Spector & Grant*, 1970], depth estimate correlations to wavenumber confirm only 2 lithospheric sources (crust and upper mantle) for the Proterozoic East Antarctic craton.

Aeromagnetic data were also processed using standard methodologies including diurnal, and International Geomagnetic Reference Field (IGRF) corrections followed by subsequent leveling to minimize cross-line differences [*Aitken et al.*, 2014]. Once levelled, magnetic data were gridded and displayed in Figure 3.6 using similar techniques and resolution as for free-air gravity results. Primary Australia-Antarctica conjugate margin faults, including the Darling to Conger and Mundrabilla to Frost Fault systems respectively, were identified commensurate with the Gondwana fit model at 160 Ma presented by Aitken et al. [2014]. Smaller scale regional and conjugate margin faults were interpreted based strictly on total magnetic intensity anomalies to provide some lateral lithologic constraint for subsequent sedimentary basin modeling.

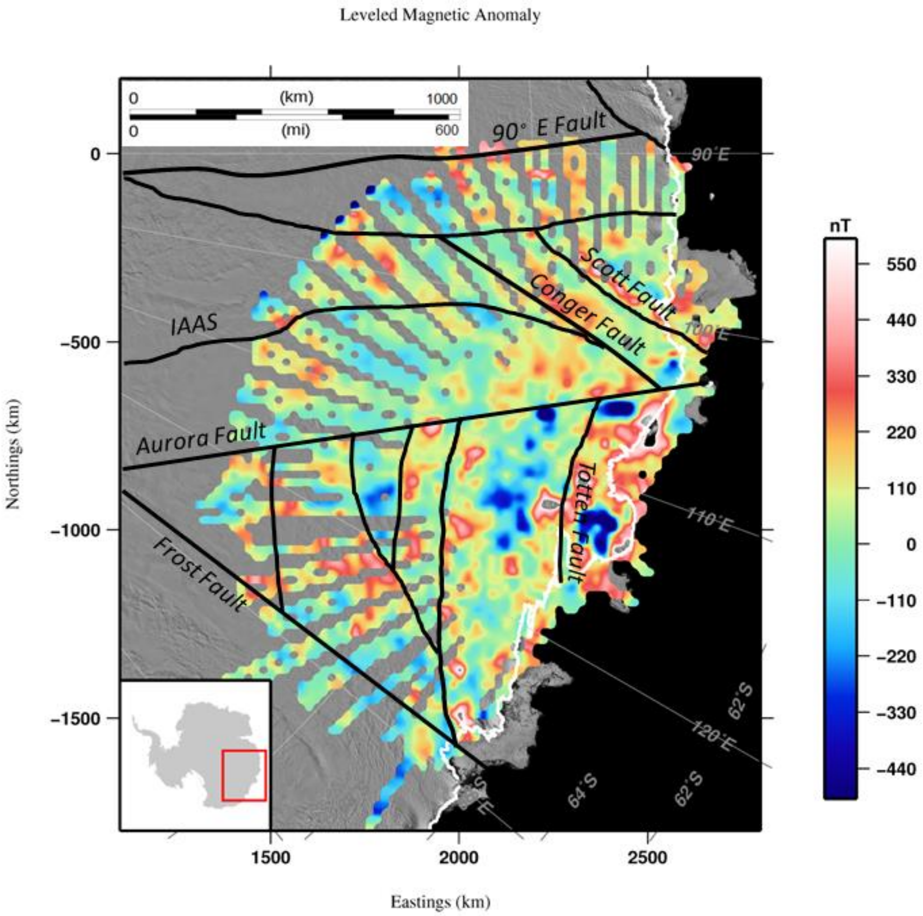

Figure 3.6: Aurora Subglacial Basin Leveled Magnetic Data with Regional Faults [*Aitken et al,* 2014] indicating lateral structural constraints to basin evolution. IAAS=Indo-Australo-Antarctic Suture. Background image is the MODIS Mosaic of Antarctica [*Scambos et al*., 2007].

Magnetic depth to basement (DTB) estimates, utilized as a proxy for sedimentary basin thickness, were subsequently performed via Werner 2D deconvolution methods [*Ku and Sharp*, 1983] and direct gridded at 20 km (Figure 3.7).

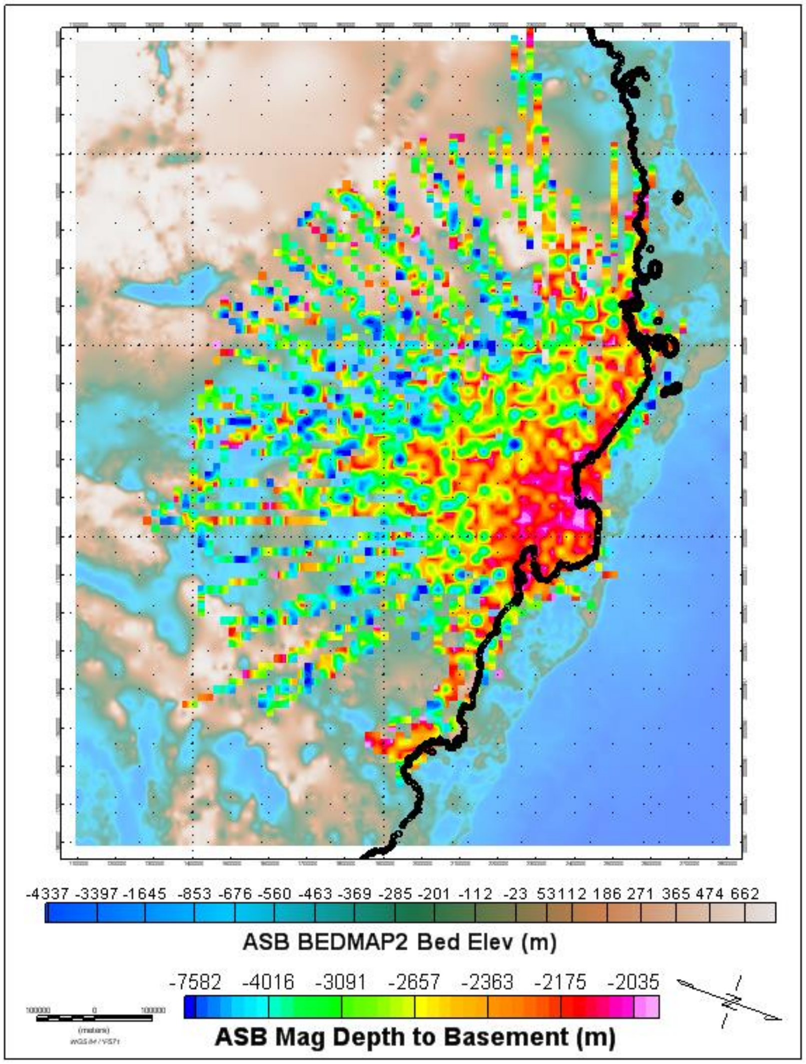

Figure 3.7: Aurora Subglacial Basin 2D Werner Deconvolution Magnetic Depth to Basement Estimates (meters) depicting elevation depths to magnetic basement relative to the WGS84 ellipsoid. Background image is the updated Bedmap2 dataset [*Fretwell et al.*, 2013].

The 2D Werner deconvolution DTB method utilizes a moving window of specific width and distance between each analysis (Table 3.1) such that the depth estimate returned directly corresponds to the window size. As a result, three passes over the magnetic data were performed at three different wavelength/window sizes to capture the full suite of depths characterizing the ASB using methodologies established in Aitken et al [2014].

	Window sizes (km)	**Window Shift (km)**	**Depth – min/max (km)**
Short Wavelength	1,3,5	0.5	0.5, 5
Medium Wavelength	5, 10, 15	2.5	2, 15
Long Wavelength	10, 20, 30	5	5, 30

Table 3.1: Aurora Subglacial Basin Magnetic Depth to Basement Specifications

Topographic roughness was evaluated with 60 MHz coherent ice-penetrating radar data using RMS deviation methods summarized in Shepard et al. [2001] and described in Young et al [2011]. RMS deviation (v) is defined as the RMS difference in height separated by a step (Δx) and given by:

$$v(\Delta x)=\{1/n\Sigma[(z(x_i)-z(x_i+\Delta x)]^2\}^{1/2}, \qquad (2)$$

where

n is the number of sample points;
$z(x_i)$ is the height of the surface at point x_i [*Shepard et al.,* 2001].

Correlation length is the normalized covariance between the flight profile and itself when offset by some lag/distance (Δx) [*Shepard et al.*, 2001; *Turcotte*, 1997]. RMS deviation was characterized at a discrete length of 800 m (Figure 3.8). Smooth regions blanketed by sediment appear blue, while rough topographic highs appear white or red.

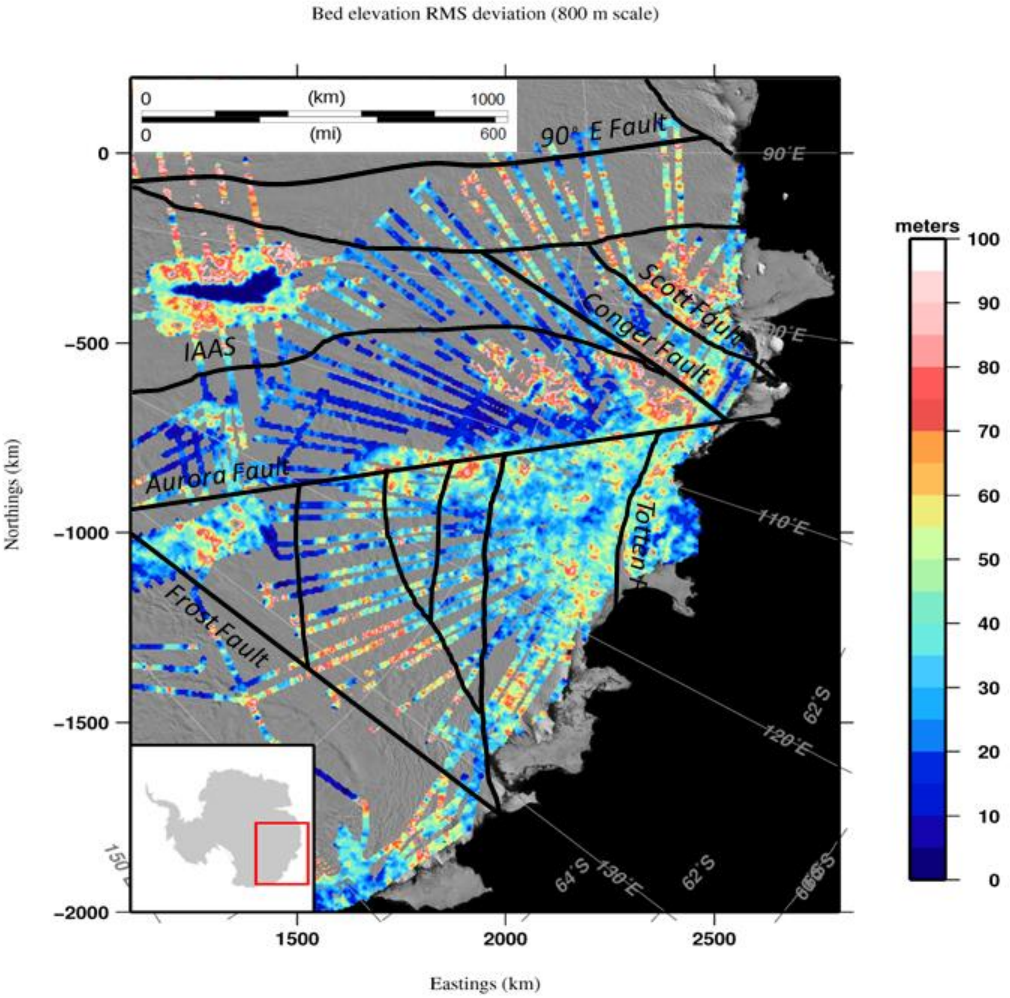

Figure 3.8: Aurora Subglacial Basin Radar Roughness Sediment Mask – 800 m length scale with Regional Faults [*Aitken et al*., 2014] showing smoother subglacial topography in blue and rougher in red/white. IAAS=Indo-Australo-Antarctic Suture. Background image is the MODIS Mosaic of Antarctica [*Scambos et al.* 2007].

ASB sedimentary basin thickness estimates were initially attempted using 3D steepest descent inversion techniques, however, the variable distance between radial flight line patterns resulted in a wavelength bias in the datasets and errant inversion results. Hence, 2D forward modeling of free-air gravity data were performed using Geosoft's GM-SYS® modeling package using a four layer model for ice (0.92 g/cc), sediment (2.35 g/cc), bedrock (2.67 g/cc), and mantle (3.3 g/cc) materials (Figure 3.9).

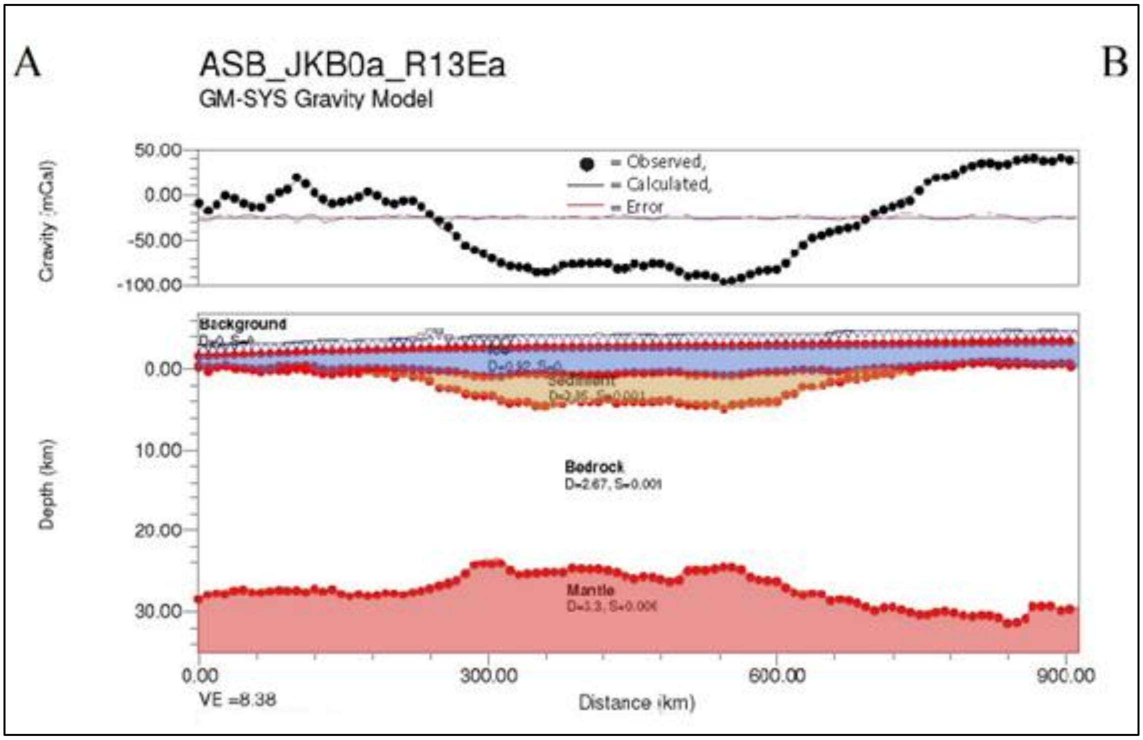

Figure 3.9: Aurora Subglacial Basin 2D GMSYS Forward Gravity Model Profile A-B (see Figure 10 for map A-B profile) – ASB/JKB0a/R13Ea – Red dots represent model horizons with densities posted. Black dots represent observed free-air gravity with modeled gravity depicted as black line.

Stratigraphic model densities were estimated based upon previous seismic and potential fields research in the nearby Lake Vostok [*Roy et al.*, 2005; *Filina et al.*, 2006] and WSB regions *[Ferraccioli, Coren, and Bozzo,* 2001], and compared to theoretical estimates [*Bahr et al.*, 2001]. A significant variation in modeled sediment densities was discovered in published literature for Wilkes Land, prompting an evaluation of sediment densities from 1.85 g/cc to 2.4 g/cc to assess 2D forward model basin response relative to supplemental data constraints including magnetic DTB. Initial forward gravity models were constructed using the more conservative densities of the Lake Vostok literature (1.85 g/cc) which resulted in four subglacial sedimentary subbasins, ASB, VSB, KSB, and SSB with maximum thicknesses ranging from 3.5 to 8.5 km. Subsequent empirical examination of probable sediment densities at these burial depths with an average of 2 km of overlying ice, equivalent to overburden pressures on the order of 70-90 MPa, resulted in subglacial sediment densities of 2.2-2.5 g/cc and estimated sediment porosities of 15-18% [*Bahr et al.,* 2001; *Gueguen and Palciauskas*, 1994; *Zoback*, 2010]. Based on these results and prior modeled subglacial sediment densities in the WSB [*Ferraccioli et al.*, 2001], final forward gravity models were constructed using a subglacial sediment density estimate of 2.35 g/cc.

Moho surfaces used in the 2D models were derived from simple Airy isostatic calculations with zero flexure and manually smoothed. Sedimentary basin depths were adjusted until modeled gravity results reflected observed. Because 2D forward gravity modeling is non-unique, the initial layered density models were kept as simple as possible. Resulting sediment isopachs for each 2D flight line were compiled and subsequently interpolated using a minimum curvature technique with 2 km grid spacing

(Figure 3.10). This revised density model for the 2D forward gravity calculations resulted in maximum subbasin thicknesses ranging from 3.7 to 12.5 km.

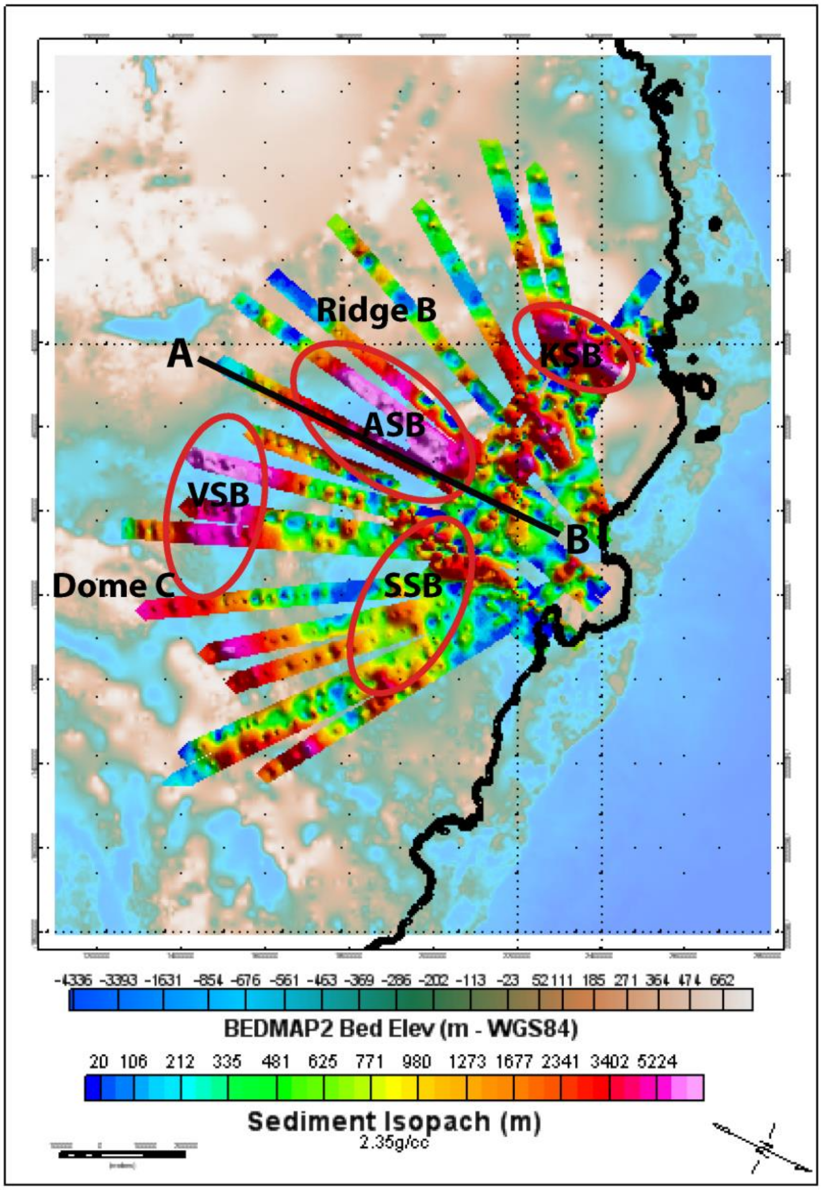

Figure 3.10: Aurora Subglacial Basin sediment isopach (meters) indicating four distinct sedimentary subbasins, all with thicknesses exceeding 3.7 km: ASB = Aurora Subglacial Basin, VSB = Vincennes Subglacial Basin, KSB = Knox Subglacial Basin, SSB = Sabrina Subglacial Basin. A-B profile identifying flight line ASB/JKB0a/R13Ea also shown.

Sediment volume calculations were subsequently performed based upon the 3D raster isopach using the following expression:

$$\mathrm{Vol}_{sed} = \Sigma_{ij}\, P_A(T_{ij}) \qquad (3)$$

where

P_A = pixel area (m^2);

T_{ij} = average pixel isopach thickness (m).

To estimate uncertainties, I derived from the use of different available interpolation methods to produce the isopach raster surfaces, I examined several methods in Geosoft's Oasis montaj® software suite. Minimum curvature minimization methods combined with linear spline interpolation produced the most accurate volume estimates given the predominantly radial orientation of the ASB aerogeophysical dataset.

3.5 OBSERVATIONS AND INTERPRETATION

ICECAP airborne free-air gravity results (Figure 3.2) reflected topography across the ASB as would be expected. Free-air gravity lows corresponding to topographic lows in the basin and free-air gravity highs corresponding to topographic highs. Airborne free-air gravity was leveled to GOCE downward-continued data altitudes of 3 km above the ellipsoid with satisfactory results.

ICECAP airborne Bouguer gravity calculations (Figure 3.3) reflect both increasing ice load toward craton interior as well as the thinner continental crust at continental margins and thicker crust toward craton interior. ASB Bouguer gravity data presented herein utilizes the most updated ice surface and bed topography 3D models incorporating Bedmap2 datasets and ICECAP airborne radar and laser altimetry data from field seasons 2010-2013. These new ASB Bouguer gravity results were calculated using a Parker-Oldenberg approach [*Oldenburg,* 1974; *Parker,* 1973] to produce a 3D forward model based on updated ice and bed topographies that was then subtracted from the ICECAP airborne free-air data. The resultant Bouguer gravity anomalies do not reflect data over floating ice, as water depths were not adequately constrained and potential Bouguer data along the continental margin was not required in construction of an interior ASB sedimentary basin model.

Residual isostatic anomaly gravity data were calculated (Figure 3.4) to attempt to remove the gravitational bias introduced as a result of the downward deflection of the crust due to the EAIS. Because expansive ice loads often result in a direct isostatic response [*Watts*, 2001], a simple Airy isostatic correction was applied to account for ice and crustal thickness, the resultant gravity deficiency in ASB interior is reflective of mass missing from the model. *Diehl* [2008] identified seismically-defined basin sediment infill [*Anandakrishnan and Winberry*, 2004; *Peters et al.*, 2006] to be correlated with isostatic residual gravity response for sedimentary basins in West Antarctica such that: 0+/-50 m = -8 mGals, 300+/-50 m = -10 mGals and >1000 m = -15 mGals; this model was subsequently modified such that < -10 mGals indicated a moderate likelihood of sedimentary basins and < -30 mGals indicated a high likelihood of sedimentary basins. If the Damiani et al. [2014] model is applied to the ASB Airy isostatic correction results, all portions of the ASB, VSB, and KSB have a high likelihood of sedimentary basins with the SSB having a moderate likelihood. Given the lack of recent volcanism and characteristically low mantle-derived geothermal flux for the East Antarctic craton in the Wilkes Land region [*Llubes et al.*, 2006], the negative isostatic anomalies over the relatively cool lithosphere could most likely be attributed to low-density bodies of a range of compositions [*Diehl*, 2008]. Such negative residual isostatic gravity anomalies would later be used to laterally constrain sedimentary basin isopachs derived from 2D forward models.

Spectral analyses of the free-air gravity anomalies in the ASB (Figure 3.5) showed just one change in slope indicative of density contrasts at the Crust-Moho boundary *[Damiani et al,* 2014*; Spector & Grant,* 1970] with crustal depths estimated at 9.6 km and Moho depths estimated at 37 km. These estimates are in agreement with recent East Antarctic lithospheric structure models published by Lloyd et al [2013] and Baranov and Morelli [2013]. Based on the power spectrum energy plots and interpreted least squared line segment slopes, the best fit Moho depths for the ASB consistently fell between 32-37 km with no apparent mid-crust discontinuity as would be expected from an old cratonic EAIS lithosphere of Proterozoic age. Regional body wave tomography analyses confirm these spectral analysis results with Moho depths on the order of 25-35 km for the ASB [*Baranov and Morelli*, 2013; *Lloyd et al.*, 2013] and no mid-crustal density contrast. And although Bannister et al. [2003] found mid-crustal discontinuities in the Transantarctic Mountains at approximately 8-14 km depth using nonlinear inversion of receiver functions, they noted that the associated seismic velocity boundary did not extend west into the East Antarctic craton. Lateral spatial changes in crustal boundaries based on spectral analysis were not performed here as a result of the variable spatial wavelengths inherent in the data resulting from the radial flight pattern.

Leveled aeromagnetic data were utilized to define regional faults across the ASB (Figure 3.6) to gain a better understanding of potential lithologies and associated lithologic densities that might laterally constrain sedimentary basins and facies. Regional faults were identified with guidance from recent conjugate Australia-Antarctica margin work by Aitken et al. [2014] who identified tectonic features impacting basal boundary conditions and the evolution of the EAIS. Most notable across the region are the two extensive trans-continental faults, the Frost Fault and the Conger Fault, that trend north-south and bound the eastern and western portions of the ASB. The Frost Fault separates the rocks of the eastern and western Mawson craton, while the Conger Fault represents a footwall that bounds the Knox Subglacial Basin [*Aitken et al.*, 2014]. By overlaying the magnetic fault interpretations on an ASB bed topography map, the Conger regional fault trends NW-SE parallel the axis of the ASB (Figure 3.1).

Associated extensional faults running orthogonal to the Conger Fault correspond to a number of subglacial fjords and topographic lows first identified by Young et al. [2011]. In addition, the Frost Fault location in particular may suggest that it was associated with the establishment of eastern boundary of the ASB, and the Indo-Australo-Antarctic Suture (IAAS) with the western ASB constraint (Figure 3.8). The Aurora Fault established a zone of structural weakness that was subject to extension during the late Cretaceous with the separation of Australia from Wilkes Land and then subsequently preferentially eroded into its present form. The Totten Fault constrains the Totten Glacier catchment and trunk with the distinct separation of the Albany-Fraser Province (Law Dome) remnant left abutted against the East Antarctic craton. Although lithologic identification of subglacial bedrock materials across the ASB remains loosely constrained with only glaciomarine sedimentation on the continental shelf, such structural controls provide good indication of geomorphologic evolution and lateral constraint for sedimentary basin extent.

2D Werner deconvolution DTB results for the ASB indicate elevation depths to magnetic basement relative to a WGS84 ellipsoid approximation of mean sea level. DTB results ranged from > -2 km to over > -14 km across all the 20 km direct-gridded locations (Figure 3.7). While errors are difficult to quantify, they are typically estimated to be about 20-40% of the source depth [*Kilty*, 1983]; therefore, increases in ice sheet thickness should result in greater standard deviations. Median medium wavelength DTB values for the ASB were -4.2 km with a mean value of -4.7 km and a substantial standard deviation (+/- 2.2 km). Extremely shallow DTB estimates occurring above the base of the ice sheet were rejected prior to gridding in well-sampled areas. DTB results less than -500 m are found to be within the error of the base of the ice sheet and should therefore be interpreted as ice directly overlying crystalline basement rocks [*Aitken et al.*, 2014]. Despite the high variability and source depth errors, DTB results provided a valid vertical constraint for subsequent 2D forward gravity modeling of sedimentary basin thicknesses.

Subglacial bed surface roughness was quantified by evaluating RMS deviation over correlation length scales of 800 m (Figure 3.8) revealing significantly smoother surfaces across the interior Aurora, Vincennes and Knox subglacial basins with RMS height deviations falling below 10 m over the respective length scales. RMS deviation over correlation length was not only impacted by changes in RMS deviation, but also by larger correlation lengths associated with smoother and rougher surfaces by smaller lengths [*Shepard et al.*, 2001]. As such, subglacial highlands (including Dome C, Ridge B, and the Vostok highlands) resulted in RMS height deviation values exceeding 70 meters at the 800 meter correlation length scale. The distinct transition between rough and smooth bed surfaces at the subglacial basin edge in the interior ASB provided additional lateral constraint during subsequent 2D forward gravity modeling efforts.

These smooth bed features are consistent with the presence of weak, unconsolidated sediments within these basins [*Alley et al.,* 1987].

Subsequent 2D forward gravity modeling (Figure 3.10) revealed that much of the interior ASB, characterized by smooth bed surfaces in radar sediment mask analyses, exhibited overlying subglacial sediment thickness exceeding 500 meters. Four distinct subbasins, the ASB, VSB, SSB, and KSB, that were characterized by RMS deviation versus correlation length estimates of less than 10 meters at the 800 meter scale contained sedimentary basin isopach results in excess of 3.7 km. The VSB contained a maximum sediment isopach value of 8,303 meters while the ASB, SSB, and KSB revealed maximum sediment thicknesses of 10,563, 4,915 and 12,515 meters, respectively. These thicknesses would correspond to estimated sediment volumes with 20% porosity for the VSB of 398,082 +/- 164,454 km^3, the ASB of 283,810 +/- 117,246 km^3, the SSB of 26,349 +/- 10,885 km^3, and the KSB of 123,451 +/- 50,999 km^3.

The VSB subbasin, is immediately adjacent to the Dome C subglacial topographic high, while the ASB and KSB subbasins were mapped in direct association with the Ridge B subglacial highlands. With potential source areas so close to the depocenters, I estimate the time required to infill the VSB, ASB, and KSB basins with the respective volume of sediment (Table 3.2) to gain an improved understanding of sediment provenance, composition, and the relative quantity of preglacial versus postglacial basin infill. Assumptions were made that 1) if the basins were overlain by the EAIS, erosion processes, not depositional would dominate [*Siegert et al.*, 2004], and 2) with EAIS advance to basin margins, temperate/polythermal systems would dominate, not present-day polar.

Process	Sedimentation Rate	VSB	ASB	KSB
Fluvial	0.075 cm/yr	4.7 M yrs	5.6 M yrs	11.3 M yrs
Temperate/polythermal Glaciation	10 cm/yr	35 k yrs	42 k yrs	85 k yrs

Table 3.2: Estimated Basin Deposition Elapsed Time (assuming all sediment deposited prior to current polar EAIS), fluvial rates based on historic Gulf of Mexico rates [*Galloway and Williams*, 1991], temperate/polythermal rates are based on current temperate/polythermal valley glaciers of SE Alaska [*Hallet et al*, 1996].

3.6 DISCUSSION

Based on these results, it is evident that the temperate/polythermal systems are orders of magnitude more efficient at basin infill, such that the vast majority of subglacial sediment in the VSB, ASB, and KSB are the result of these temperate/polythermal depositional processes. These high sediment fluxes were possible in the post-middle Eocene, during a period of temperate/polythermal glaciation from 34-9 Mya, continental shelf sequences immediately offshore west Wilkes Land and the Totten Glacier catchment [*Close, Stagg, and O'Brien,* 2007]. During the onset of temperate/polythermal processes in the early Miocene, the sedimentation rate estimated from Ocean Drilling Program (ODP) cores in Prydz Bay was as much as seven times higher than the more conservative Hallet et al. [1996] rate used in Table 3.2 here [*Cooper and O'Brien*, 2004].

The KSB sedimentary basin lies directly within the Denman Glacier catchment, and the ASB sedimentary basin in the catchment for Totten Glacier. The VSB lies adjacent to the Dome C ice divide and a multitude of subglacial lakes [*Siegert et al*. 2005; *Tabacco et al.*, 2006]. Wright et al. [2012] mapped the subglacial hydraulic potential associated with these subglacial lakes for the ASB region and found that the majority of the subglacial hydraulic flow paths lead from the VSB and ASB subbasin interior, across the SSB, and into either the Reynolds Trough and/or Totten Glacier catchments, respectively.

Here I have presented the first comprehensive subglacial sediment isopachs for the ASB region derived from airborne gravity measurements and corroborated against other geophysical datasets that are known sedimentary basin indicators. The increase in maximum sedimentary basin thickness, ranging from 8.3 km thick in the eastern VSB to 12.5 km thick in the western KSB, supports a hypothesis of basin geometry dictating ice sheet stability across time as the Denman-Scott catchment and the KSB show more restricted subglacial topography versus the broader subglacial topography with less relief to the east in the Totten-MUIS catchment and associated ASB, VSB and SSB subbasins. The presence of thick sediment accumulations in the VSB, ASB, and KSB subbasins, directly associated with subglacial Ridge B and Dome C highlands, support hypotheses of distinct alpine glacial regimes [*Filina et al.*, 2008; *Young et al.*, 2011] in the early Miocene/late Oligocene supplying the bulk of the sediment into these basins. This contention is further substantiated by the fact that polar ice currently characterizing the Wilkes Land region is predominantly considered an erosional as opposed to depositional environment, such that the sediment detected within the ASB interior would have been deposited when the basins were free of ice in a more marine setting *[Siegert et al.*, 2004].

However, what explains the smaller SSB sedimentary deposits and their concentration in the troughs of the upper reaches of the Totten Glacier catchment? More recent subglacial hydraulic modeling in the ASB by Wright et al. [2012], combined with recent climatic ice volume models by Cook et al. [2013] and Mengel and Levermann [2014] in the nearby WSB raise the possibility of a more dynamic EAIS actively mobilizing sediment from the SSB to depocenters further out on the continental shelf and margin during shorter Pliocene timescales. Evidence of subglacial sediment distribution and associated hydraulic networks leading to hydraulic pressure equilibrium with the overlying ice sheet in catchment interiors was recently illustrated by Schroeder et al. [2013] for Thwaites Glacier catchment, West Antarctica, raising the possibility of potential instability in the SSB over shorter time scales versus the VSB, ASB, and KSB whose more constrained topography could have insulated the interior ASB region from eustatic forcing mechanisms across such shorter time scales. If these hypotheses hold true for the ASB region, the geomorphologic development of areas in the lower Totten Glacier/Reynolds Trough catchment, including portions of the SSB, might best be explained by Pliocene epoch Milankovitch climate cyclicity [*Jamieson et al.*, 2008]. Such erosive glacial advance/retreat cycles over the SSB may explain the comparatively reduced sediment volumes and basin axis correlation to subglacial hydraulic pathways and channels leading toward the present day ice margin and Totten Glacier catchment [*Jamieson et al.*, 2010]. With the SSB characterized by WGS-84 bed elevations in excess of 500 meters below sea level, and significant subglacial hydraulic pathways, the likelihood of a significant sediment deformation component fueling basal EAIS dynamics in the region [*Alley and Blankenship*, 1987] can be substantiated.

3.7 CONCLUSIONS

Although subglacial sediment is a key constraint dictating basal ice dynamics [*Alley et al.*, 1987; *Blankenship et al.,* 1986] for the EAIS [*DeConto and Pollard*, 2003], the size, scope, and significance of subglacial sedimentary basin distribution in the ASB has remained a topic of significant debate in scientific literature. However, my findings reveal the first evidence of significant sedimentary basin development across the ASB region and relative volumes for four distinctly different subglacial subbasin depocenters – the ASB, VSB, KSB, and SSB. I observe substantial differences in sediment volume and morphology between the subbasins, supporting the hypotheses of different structural highlands as sedimentary source areas for each depocenter and sedimentary subbasin development impacted by distinctly different fluvial and temperate/polythermal glacial ice sheet configurations.

The overall distribution and character of the ASB sedimentary subbasins across western Wilkes Land supports the Young et al [2011] hypothesis of past temperate/polythermal glaciations with different ice sheet configurations selectively deepening preexisting river valleys at different points across geologic time. Such glacial advance-retreat cycles emanating from either one or both adjacent highlands (Ridge B and/or Dome C), would have dramatically disparate impacts across the ASB region, both in terms of a) selective overdeepening of ASB, VSB, SSB, or KSB tributaries and b) associated subbasin sediment influx (sedimentation rates). The current polar EAIS configuration is unlikely to have generated such significant, yet distinct sedimentary subbasins across the ASB region, due to relatively slow ice flow (compared to temperate/polythermal conditions) across trough axes and the predominantly erosional versus depositional character of polar ice sheets [*Young et al,* 2011; *Siegert et al,* 2004].

First order aerogeophysical mapping provides estimates as to the size, shape and volume of the ASB sedimentary subbasins (Figure 3.10) - VSB of 398,082 +/- 164,454

km^3, the ASB of 283,810 +/- 117,246 km^3, the SSB of 26,349 +/- 10,885 km^3, and the KSB of 123,451 +/- 50,999 km^3. In addition to the broad implications for EAIS boundary conditions determining rate of retreat used in Wilkes Land climate models, the extent, thickness and character of the ASB subglacial strata may also contain some of the best preserved paleoclimatic data associated with the last EAIS retreat-advance over this region and thus be a future target for subglacial access drilling once the technology matures.

Chapter 4: Sedimentary Basin Models for the Wilkes Subglacial Basin, East Antarctica

4.1 ABSTRACT

Topography, sediment distribution and heat flux are all key boundary conditions governing the dynamics of the East Antarctic ice sheet (EAIS). EAIS stability is most at risk in Wilkes Land across vast expanses of marine-based catchments including the 1400 km x 600 km expanse of the Wilkes Subglacial Basin (WSB) region. Numerical ice sheet models require accurate deformable sediment distribution and lithologic character constraints to estimate overall flow velocities and potential instability. Here I present the first detailed subglacial sedimentary basin model for the WSB that defines distinct northern and southern sub-basins within the catchment containing a central Southern WSB basin with an average sediment isopach value of 1,623 m +/- 254 m and sediment thicknesses in excess of 6 km in certain locations, and the Northern WSB revealed average sediment isopach values of 1,144 m +/- 179 m and subglacial sediment thicknesses in excess of 2.5 km several sub-basin locations. Basin-wide tectonics determined the expanse and depth of these fault-controlled catchments, providing lithologic and structural boundaries to basin evolution, and thereby dictated ice sheet stability. The Southern sub-basin is bordered by the TAM and the East Antarctic Rift system (EARS) subglacial highlands, bolstering the hypothesis that a combination of temperate/polythermal alpine regimes during the early Miocene/late Oligocene dictated regional denudation in the Southern WSB. The Northern WSB geomorphology is dominated by substantially thinner subglacial sedimentary deposits with significant accumulations only in restricted, fault-controlled, channelized basins leading to

predominant outlet glacier catchments. Our WSB sedimentary basin model supports a more dynamic EAIS across the Northern WSB during the Pliocene with potential for basin-scale subglacial hydraulic networks governing basal drag and submarine, landward-sloping bed elevations enhancing inherent instability. Hence, sedimentary basin model improvements introduced here provide for significantly greater EAIS ice sheet model constraint accuracy in establishing quantifiable limits for subglacial hydrologic and geothermal flux estimates essential to modeling the polar, deep interior basal ice dynamics that presently dominate the Wilkes Land region.

4.2 INTRODUCTION

Heterogenetic distribution and character of subglacial sedimentary basin deposits have long been identified as a key constraint dictating basal ice dynamics [*Alley et al.,* 1987, *Blankenship et al.,* 1986]. Here I introduce the first sedimentary basin isopachs for the entire WSB, a 840,000 square kilometer expanse with an average bedrock elevation of 500 m below sea level [*Drewry*, 1983] immediately west of the 3500 km long, 4500 m high TAM range. With potential WSB eustatic sea level rise estimates ranging from 3 – 7 m [*Mengel and Levermann*, 2014; *Pollard et al.*, 2015]**,** basal constraints presented herein quantify sedimentary basin distribution, thickness and lithologic character and provide critical insight into the geomorphologic history of the basin while standing to improve the accuracy of future ice dynamic models for the region (Figure 4.1).

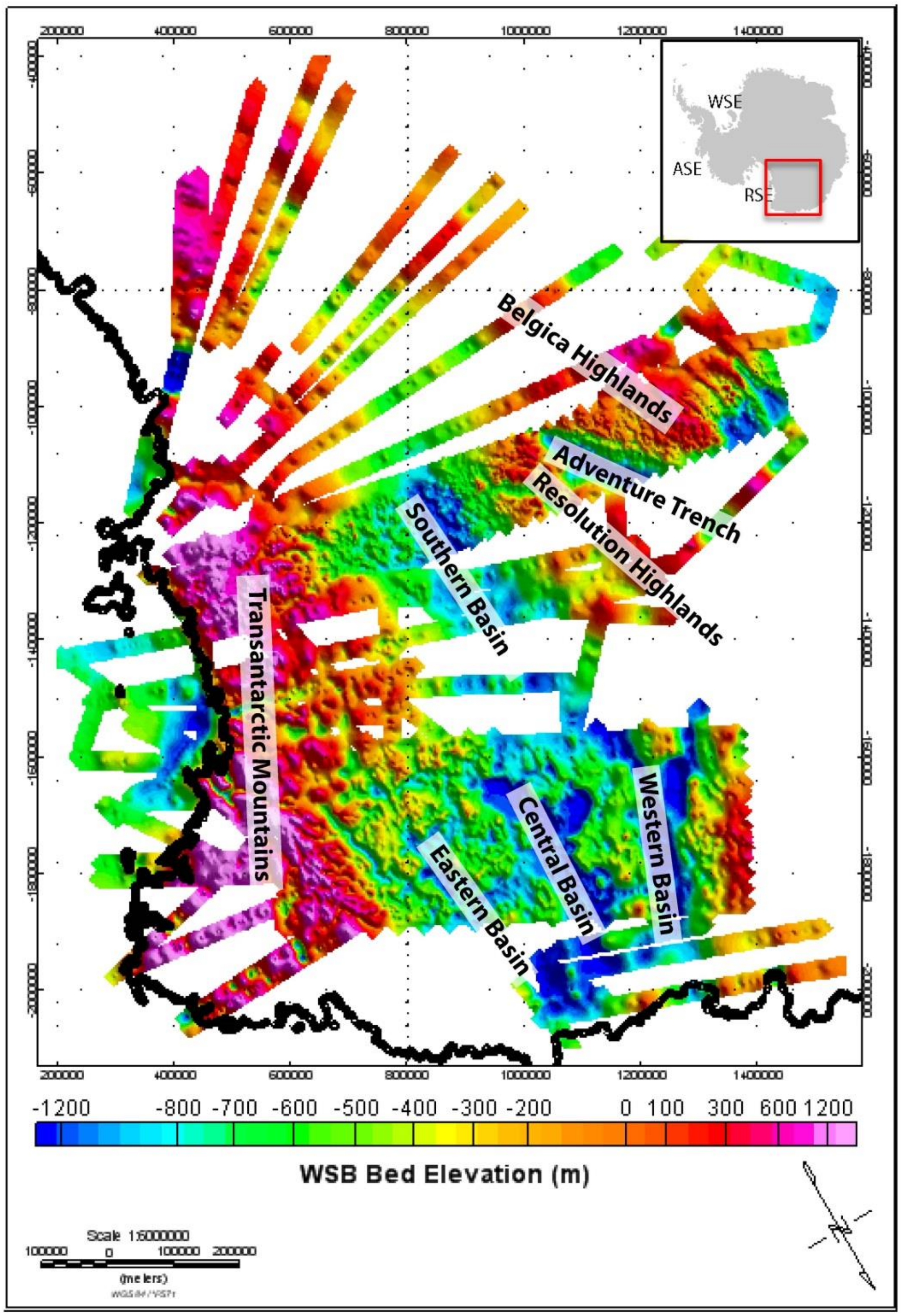

Figure 4.1: Wilkes Subglacial Basin bed topography. Aerogeophysical sounding data presented as meters relative to WGS-84 and gridded at 2 km using a minimum curvature approach.

While the existence of a sediment-draped WSB was first postulated as early as the 1970s from airborne ice-penetrating radar data [*Drewry*, 1976], the tectonic evolution of the basin remains controversial. Mutually incompatible structural models have been suggested including a flexural downwarp of lithosphere [*Stern & ten Brink,* 1989], a rift basin scenario [*Steed*, 1983], and most recently, a region of extended terrain with amagmatic, Cenozoic denudation [*Ferraccioli et al.*, 2009; *Jordan et al.*, 2013]. Regardless of the tectonic forcing mechanism, fluvial denudation and scouring processes would have dominated geomorphologic evolution through the Eocene and into the early Oligocene following the proximal TAM uplift [*Lawrence et al.*, 2007]. By the post mid-Oligocene WSB sedimentary basin geomorphologic evolution would be dominated by temperate/polythermal and subsequently polar glacial cyclicity and denudation by the late Miocene [*Sugden et al.*, 1995]. Despite historical viewpoints that the EAIS was relatively stable [*Mercer*, 1978], more recent Wilkes Land studies suggest that the EAIS (particularly where grounded below current sea level) may have been far more dynamic across longer time intervals than previously suspected [*Young et al.*, 2011; *Cook et al.*, 2013; *Mengel and Levermann*, 2014].

Such glacial modulation across the WSB for millennia would have not only served to promote the bed-depression overdeepening and interior-sloping basin floors characterizing the present-day WSB, but would also generate, erode and deposit gigatons sediment leading to reductions in topographic relief and effective stress with corresponding increases in subglacial till deformation, shear, and faster ice flow [*Alley et al.,* 1987; *Blankenship et al.,* 1986]. Ice sheet insulation combined with regional geothermal heat flux estimates on the order of 50 mW m^{-2} [*Siegert and Dowdeswell*, 1996; *Nyblade*, 1999; *Wright and Siegert*, 2012] predicts a wealth of subglacial water systems identified in the Wilkes Subglacial Basin by airborne radar and satellite remote sensing [*Wingham et al.*, 2006; *Carter et al.*, 2007; *Smith et al.*, 2009; *McMillan et al.*, 2013; *Wright et al.*, 2014]. Sediments play an important role in shaping subglacial water systems, as demonstrated by the discovery of a vast systems of canals in deformable sediment underlying Thwaites Glacier in West Antarctica [*Schroeder et al.*, 2013, 2014]. In that case, the sediment-floored canals reduced basal drag in comparison with sediment starved, concentrated subglacial channel systems downstream in a region of increased basal drag, greater scouring, and erosion.

In this study, I provide the first quantitative estimates for extent, thickness and potential character of WSB sedimentary basin deposits lying beneath the EAIS. The distribution, disposition, and magnitude of any such potential subglacial sedimentary deposits is an important control to establishing accurate basal hydraulic and geothermal flux models which, in turn, facilitate more accurate regional ice and climate models. To evaluate subglacial sedimentary basin boundaries, area, volume, and potential depositional controls, I integrate over 110,867 line kilometers of aerogeophysical data collected as part of NASA's IceBridge program and the ICECAP program across four austral field seasons between 2008-2013, combined with historical WSB aerogeophysical data flown during the WISE (Wilkes basin/transantarctic mountains System Exploration)-ISODYN (Ice-house Earth: Stability or DYNamism?) campaign of 2005-2006 [*Ferraccioli et al.*, 2009] and the WLK (Wilkes Land Transect) campaign of 1999-2000 [*Studinger et al.*, 2004; *Carter et al.*, 2009]. My purpose was to provide a comprehensive subglacial sedimentary baseline from which I might begin to more accurately estimate and evaluate WSB subglacial sediment quantity, distribution and character to more accurately assess potential destabilizing feedbacks in modeling ice flow.

4.3 DATA RECOVERY AND PREPROCESSING

Aerogeophysical platforms and equipment varied across field seasons as detailed in Table 4.1. The University of Texas-Austin ICECAP aerogeophysical surveys maintained consistent instrumentation and processing techniques throughout the four seasons of data used here. ICECAP flight profiles were designed in a radial pattern extending from the sea ice runway at McMurdo into the interior of the Southern Wilkes Basin in order to maximize the total aerogeophysical coverage area and cross historical surveys wherever possible. IceBridge aerogeophysical flight lines tracked historical ICESat satellite survey paths and have been incorporated into the data here where applicable.

Additional instrument altitude constraints were incorporated into flight survey design. While airborne gravimeters perform best when flying at a constant altitude, the 60 MHz ice-penetrating radar returns are significantly attenuated at altitudes exceeding 1000 m above the ice surface. Due to these instrumentation constraints and an ice surface relief exceeding 2500 m over the survey area, radial aerogeophysical survey flight paths were often flown at several consistent altitudes in a stair-stepped vertical profile. To help mitigate large aircraft acceleration impacts on the gravimeter, smooth altitude changes were generally performed over a distance of 25-35 km. The Bell BGM-3 gravimeter samples every 1 Hz (approximately every 90 m along track at Basler BT-67 airspeeds), an estimated precision of less than 3 mGal, and concurrent dual frequency carrier phase GPS data separately recorded at 0.1 m resolution for subsequent use in gravity data processing. The Geometrics 823A cesium vapor magnetometer was towed behind the aircraft in a 3 m tailboom to achieve a better than 1 nT precision and a track-line sampling distance of approximately 130 m. A three-axis fluxgate magnetometer was also installed to provide vector magnetic field data for subsequent use in cesium-vapor magnetometer data reduction. Topographic surface data were collected with a fixed, nadir-pointing laser altimeter allowing for 2D reconstruction of the ice surface elevation to within 0.25 m accuracy and an along-track sampling distance of 10 m. Ice-penetrating radar data were collected using a High Capability Radar Sounder (HiCARS) with a 60 MHz center frequency and 15 MHz bandwidth. Ice thickness estimates were obtained using coherent, synthetic aperture radar with a track-line sampling distance every 25 m.

Campaign	Platform	Radar	Gravity	Magnetics
WLK (UTIG/LDEO; 1999-2000)	Twin Otter (speed 65 m/sec)	UT/TUD 60-MHz (4 MHz bandwidth)	Bell BGM-3	Geometrics 823A cesium vapor (trailing bird)
WISE-ISODYN (BAS/PNRA; 2005-2006)	Twin Otter (speed 65 m/sec)	PASIN 150-MHz (12 MHz bandwidth)	ZLS (S-83)	Scintrex CS3 cesium vapor (wing tip)
ICECAP (UTIG/NERC/IceBridge; 2008-2011)	Basler BT-67 (speed 90 m/sec)	HiCARS 60-MHz (15 MHz bandwidth)	Bell BGM-3	Geometrics 823A cesium vapor (tail boom)

Table 4.1: Aerogeophysical equipment and platform specifications. BAS – British Antarctic Survey, LDEO – Lamont Doherty Earth Observatory, PNRA – Italian Programma Nazionale di Ricerche in Antartide, UTIG – University of Texas Institute for Geophysics.

Gravity reduction

Gravity data reduction and preprocessing was performed in accordance with methodologies developed and detailed in Holt et al. [2006] and Richter et al. [2001]. Raw gravity data from the BGM-3 was mapped with concurrent GPS data, time stamped, and then corrected for vertical or horizontal aircraft acceleration, yaw, pitch, and roll. An

Eötvös correction was then applied to account for the acceleration resulting from the Earth's rotation relative to WGS-84 such that the gravity meter and the source are vertically aligned. Data were smoothed with a finite impulse response low-pass filter with a half-amplitude frequency point of 0.0054 Hz (185 seconds) resulting in an estimated spatial resolution of 7.9 km. The gravity signal was then corrected for aircraft altitude using the theoretical spheroid gravity algorithm developed by Featherstone [1995]. Final edits of the preprocessed gravity results were completed by cross-over error assessment, visual analysis of the plotted data, and root-mean-square (RMS) analysis. Often the beginning of a line had to be trimmed to reduce the RMS, or in some cases, entire lines had to be removed from the dataset because of excessive in-flight turbulence.

The resultant free-air gravity disturbance for the WSB was leveled to a consistent data elevation of 3950 m above the ellipsoid, to correspond to the highest aircraft altitude flown during the composite WSB aerogeophysical surveys, to provide consistent spectral content for subsequent power spectra analysis using Generic Mapping Tools (GMT) [*Wessel and Smith*, 1998]. At the 3950 m upward continued elevation, the closest bedrock sources would yield an expected resolvable geologic wavelength of ~6.5 km for ideal flight conditions based upon calculations for different basin widths using formulas developed by Childers et al [1999]. Following leveling and upward continuation, RMS crossover errors were reduced to less than 3 mGals with an estimated spatial resolution of 9 km. Resultant upward-continued free-air gravity data were then gridded at 2 km using a minimum curvature approach, and plotted (Figure 4.2) using Geosoft's Oasis montaj® software suite.

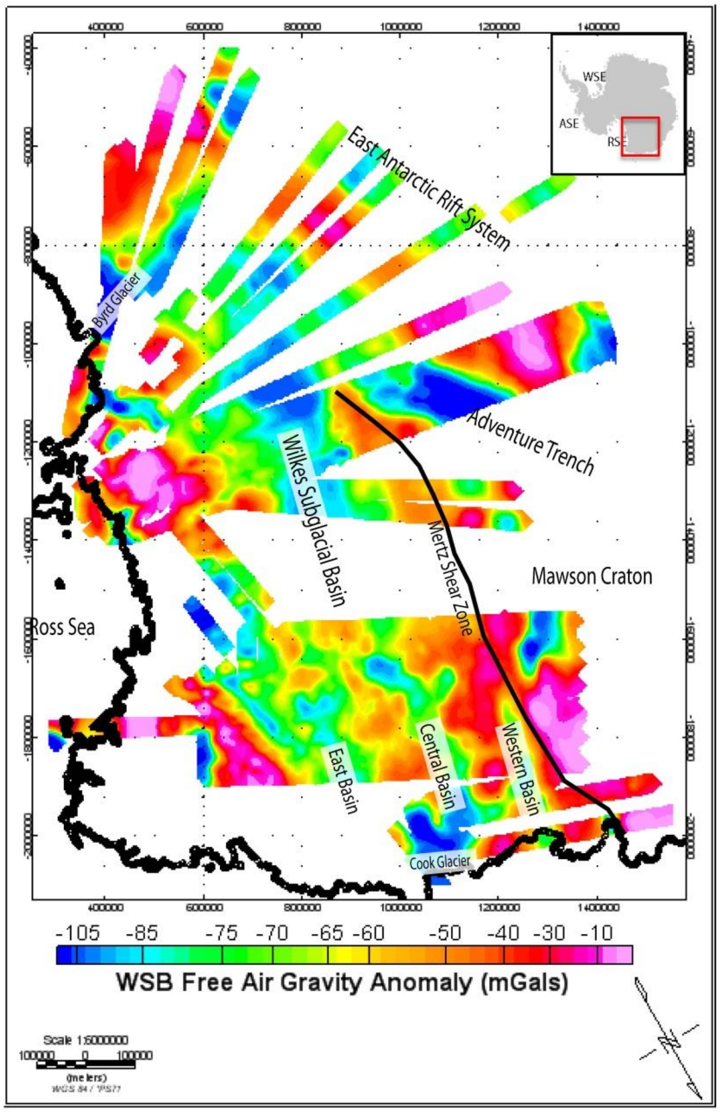

Figure 4.2: Wilkes Subglacial Basin Free-Air Gravity (mGals) ICECAP and WISE-ISODYN datasets leveled to 3950 m.

Magnetics reduction

Aeromagnetic data were processed using standard methodologies including diurnal and IGRF corrections followed by subsequent leveling to minimize cross-line differences. While the IGRF model details very long wavelength and scale variations in the Earth's magnetic field, and diurnal variations in the Earth's magnetic field occur across much more finite (daily) time intervals, it should be noted that neither magnetic data reduction technique can fully account for magnetic measurements variability across a 4-year aerogeophysical program. Persistent variability in cross-line differences in the magnetic dataset may be the result of flight altitude differences, equipment configuration changes between field seasons, or imperfect removal of the diurnal field [*Minty*, 1991]. Once levelled, magnetic data were interpolated and gridded using a minimum curvature method with a cell size of 2 km, draped on the composite Bedmap2 bed topography at an interval of 3950 m, and displayed in Figure 4.3 with individual datasets merged into a single composite grid.

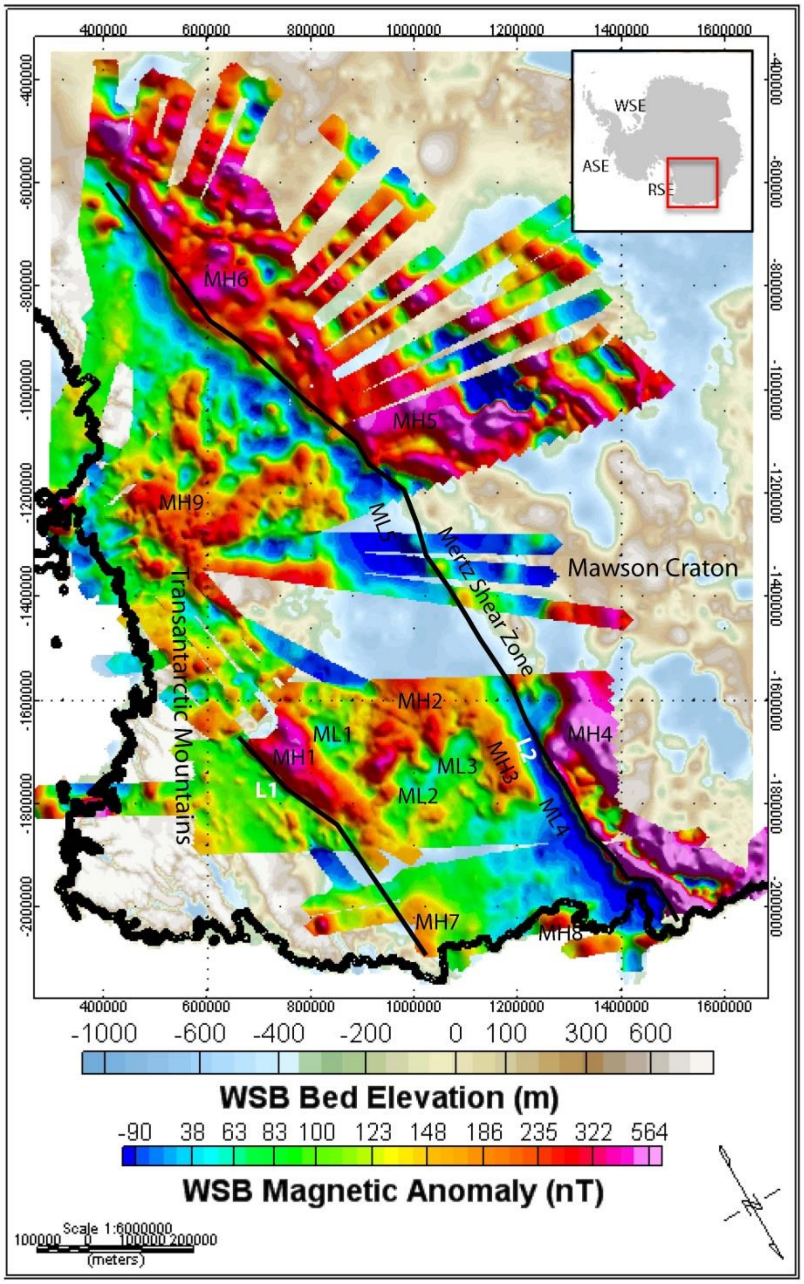

Figure 4.3: Wilkes Subglacial Basin Leveled Magnetic Data ICECAP, WLK and WISE-ISODYN surveys draped on Bedmap2 bed topography. Major aeromagnetic anomalies and lineaments have been labeled consistent with *Ferraccioli et al.*, [2009] and *Jordan et al.* [2013].

Radar reduction

Airborne ice-penetrating radar data from multiple surveys were pulse-compressed, processed using a short synthetic-aperture radar aperture to retain energy, and compiled regionally to achieve range distortions below 400 m. Ice thicknesses were calculated assuming a speed of light in ice of 169 m/μs^{-1}, and the bed elevation calculated relative to the coincident surface reflections. Bedmap2 models for ice surface and bed topography [*Fretwell et al.*, 2013] were augmented with ice-penetrating radar data collected during ICECAP/IceBridge field seasons 2010-2013. The latest ICECAP/IceBridge radar data were gridded at a spacing of 5 km and sutured to regional Bedmap2 gridded data using Geosoft's Oasis montaj® Gridknit extension. The updated Bedmap2 dataset was then interpolated using a natural neighbor algorithm [*Watson*, 1992] at to facilitate incorporation into 3D structural models for subsequent gravity reduction.

4.4 GEOPHYSICAL ANALYSIS AND MODELING

Bouguer anomaly estimation

The Bouguer anomaly maps out the density variations not due to known topographic loads.

In this case, complete terrain-corrected Bouguer gravity anomalies were derived using a Parker-Oldenberg approach [*Parker*, 1973; *Oldenburg*, 1974] to produce a 3D forward model based on updated Bedmap2 ice and bed topographies that was then used to reduce the free-air data with average ice and crustal densities of 0.92 g/cc and 2.8 g/cc [*Studinger et al.*, 2004; *Filina et al.*, 2006], respectively. These resultant Bouguer gravity anomalies do not reflect data over floating ice, as water depths were not adequately constrained and potential Bouguer data along the continental margin was not required in construction of an interior WSB sedimentary basin model. The Parker-Oldenberg algorithms, included as part of Geosoft's Oasis montaj® software suite, estimate the gravitational effects of topography using LaFehr's [1991] curvature correction with intermediate zones (1-8 grid cells from the gravity station) calculated using the flat-topped square prism approach [*Nagy*, 1966], and the far zone (>8 grid cells from the gravity station) terrain effect calculated using the annular ring segment approximation of [*Kane*, 1962]. Bouguer gravity results are gridded and displayed in Figure 4.4 using similar resolution and techniques as for free-air gravity results.

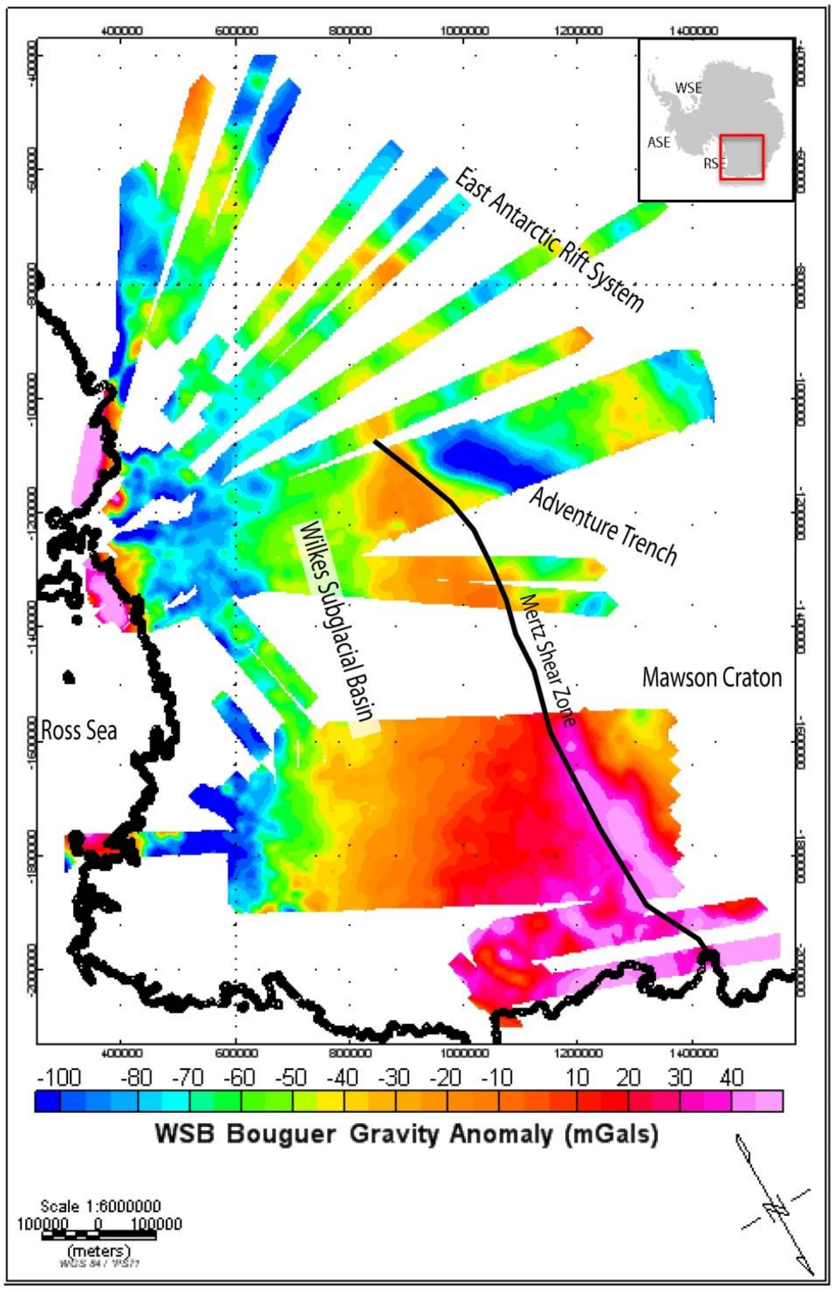

Figure 4.4: Wilkes Subglacial Basin Bouguer Gravity (mGals) anomaly ICECAP and WISE-ISODYN datasets leveled to 3950 m.

Free Air Gravity spectral analysis

As the frequency content of a potential field changes with distance from the source, I exploit the spectral content of our potential fields data to estimate the depth of major interfaces.

Spectral analyses of free-air gravity data were assessed to estimate the depth of major interfaces based upon changes in the frequency content of potential fields relative to the distance from the source. This methodology was based upon prior potential field analytics established by Damiani, et al. [2014], Fairhead and Okereke [1988], Karner and Watts [1983], and Spector and Grant [1970]. The radial power spectrum of the free-air gravitational response was plotted as the natural log of power versus wavenumber. Least squares line segments were fit to slope breaks to determine representative crustal density boundary depths using the equation $h= -s/4\pi$, where h = depth to source and s = slope of the (natural log) energy spectrum (Figure 4.5).

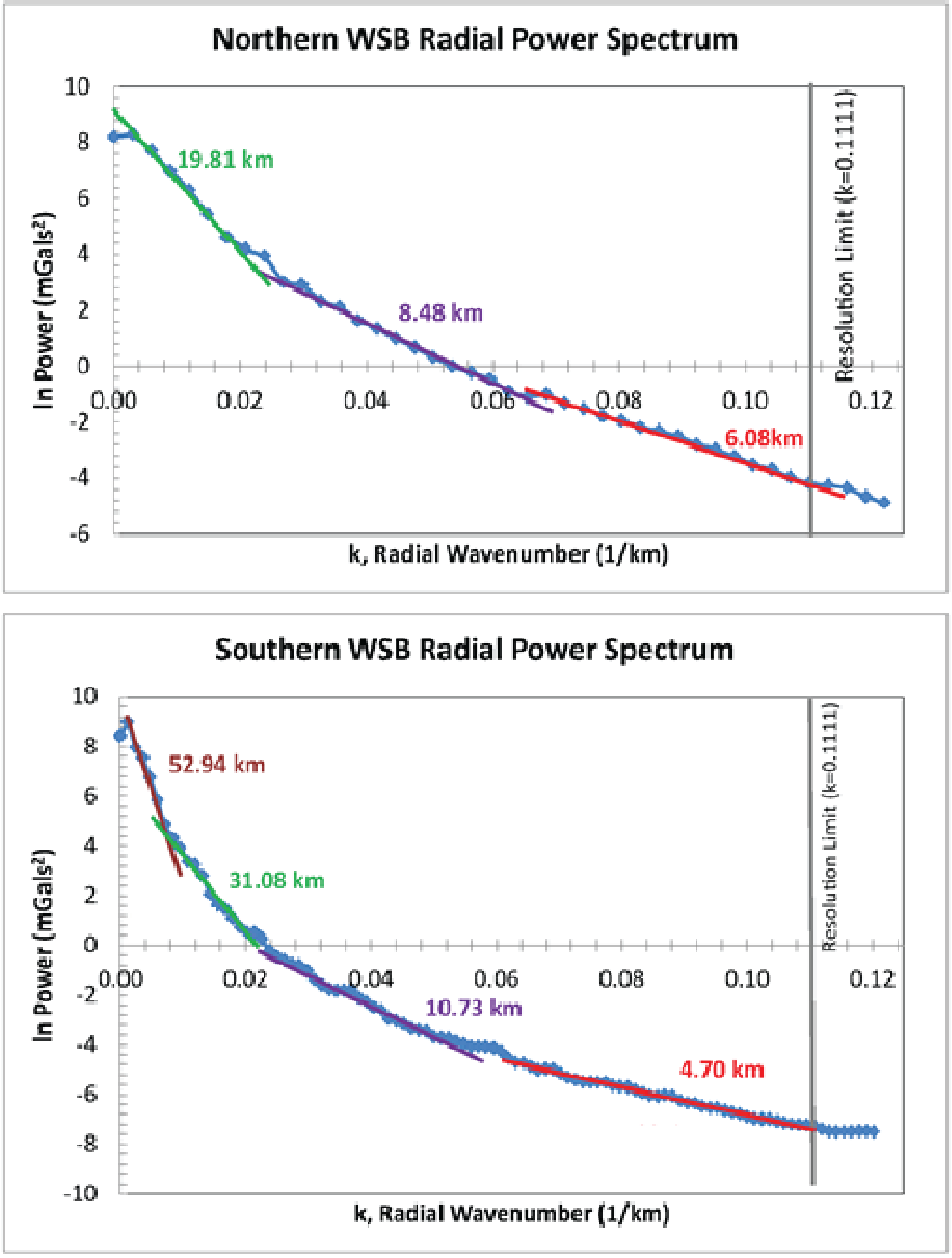

Figure 4.5: Wilkes Subglacial Basin Free-Air Gravity Radial Power Spectrum Depth Estimates Average of slope energy spectrum showing two distinct source areas – crust (purple) and mantle (green). Note the increasing Moho depth toward the WSB interior.

With each resultant slope indicative of the characteristic power spectrum, breaks in slope identify a density change at a boundary of specified wavelength or wavenumber [*Damiani et al.,* 2014; *Spector and Grant,* 1970]. Depth estimate-wavenumber correlations confirm lithospheric sources at the base of the sedimentary basin-crust and crust-mantle interfaces only for the Ross Age extended terrain of the WSB. A closer evaluation of the free air gravity power spectra response of the Northern and Southern WSB reveal an increase in crust and lithospheric thickness extending toward the Southern interior of the basin.

Isostatic anomaly estimation

The isostatic gravity anomaly maps out departures of the gravity field from that generated by topography supported by variations in the thickness of the crust. As such, this method may highlight variations in the density of the crust, a key indicator for sedimentary basins.

Isostatic gravity anomalies were calculated to accentuate gravity field departures generated by topography and supported by crustal thickness variations by adding a simple Airy-based Moho surface estimate to the 3D structural model [*Jachens, and Griscom*, 1985]. Resulting regional WSB Airy isostatic gravity anomaly estimates highlight potential crustal density anomalies as key initial indicators for subglacial sedimentary basins (Figure 4.6). Airy isostatic corrections implemented an elastic thickness component of 90 km [*Stern and ten Brink*, 1989] as a best estimate to account for the limited to moderate downward Moho deflection of a Proterozoic-age lithosphere having undergone Cretaceous extensional forces and significant Cenozoic erosion and scouring [*Jordan et al.*, 2013]. Airy Moho depth estimates of 20-30 km were found consistent with recently published Wilkes Land regional models by Lloyd et al. [2013] and Baranov and Morelli [2013]. Geosoft's Oasis montaj® software was employed with

ICECAP/IceBridge/WISE-ISODYN/WLK airborne survey free-air gravity data as input to calculate the residual gravity anomaly based on the complete 3D structural model using ice, crust and mantle densities of 0.92, 2.8, and 3.3 g/cc, respectively.

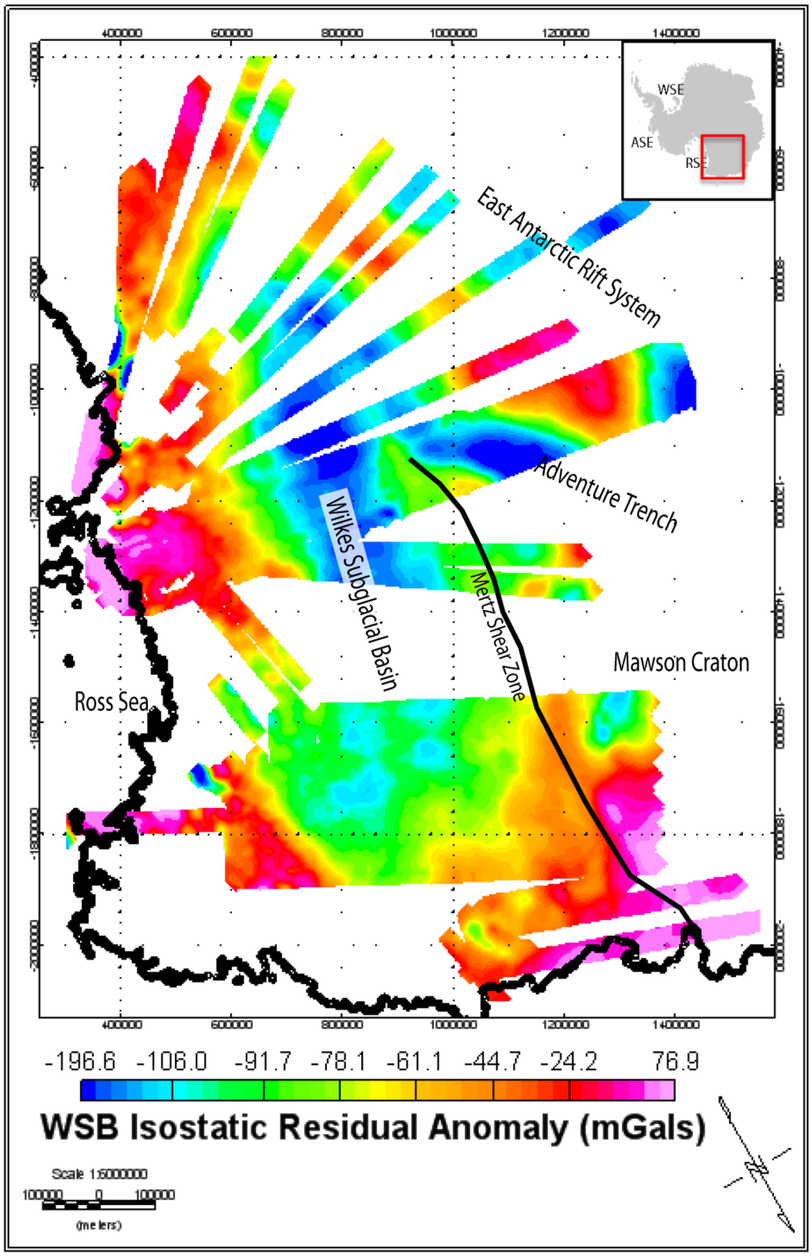

Figure 4.6: Wilkes Subglacial Basin Residual Airy Isostatic Corrected Gravity (mGals) anomaly ICECAP and WISE-ISODYN datasets leveled to 3950 m with the inferred Mertz Shear Zone location.

Total magnetic anomaly interpretation

Regional magnetic anomaly data were compiled for the entire WSB including ICECAP/IceBridge and the historical WISE-ISODYN and WLK surveys as detailed in Ferraccioli et al [2009] and Studinger et al [2004]. Major magnetic anomalies and lineaments were identified and labeled consistent with nomenclature established by Ferraccioli et al [2009]. Although the extensional tectonic controls concerning the origins of the WSB have long been debated with hypotheses of lithospheric flexure, crustal thinning and structural controls dominating the literature [*ten Brink and Stern*, 1992; *Ferraccioli et al.*, 2001, 2009], aeromagnetic features were identified and summarized here for the entire WSB to best provide lateral constraint for subsequent subglacial sedimentary basin modeling.

Beginning along the northern George V coastline, notable features include magnetic highs (MH7 and MH8) first identified by Damaske et al [2003]. Based upon limited outcrops and the prior of Roland [1991], Damaske et al [2003] suggested that the MH7 anomaly may be related to either a) significantly thick portions of dolerite sill, b) ice-covered Jurassic Kirkpatrick Basalts, or c) thicker Jurassic mafic feeder bodies. With a more concentrated aeromagnetic grid, Damaske et al [2003] described the WNW-ESE trending MH8 magnetic anomaly as notably more enigmatic with no direct correlation to outcrop. The same N-S trending magnetic anomaly high (MH4) that Ferraccioli et al [2009] showed to extend across the western boundary of the WISE-ISODYN survey is shown here (Figure 4.3) to define the western edge of the WSB across some 1900 km. This feature, flanked by a prominent magnetic lineament (L2), is interpreted to define the extension of the Mertz Shear Zone (MSZ) Fault system extending from the George V coastline to the South Pole region. Based upon regional geologic conjugate margin hypotheses advanced by Aitken et al. [2014], Boger [2011], and White et al. [2013], the MSZ delineates the eastern extent of the Late Archean Mawson Craton underlying much of the EAIS from the WSB defined by Cenozoic extension and reworked passive margin sedimentation.

Another magnetic anomaly high, trending NW-SE across the eastern margin of the WSB and flanked by magnetic lineament L1 was first identified by Damaske et al. [2003] and then Ferraccioli et al [2009] to be associated with Ross Age magmatic arc intrusions associated with the Prince Albert Fault System and the formation of the Prince Albert Mountains to the south. High frequency magnetic anomaly highs associated with MH2 were observed coincident with broad mesa subglacial topography and were interpreted to be characteristic of Becon Supergroup lithologies massively intruded by Jurassic-age Ferrar tholeiites [*Ferraccioli et al.*, 2009].

With insufficient rock outcrops in the Southern WSB, geologic interpretation of associated magnetic anomaly data is sparse in historical literature. Lateral changes in magnetic anomaly texture, representing different wavelength content, can be distinguished across the region however. Of particular note is the broad change in magnetic anomaly character across the Southern WSB from east to west. From the TAM extending west into the WSB interior (MH9), the magnetic response is characterized by a broad magnetic anomaly high with short to long wavelength positive anomalies ranging from 5-10 km (+/-50 nT) to 100 km (100-250 nT) as detailed by Studinger et al [2004]. Longer wavelength magnetic anomalies are generally interpreted to represent deep crustal response (>10 km depth) with shorter amplitudes characterizing shallower source depths of 1-10 km. The change in magnetic anomaly character from east to west approaching the MSZ (from MH9 to ML5 to MH5) is notable for the dramatic increase in amplitude and wavelength indicative of the transition from extended sediment draped crust in the WSB to the thick, Late Archean Mawson Craton.

Depth to magnetic basement

The same principle applied in the spectral analysis of the gravity data referred to above can also be applied to magnetics data to assess the depth to magnetic (presumably crystalline) basement.

Biased sampling inherent in the ICECAP variable flight line spacing precluded a full 3D DTB deconvolution due to variable wavelength information. The 2D Werner deconvolution method here utilizes a moving window of specific width and distance between each analysis (Table 4.2) such that the depth estimate returned directly corresponds to the window size.

	Window sizes (km)	**Window Shift (km)**	**Depth – min/max (km)**
Short Wavelength	1,3,5	0.5	0.5, 5
Medium Wavelength	5, 10, 15	2.5	2, 15
Long Wavelength	10, 20, 30	5	5, 30

Table 4.2: Wilkes Subglacial Basin Magnetic Depth to Basement Specifications

As a result of the direct, positive correlation between window size and depth estimates, three passes over the magnetic data were performed at three different wavelength/window sizes to capture the full suite of depths characterizing the WSB. DTB solutions exceeding the window width, or shallower than the sample interval are not likely to be valid, hence source depths less than 50% of the narrowest window or more than 50% of the largest window width were discarded. To reduce noise in the short wavelength spectrum, a noise limit was implemented to reject analyses if the RMS anomaly amplitude did not exceed 20 nT. While DTB errors are difficult to quantify, calculated source depth estimates may vary on the order of 20-40% [*Kilty*, 1983].

Exploiting the high data density and consistent sampling along flight transects, magnetic DTB estimates were derived via Werner 2D deconvolution methods for short, medium, and long wavelengths [*Ku et al.*, 1983]. DTB contact and dike solutions for all wavelengths were assessed against Geosoft's GM-SYS® gravity modeling solutions for comparison and vertical constraint. Long DTB wavelength solutions were found to most accurately track depths to crystalline basement (as indicated in Figure 4.9) and are thereby displayed in map view in Figure 4.7 direct gridded at 20 km.

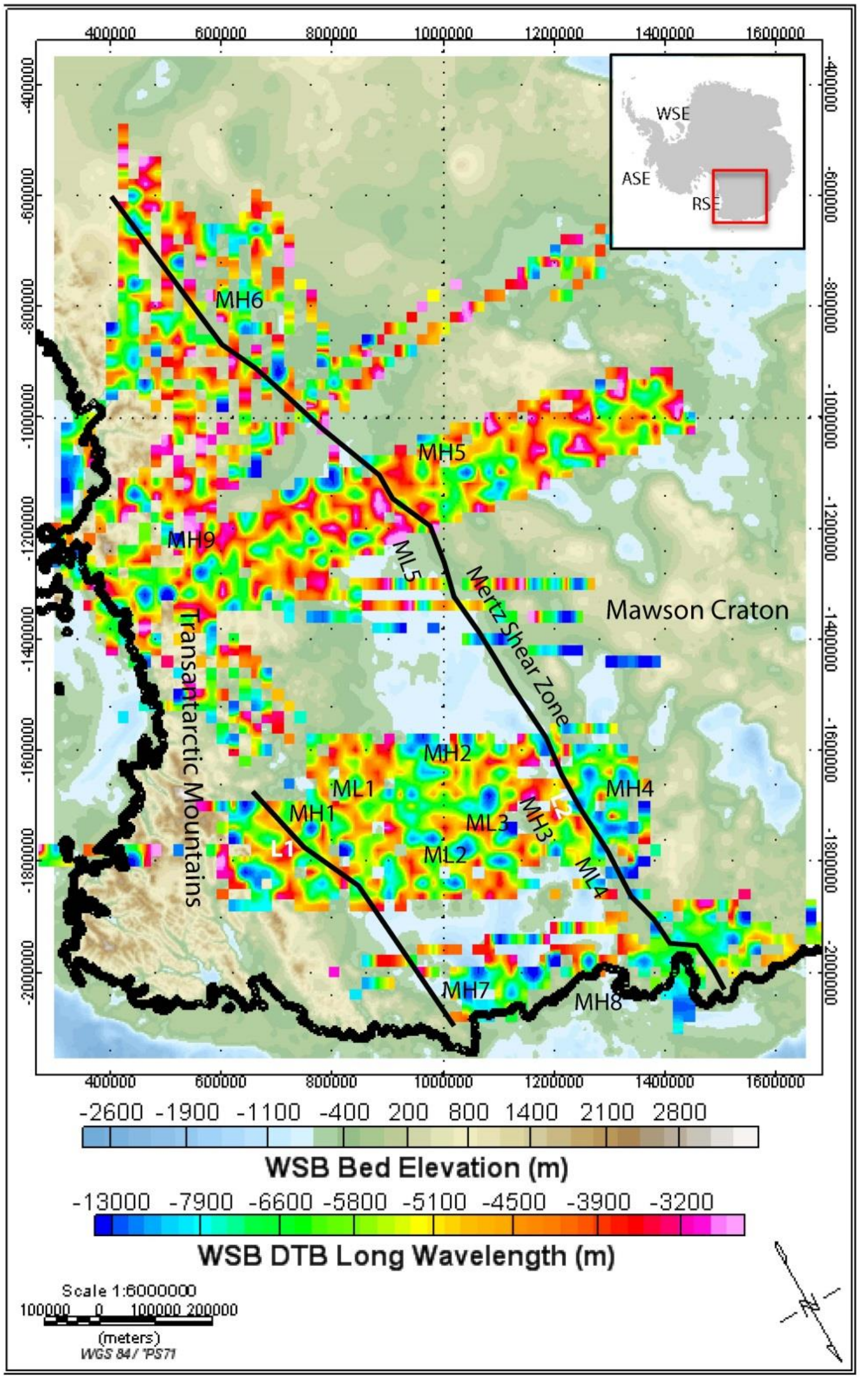

Figure 4.7: Wilkes Subglacial Basin Magnetic DTB long wavelength estimates via Werner 2D deconvolution with direct gridding at 20 km. Bedmap2 bed elevations displayed as background.

Basal roughness

Topographic roughness was also evaluated using the 60 MHz and 150 MHz coherent ice-penetrating radar data from the combined aerogeophysical surveys. By assessing RMS deviation (v) results defined as the RMS difference in height separated by a step (Δx) and given by:

$$v(\Delta x)=\{1/n\Sigma[(z(x_i)-z(x_i+\Delta x)]^2\}^{1/2} \tag{1}$$

where n is the number of sample points, $z(x_i)$ is the height of the surface at point x_i [*Shepard et al.*, 2001; *Young et al.*, 2011]. Roughness of the subglacial bed topography was estimated with RMS deviation over a discrete length of 1600 m for which the heights of a rough surface are correlated with each other (Figure 4.8). Smooth regions appear blue while rough, topographic highs appear white or red.

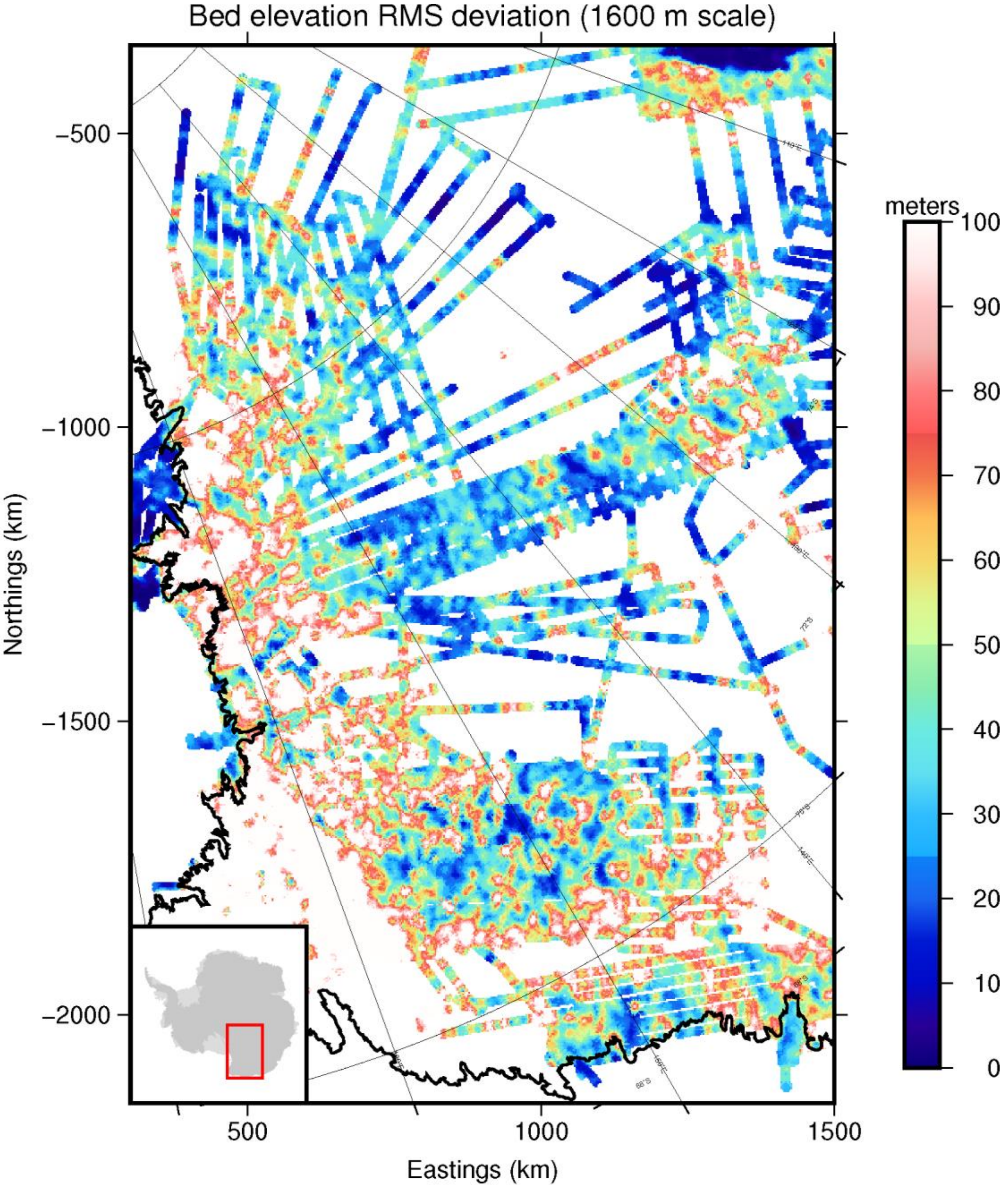

Figure 4.8: Wilkes Subglacial Basin Radar Roughness Sediment Mask – 1600 m length scale.

Sedimentary basin thickness modeling

WSB sedimentary basin thickness estimates were initially attempted using 3D steepest descent inversion techniques, however, the variable distance between radial flight line patterns resulted in a wavelength bias in the datasets and errant inversion results. Hence, 2D forward modeling of free-air gravity data were performed using Geosoft's GM-SYS® modeling package [*Talwani and Ewing*, 1960] using modeled densities consistent with historical research - ice (0.92 g/cc), sediment (2.35 g/cc), crust (2.8 g/cc), and mantle (3.3 g/cc). Topographic surfaces for ice, bed, and Airy-derived Moho surfaces were held fixed with iterative inverse solutions performed on the model until the error between the calculated and measured gravitational response was approximately 3 mGals or less. The resultant 2D subglacial sedimentary basin isopach estimates were calculated along track, interpolated and gridded using a minimum curvature method with a cell size of 2 km (Figure 4.9).

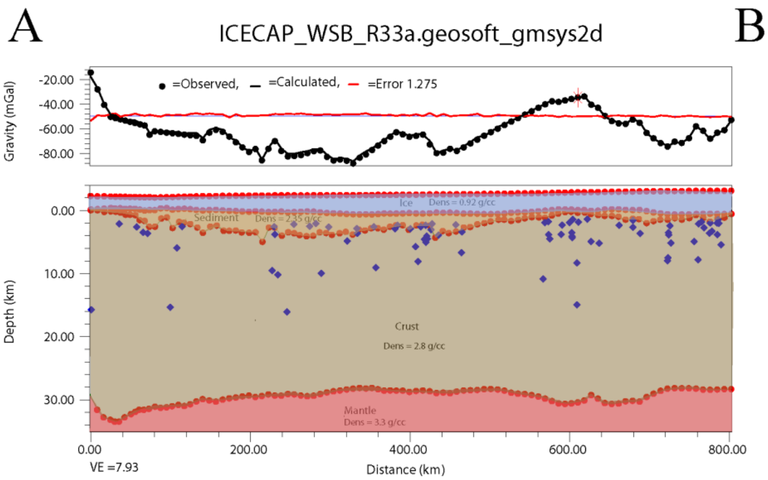
A
ICECAP_WSB_R33a.geosoft_gmsys2d
B
Gravity (mGal)
-20.00
-40.00
-60.00
-80.00
=Observed,
=Calculated,
=Error 1.275
Ice Dens = 0.92 g/cc
Sediment Dens = 2.35 g/cc
Crust
Dens = 2.8 g/cc
Mantle
Dens = 3.3 g/cc
Depth (km)
0.00
10.00
20.00
30.00
0.00
200.00
400.00
600.00
800.00
VE =7.93
Distance (km)

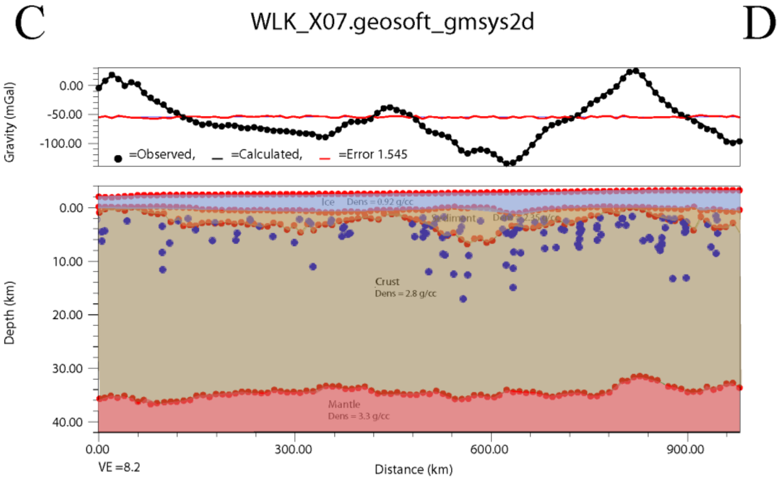
C
WLK_X07.geosoft_gmsys2d
D
Gravity (mGal)
0.00
-50.00
-100.00
=Observed,
=Calculated,
=Error 1.545
Ice Dens = 0.92 g/cc
Sediment
Crust
Dens = 2.8 g/cc
Mantle
Dens = 3.3 g/cc
Depth (km)
0.00
10.00
20.00
30.00
40.00
0.00
300.00
600.00
900.00
VE =8.2
Distance (km)

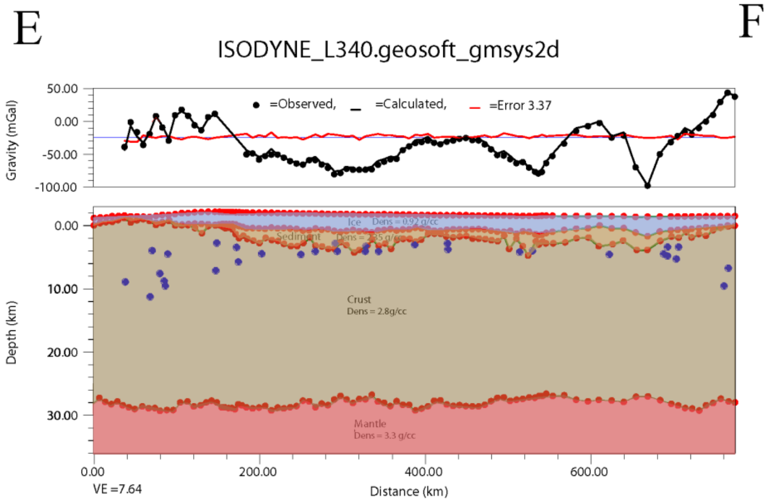
E
ISODYNE_L340.geosoft_gmsys2d
F
Gravity (mGal)
50.00
0.00
-50.00
-100.00
=Observed,
=Calculated,
=Error 3.37
Ice Dens = 0.92 g/cc
Sediment Dens = 2.35 g/cc
Crust
Dens = 2.8g/cc
Mantle
Dens = 3.3 g/cc
Depth (km)
0.00
10.00
20.00
30.00
0.00
200.00
400.00
600.00
VE =7.64
Distance (km)

Figure 4.9: Wilkes Subglacial Basin 2D GM-SYS® Forward Gravity Model Profiles with Magnetic DTB results (see Figure 10 for map profile transects) – Red dots represent model horizons with densities posted. Black dots represent observed free-air gravity with modeled gravity depicted as a black line. Error across the 2D model depicted as a red line. Blue circles represent magnetic DTB contact and dike results for magnetic anomaly long wavelengths.

Initial stratigraphic model densities were constrained with prior seismic and gravity research in the WSB region [*Ferraccioli et al.*, 2001] and compared to theoretical estimates [*Bahr et al.*, 2001]. Moho depths initially derived from simple Airy isostatic calculations were manually smoothed, and basin depths adjusted accordingly until modeled gravity results reflected observed. Because 2D forward gravity modeling is non-unique, the initial layered density models were kept as simple as possible. Resulting sediment isopachs for each 2D flight line were compiled and subsequently interpolated using a minimum curvature technique with 2 km grid spacing (Figure 4.10).

A significant variation in modeled sediment densities was discovered in published literature for Wilkes Land, prompting an evaluation of sediment densities from 1.85 g/cc [*Filina et al.*, 2008] to 2.4 g/cc [*Ferraccioli et al.*, 2001] to assess 2D forward model basin response relative to supplemental data constraints including magnetic DTB. Empirical examination of probable sediment densities at these burial depths with an average of 2 km of overlying ice, equivalent to effective pressures on the order of 70-90 MPa, resulted in subglacial sediment densities of 2.3-2.4 g/cc and estimated sediment porosities of 15-18% [*Gueguen, Y. and Palciauskas*, 1994; *Bahr et al.*, 2001; *Zoback*, 2010]. Based on these empirical estimates and prior modeled WSB sediment densities [*Ferraccioli et al.*, 2001; *Studinger et al.*, 2004], final gravity models were constructed using a subglacial sediment density estimate of 2.35 g/cc resulting in average sedimentary basin thicknesses for the Northern and Southern WSB of 1,144 m +/- 179 m and 1,623 m +/- 254 m, respectively. Gravity modeling across more finite sub-basins, including the East (~2 km), Central (~3 km), and Western (~4 km) basins in the Northern WSB [*Ferraccioli et al.*, 2009], the Southern WSB (~5 km), and the Adventure

Subglacial Trench (>7.5 km) contained substantially thicker sediment thicknesses as detailed in Figure 4.10.

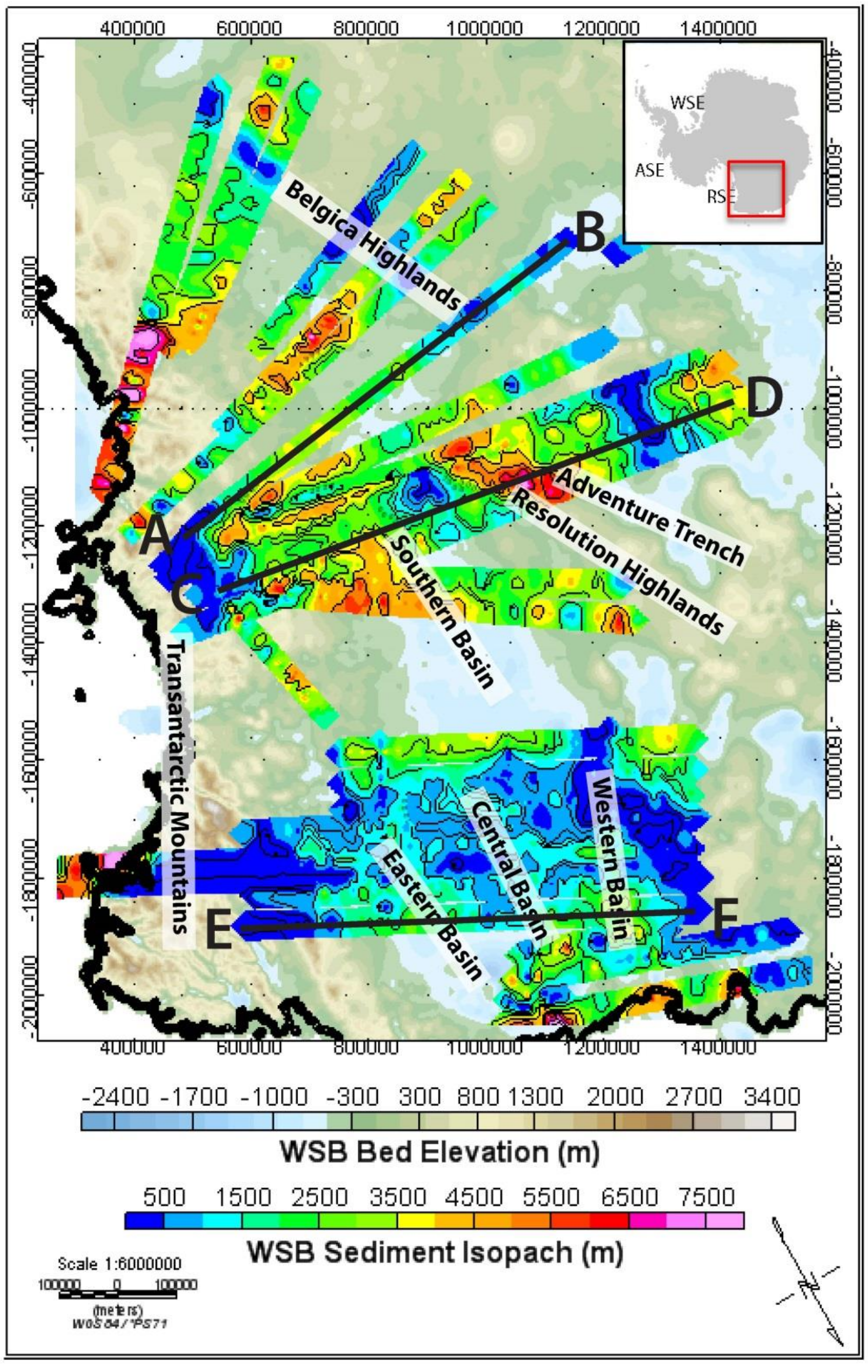

Figure 4.10: Wilkes Subglacial Basin Sediment Isopach (meters): 2D GM-SYS® gravity model transects also shown (Figure 4.9).

Uncertainty Estimation

While depth to magnetic basement and radar roughness estimates can be utilized to constrain vertical and horizontal subglacial sediment distribution models, respectively, inversion of gravity anomalies is inherently a nonunique solution with sizeable trade-offs between density and geometry. Using a nonlinear approach to solving the inverse problem, density contrasts were established between geologic interfaces and the inversion constrained with depths at isolated points along the interface [*Leao et al.*, 1996]. Despite this, gravity inversion equations remain ill posed, such that instead of presenting a finite solution uncertainty estimates were quantified to assess the validity of the inverse problem.

Densities for ice, crust and mantle (0.92 g/cc, 2.8 g/cc and 3.3 g/cc, respectively) were determined based upon regional, historical analyses [*Studinger et al.*, 2004; *Filina et al.*, 2006], while estimated sediment densities of 2.3 – 2.4 g/cc [*Gueguen, Y. and Palciauskas*, 1994; *Bahr et al.*, 2001; *Zoback*, 2010] yielded results most consistent with magnetic DTB estimates. East-west flight profiles were inverted using the Parker-Oldenberg gravity inversion algorithms included as part of Geosoft's Oasis montaj® software suite constrained with radar ice thickness data and laser derived topography. Initial results with no basal depth range constraints provided good agreement between the computed and observed gravity anomalies with error reduced to 0.04 in the Figure 4.11 profile example resulting in an average sediment thickness of 2,209 m +/- 180 m. While the variability of the depth values was initially large, depicted by the blue vertical lines on Figure 4.11, these uncertainties were subsequently minimized by constraining the minimum and maximum depths of the bedrock surface using vertical magnetic DTB limits to the upper and lower bounds of sediment thickness. Several statistical measures of uncertainty, including mean, variance, and standard deviation, were calculated herein based upon the multitude of inverse models generated. Consistent with the findings of Roy et al. [2005], we found the uncertainty estimates of density models inverted from gravity data does not accentuate the limitations of the inversion process, but actually strengthens the reliability of the results.

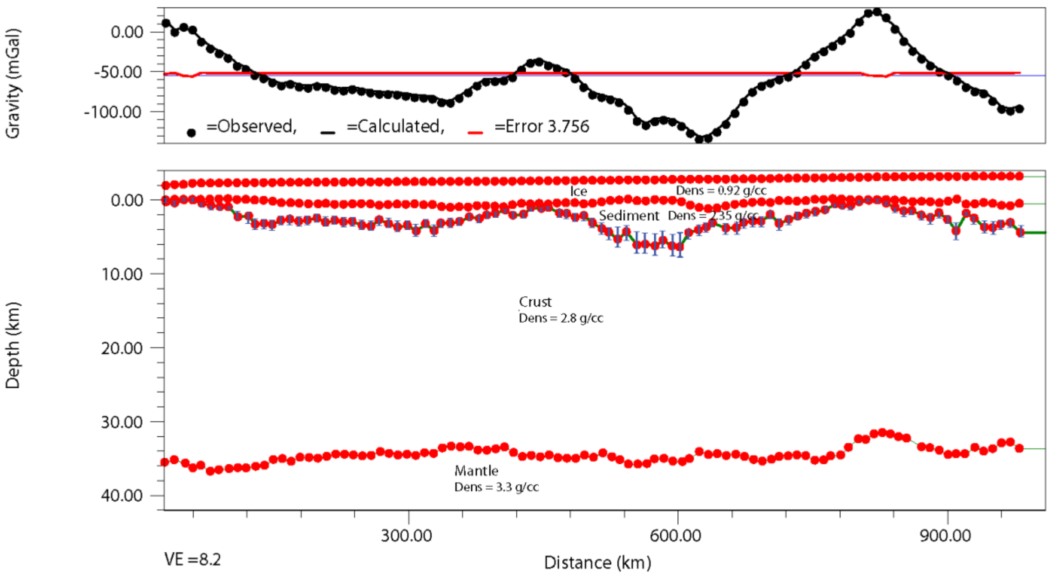

Figure 4.11: Results of inversion of gravity data along profile C – D (Figure 4.10) of the Wilkes Subglacial Basin. Observed and computed anomaly and corresponding model with variance represented as vertical bars.

4.5 DISCUSSION

Crustal structure from free air and Bouguer gravity:

WSB airborne free-air gravity results (Figure 4.2) reflected bed topography as would be expected with free-air gravity lows corresponding to topographic bed elevation lows in the basin and free-air gravity highs corresponding to topographic bed elevation highs. Of particular note are the three Northern WSB basins, east, central, and western, that Ferraccioli et al [2009] identified with regional free air anomalies on the order of ~-60 mGals and a central, interior Southern WSB gravity low exceeding ~150 mGals. The Transantarctic Mountains are characterized by strong positive free air anomalies averaging 50-60 mGals, with local negative anomalies <-100 mGals typify the Cook and Byrd glacial valleys.

By removing the free air topographic bias in the gravity data and further isolating the geologic signal, the Bouguer gravity results (Figure 4.4) reflect both increasing ice load toward craton interior and typical thinner continental crust at the rifted, passive, continental margins, particularly notable at the Southern Ocean and Ross Sea, respectively. Within the Northern WSB a general east to west increasing trend in Bouguer anomalies is noted from ~-100 mGal to 100 mGal. The western boundary of the Northern WSB is demarcated by the MSZ and the associated positive Bouguer response thereby extends some 900 km to the south. Bouguer anomalies decline substantially to ~-70 mGals in the central Southern WSB sub-basin and to <-200 mGals in the Adventure Subglacial Trench. The fringes of a deep interior basin termed the East Antarctic Rift system (EARS) by Ferraccioli et al. [2011] can also be distinguished toward the end of the ICECAP radial flight lines with a distinct negative Bouguer response of ~<150 m Gals. Both the EARS, Adventure Trench, and Southern WSB are characterized by low bed roughness (Figure 4.8) indicative of smooth sedimentary basal ice conditions. In contrast, the extensional, faulted Northern WSB crust, presumably thinner sediment drape, and associated MSZ tectonism has resulted in elevated bed roughness and coarser subglacial basal ice conditions for all but the East, Central, and Western sub-basins identified by Ferraccioli et al [2009] and the Cook and Mertz glacial catchments.

Spectral analyses of the free-air gravity anomalies in the Northern and Southern WSB (Figure 4.5) were completed prior to designing the 3D structural model necessary to correct for Airy-style isostatic flexure of the lithosphere. To assess the probability of a mid-crust discontinuity gravity power spectra was plotted against wavenumber to reveal just one subtle change in slope at a lithospheric depth associated with the Crust-Moho boundary [*Damiani et al.*, 2014]. Based on the resultant least squared line segment slopes, the best fit Moho depths for the WSB fell between 20-31 km with no apparent mid-crust discontinuity as would be expected from the Proterozoic EAIS lithospheric craton. Crust and lithospheric thickness increased toward the southern interior of the WSB, with the base of crust increasing from 8.48 to 10.73 km and the Moho depth increasing from 19.81 to 31.08 km. More finite spatial changes in lithospheric boundaries, across the WSB based on spectral analysis, were not performed as a result of the variable wavelengths inherent in the airborne gravity data due to the radial flight pattern. Regional body wave tomography analyses confirm our spectral analysis results here with recorded Moho depths on the order of 25-35 km for the WSB [*Baranov and Morelli*, 2013; *Lloyd et al.*, 2013] and no mid-crustal density contrast. While Bannister et al. [2003] found mid-crustal discontinuities in the Transantarctic Mountains at approximately 8-14 km depth, the associated seismic velocity boundary did not extend west into the East Antarctic craton and WSB.

Geological context from isostatic anomalies and magnetic anomalies

Because expansive ice loads often result in a direct isostatic response [*Watts*, 2001], lithospheric flexure associated with WSB basal topography and ice loads was estimated using a standard 3D Airy model for the Moho boundary and the results from generalized constraints revealed during the gravity power spectra analysis (Figure 4.5). The resultant isostatic residual gravity deficiencies <-150 mGals, in the Southern WSB interior and the subglacial Adventure Trench are reflective of mass deficiencies in the model. Isostatic residual gravity presented here reflect the characteristic N-S anomaly trend of the WSB contrasted with the NW-SE regional trend of the subglacial Adventure Trench and the EARS, suggesting disparate structural controls between the basins. Regional faults appear generally associated with rifted lithospheric zones in the WSB indicating potential overcompensation of Moho depth at these suture zones in our model (Figure 4.6). Deep glacial valleys, including Cook and the adjacent Mertz glacier, appear to have exploited N-S trending geologic structures during reactivation associated with the WAR plate tectonic extension in the Northern WSB to cut across the basin bounding MSZ in the area of the western-central basins originally identified by Ferraccioli et al [2009]. Significant low isostatic residual gravity anomalies also appear toward the ends of several ICECAP flight lines across the Southern WSB, potentially associated with a sizeable subglacial sedimentary basin in the EARS region. Given the lack of recent volcanism and characteristically low mantle-derived geothermal flux for the East Antarctic craton in the Wilkes Land region [*Pollard et al.*, 2005], the negative isostatic anomalies over the relatively cool crust could most likely be attributed to low-density bodies of a range of compositions [*Aitken et al.*, 2014; *Damiani et al.*, 2014]. Such negative residual isostatic gravity anomalies are used subsequently herein to laterally constrain sedimentary basin isopachs derived from 2D forward gravity models.

Leveled aeromagnetic data draped to the subglacial topographic bed surface was utilized to define regional faults across the WSB (Figure 4.3) to gain a better understanding of potential lithologies and associated lithologic densities that might laterally constrain sedimentary deposition and facies. Regional faults were identified based on conjugate margin structural reconstruction by Aitken et al. [2014] and structural interpretation of the Northern WSB following the WISE-ISODYN aerogeophysical survey by Ferraccioli et al. [2009]. The MSZ is undoubtedly the most extensive, significant structural boundary in the region that establishes the western boundary of the Ross Orogen magmatic activity [*Gibson et al.*, 2013] while defining the western extent of the WSB separating the Mawson Craton from the reworked passive margin sediments in the WSB interior [*White et al.*, 2013]. Extending across the Southern Ocean, the MSZ represents a strike-slip extension of the Gawler Craton Coorong Shear Zone in Southern Australia [*Gibson et al.*, 2013]. Additional identified WSB faults and magnetic lineaments, most likely emerging as reactivated Ross Age fractures during Cretaceous extensional tectonics associated with the West Antarctic Rift [*Jordan et al.*, 2013], correlate well with existing sub-basin structures in the WSB including the eastern, western, and central basins identified by Ferraccioli et al. [2009].

Sediment distribution from depth to magnetic basement and basal roughness:

Due to the inherent high variability and source depth errors (on the order of 20-40% [*Kilty*, 1983] for DTB calculations), DTB results were segregated by wavelength based upon 2D Werner deconvolution window size and plotted along profile against

Geosoft's GM-SYS® gravity modeling results. Significant noise was noted particularly with the short wavelength spectrum such that solutions were clustered to reveal areas along the flight profile where DTB results remained less than -500 m. Extremely shallow DTB estimates occurring above the base of the ice sheet were rejected prior to gridding in well-sampled areas, the sparsely sampled areas toward the WSB interior were not culled and therefore may have led to the negative skewness and some erroneous minimum DTB values.

These areas generally correlated with gravity modeling results revealing little to no sediment (Figure 4.9), were found to be within the error of the base of the ice sheet and were thereby interpreted as ice overlying crystalline basement rocks [*Aitken et al.*, 2014]. Short and medium DTB wavelength solutions were scattered throughout the gravity-modeled subglacial sedimentary basin profiles potentially responding to remnant magnetism inherent in glacial erratics entrained in the sediment column. In the end, the long wavelengths (10-30 km), responding to deeper magnetic sources, proved most suitable in vertical constraint of the sedimentary basin base given the primary magnetic anomaly amplitudes across the WSB; this final deconvolution window size range not only provided the best vertical constraint to gravity basin modeling, but was also consistent with previous aeromagnetic reduction findings for the Northern WSB [*Ferraccioli et al.*, 2009].

While the inherent high variability in long wavelength DTB solutions for the WSB resulted in depths to magnetic basement from 3-13 km below mean sea level (Figure 4.7). Comparison with short and medium wavelength results indicated the potential for subglacial sedimentary basin thicknesses ranging from 0-6 km at a number of 20 km direct-gridded locations, the median long wavelength DTB values for the WSB were -7.2 km with a mean value of -8.1 km. The DTB results were also characterized by a substantial standard deviation (3.6 km) and a negative skewness of -2.1, indicating a probability distribution skewed toward DTB measurements falling below current WGS84 sea level elevations. Extremely shallow DTB estimates occurring above the base of the ice sheet were rejected prior to gridding in well-sampled areas, the sparsely sampled areas toward the WSB interior were not culled and therefore may have led to the negative skewness and some erroneous minimum DTB values.

Subglacial bed surface roughness was quantified by evaluating RMS deviation over correlation length on scales of 1600 m. Results were subsequently gridded at 2 km, using a minimum curvature approach, and plotted (Figure 4.8) with GMT. These sediment mask results revealed significantly smoother surfaces across the interior of the Southern WSB, Adventure Trench, EARS, and central and western basins of the Northern WSB with RMS height deviations falling below 10 m over the respective length scales. RMS deviation over correlation length is not only impacted by changes in RMS deviation, but also by larger autocorrelation lengths associated with smoother and rougher surfaces by smaller lengths [*Shepard et al.*, 2001]. As such, subglacial and subaerial highlands (including Dome C, the Resolution subglacial highlands, and the TAM) resulted in RMS height deviation values exceeding 70 meters at the 1600 meter correlation length scale. The distinct transition between rough and smooth bed surfaces at the subglacial basin edge in the interior WSB provided additional lateral constraint during subsequent sedimentary basin modeling efforts. These smooth bed features remain consistent with the presence of weak, unconsolidated sediments across interior portions of the WSB [*Alley et al.*, 1987].

Modeling and interpretation of sedimentary basins

Prior to actively modeling potential sediment thicknesses across the WSB, a combination of constraints from DTB, basal roughness and isostatic residual anomalies suggested that particularly the Southern WSB may contain substantially more sediment than previously suggested by Studinger et al [2004]. Subsequent 2D forward gravity modeling (Figure 4.10) revealed that much of the interior WSB, in areas characterized by smooth bed surfaces in radar sediment mask analyses (Figure 4.8), exhibited a minimum of 1000 m of overlying subglacial sediment thickness. Three distinct sub-basins, the central Southern WSB, and the central and western basins in the Northern WSB, that were characterized by RMS deviation versus correlation length estimates of less than 10 meters at the 1600 meter scale all contained sedimentary basin isopach results in excess of 3 km. The central Southern WSB contained an average sediment isopach value of 1,623 m +/- 254 m with gravitational response across flight transects resulting in sediment thicknesses in excess of 6 km in certain locations (Figure 4.9). The Northern WSB, by contrast, revealed lower average sediment isopach values of 1,144 m +/- 179 m. With gravitational models along flight lines crossing the eastern, central and western basins of the Northern WSB, illustrating subglacial sediment thicknesses in excess of 2.5 km, 4 km, and 3.5 km, respectively. These isopachs can be compared to conjugate margin coastal plain and deltaic-marine sedimentation in the Otway Basin of South Australia containing some 5 km of post Late Cretaceous Sherbrook Group deposition [*Krassay et al.*, 2004]. Estimated sediment volumes based on the calculated WSB isopachs (with 20% porosity) would be on the order of 128,094 +/- 52,399 km^3 for the central Southern WSB, and 7,188 +/- 2,940 km^3, 30,596 +/- 12,515 km^3 and 21,524 +/- 8,805 for the eastern, central and western basins in the Northern WSB, respectively. This predominance of thicker sedimentary sequences coincident with preglacial drainage and tectonic structures in the Northern and Southern WSB is consistent with the recent geomorphologic findings of Jamieson et al. [2014] who suggested that the long term impact of such selective linear erosion along regional hydraulic and ice flow and erosion pathways may give rise to further ice sheet instability in areas below present day sea level.

While the central Southern WSB sub-basin is bounded by the TAM and the Resolution Subglacial Highlands, the Northern WSB sub-basins is in direct association with the Dome C and the Belgica Subglacial Highlands,. The time required to infill the respective sub-basins with the calculated sediment volumes was estimated (Table 4.3) to gain an improved understanding of sediment provenance, composition, and the relative quantity of preglacial basin infill.

Process	***Sedimentation Rate***	***Central Southern WSB***	***Eastern Basin Northern WSB***	***Central Basin Northern WSB***	***Western Basin Northern WSB***
Fluvial	*0.075 cm/yr*	*8 M yrs*	*3.3 M yrs*	*5.3 M yrs*	*4.6 M yrs*
Temperate/polythermal Glaciation	*10 cm/yr*	*60 k yrs*	*25 k yrs*	*40 k yrs*	*35 k yrs*

Table 4.3: Estimated Basin Deposition Elapsed Time (assuming all sediment deposited prior to current polar EAIS), fluvial rates based on historic Gulf of Mexico rates [*Galloway and Williams*, 1991], temperate/polythermal rates are based on current temperate/polythermal valley glaciers of SE Alaska [*Hallet et al.*, 1996].

Assumptions were made that 1) if the basins were overlain by the EAIS, erosion processes, not depositional would dominate [*Siegert et al.*, 2004], and 2) with EAIS advance to basin margins, temperate/polythermal systems would dominate, not present-day polar. Based upon these results, it is evident that the temperate/polythermal systems are orders of magnitude more efficient at basin infill, such that the vast majority of subglacial sediment in the central Southern WSB, and eastern, central, and western sub-basins in the Northern WSB are the result of these temperate/polythermal depositional processes. These high sediment fluxes and associated productivity spikes during interglacial (temperate/polythermal) periods and were noted in the post-middle Eocene in continental shelf sequences immediately offshore west Wilkes Land and the Totten Glacier catchment [*Close et al.*, 2007] and again during the early to middle Pliocene warming period [*Escutia et al.*, 2009]. During the onset of temperate/polythermal processes in the early Miocene, the sedimentation rate estimated from Ocean Drilling Program (ODP) cores in Prydz Bay was as much as seven times higher than the more conservative Hallet et al. [1996] rate used in Table 3 here [*Cooper, A.K. and O'Brien*, 2004].

4.6 CONCLUSIONS

Here I have presented the first comprehensive subglacial sediment isopachs for the WSB region derived from airborne gravity measurements and corroborated against other geophysical datasets that are known sedimentary basin indicators. The central Southern WSB contained an average sediment isopach value of 1,623 m +/- 254 m with sediment thicknesses in excess of 6 km in certain locations, while the Northern WSB revealed average sediment isopach values of 1,144 m +/- 179 m and subglacial sediment thicknesses in excess of 2.5 km several sub-basin locations. The substantial increase in subglacial sedimentary basin thickness to the south supports a hypothesis of relative ice sheet stability across the WSB interior since the mid-Miocene [*Jamieson et al.*, 2010] with more frequent Pliocene to Pleistocene ice sheet retreat/advance cycles impacting the Northern WSB [*Miller et al.*, 2012; *Cook et al.*, 2013] across century to thousand year time scales [*Pollard et al.*, 2015]. The presence of thicker subglacial sedimentary basins in the Southern WSB, proximal to both TAM and EARS highlands, may be the result of a combination of temperate/polythermal alpine regimes during the early Miocene/late Oligocene as suggested by Young et al [2011] for the adjacent Aurora Subglacial Basin (ASB). This combined with the fact that polar ice currently characterizing the Wilkes Land region is predominantly considered an erosional as opposed to depositional environment, much of the basal sediment detected within the WSB interior would have been deposited during a preglacial fluvial or marine facies [*Siegert et al.*, 2004].

More recent studies by Schroeder et al. [2013], conducted in the Thwaites Glacier catchment of West Antarctica, suggest that basal ice conditions in the interior portions of the WSB may be controlled by distributed/dendritic subglacial hydraulic networks in equilibrium with overlying ice that reduce basal drag, rather than more channelized subglacial hydraulic canal networks. If plausible, increased basal drag and associated erosion and scouring would be more prevalent in the Northern vs the Southern WSB supporting our findings that the Northern WSB is dominated by thinner subglacial sedimentary deposits with significant accumulations only in restricted, channelized basins correlating to regional faults. With Northern WSB bed elevations averaging an excess of 500 meters below sea level and deeper channelized subglacial basins leading outlet glacier catchments, the susceptibility of this region to eustatic forcing including the likelihood of significant sediment deformation fueling basal EAIS dynamics in the region [*Alley and Blankenship*, 1987] can be substantiated. More recent WSB paleoclimate models and ice volume assessments by Cook et al. [2013], Mengel and Levermann [2014], and Pollard et al. [2015] support these WSB sedimentary basin findings to suggest a more dynamic EAIS during the Pliocene for significant portions of the Northern WSB and George V Coast with potential significant impacts for the Cook, Ninnis and Mertz glacier catchments. In addition to broad implications for EAIS boundary conditions used in determining rate of retreat for Wilkes Land climate models, the extent, thickness and character of the WSB subglacial strata may also contain some of the best preserved paleoclimatic data associated with the last EAIS retreat-advance over this region and thus be a future target for subglacial access drilling once the technology matures.

Chapter 5: Sequence Stratigraphy and Sediment Distribution Analysis of the Sabrina Coast Continental Shelf, East Antarctica

5.1 ABSTRACT

The Totten Glacier catchment in Wilkes Land, East Antarctic drain approximately 1/8 of all the East Antarctic Ice Sheet and has been shown to be losing mass with the unstable dynamic of landward-sloping beds generating potential run away retreat. Despite this fact, the Sabrina Coast continental shelf (SCCS) in front of Totten Glacier had never been surveyed until the recent RVIB *Nathaniel B. Palmer* cruise 14-02 (NBP14-02) due to consistent, annual sea ice conditions at the continental margin. The premier high-resolution multichannel seismic (MCS), swath multibeam bathymetry, and targeted marine geologic sampling reveal the most complete sequence stratigraphic record of the Wilkes Land margin ever recorded. Here I quantify preglacial, temperate/polythermal glacial and polar glacial megasequence sediment volumes in the context of basin-scale geomorphology and bedform geometries to provide insight and constraint as to prior dynamic ice cyclicity along this remote East Antarctic coastline. Notwithstanding the incredible glacial seismic sequence detail and bedform geometries illustrated by the MCS and swath multibeam datasets, over 66% of sediment in this area of the SCCS represents preglacial/fluvial facies with estimated age constraints from late Cretaceous through late Eocene. With over 22% of the SCCS sequence represented by preserved Oligocene-early Miocene temperate/polythermal glacial sediments, the temperate/polythermal glacial facies appears to have been significantly impacted by remobilization of temperate/polythermal sedimentary deposits during subsequent Plio-

Pleistocene polar ice sheet dynamics across the Totten Glacier catchment. The advance of polar glacial conditions at the end of the Miocene were marked by a significant decline in sedimentation rates (only ~11% of the shelf sediments) and a regional angular unconformity on the Sabrina Coast continental shelf with a strong MCS impedance contrast resulting from an extensive gravelly sandstone to sandy diamictite. This study highlights the importance of quantitative geologic constraint to subglacial basal ice conditions for the Totten Glacier catchment models and ongoing aerogeophysical investigations of the ASB interior.

5.2 INTRODUCTION

The potential for dynamic EAIS response to millennial scale climate oscillations has been a matter of much scientific debate. Geomorphologic and glaciologic evidence suggests the EAIS is largely static and impervious to the climatic forcing across shorter time scales [*Thomas*, 1979; *Alley and Whillans*, 1984], while biostratigraphers citing microfossil evidence in the Sirius Formation at Tillite Spur point to deglaciation of the EAIS including inland seas in the Pliocene [*Webb et al.*, 1984; *Harwood*, 1986; *Barrett*, 2013]. By comparison the West Antarctic Ice Sheet (WAIS) that has long been known to have submarine bed elevations and interior dipping bed slopes facilitating millennial-scale instability [*Pollard and DeConto*, 2009]. Through more recent aerogeophysical efforts tasked with mapping the Wilkes Land interior basins, including the Wilkes, Aurora, and Astrolabe Basins, recent scientific efforts have focused on modeled EAIS response to climatic, terrestrial and eustatic forcing mechanisms. Unfortunately, to date, high quality marine geophysical data on the narrow East Antarctic continental shelf that might show evidence of glacial advance-retreat dynamics has proved elusive. Extensive sea ice shielding much of the Wilkes Land continental shelf throughout the year make for challenging marine conditions even for the best equipped, ice-hardened seismic vessels (Figure 5.1). Here I present the first ever high resolution MCS collected along the Sabrina Coast continental shelf (SCCS) proximal to Totten Glacier and the Moscow University Ice Shelf (MUIS). These premier MCS data details preglacial, temperate/polythermal and polar glacial megasequence-scale stratigraphy and multiple glacial advance retreat cycles indicating a more dynamic ASB EAIS across epoch and perhaps even millennia time scales than previously hypothesized.

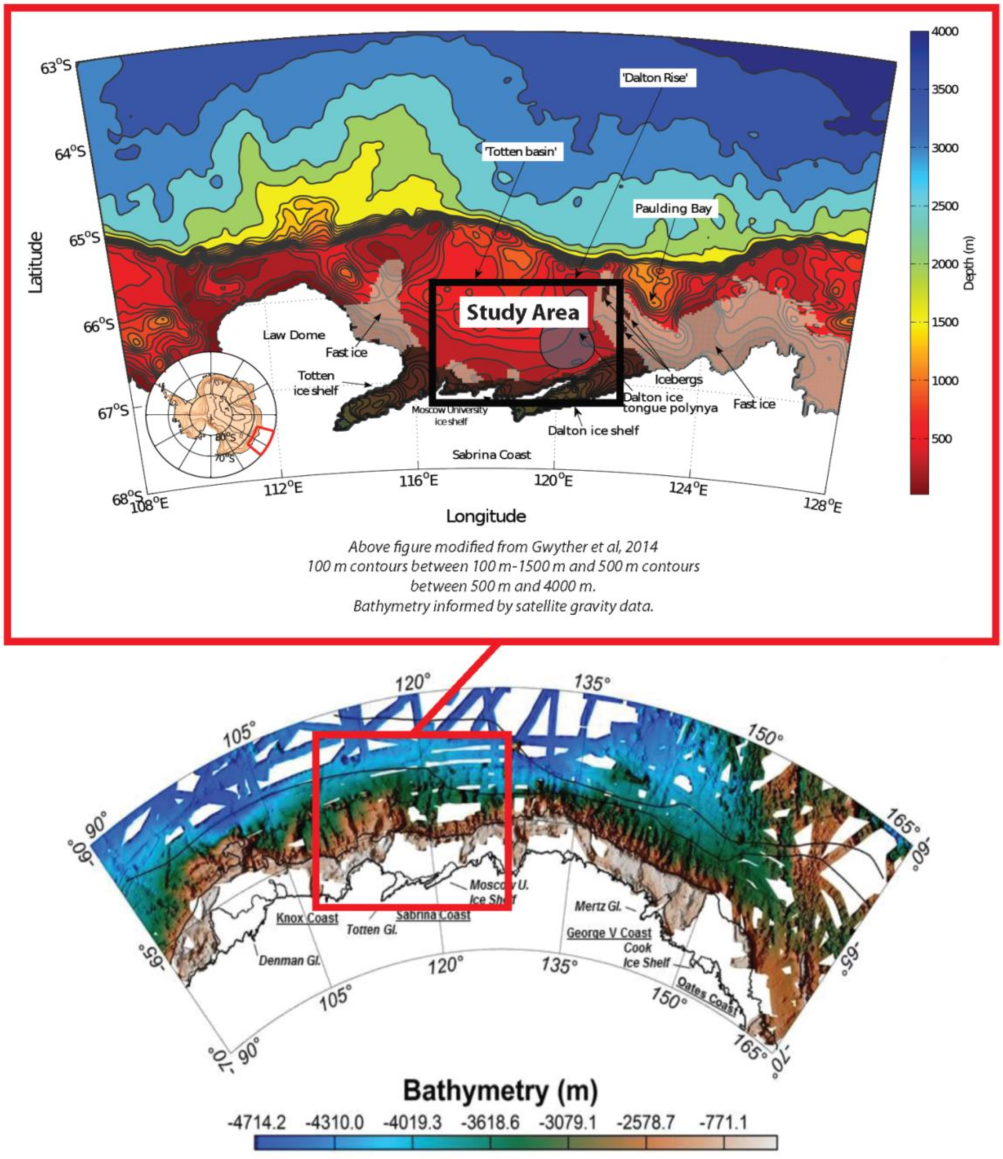

Above figure modified from Gwyther et al, 2014
100 m contours between 100 m-1500 m and 500 m contours between 500 m and 4000 m.
Bathymetry informed by satellite gravity data.

Gridded historical ship track bathymetric data. Coast names underlined. Major glaciers italicized.

Figure 5.1: RVIB *Nathaniel B. Palmer* cruise 1402 study area on the Sabrina Coast continental shelf. Modeled bathymetry data based on satellite gravity (above) from [*Gwyther et al.,* 2014]. Historical, regional gridded bathymetric ship track data (below) from Lamont Doherty Earth Observatory (LDEO) database.

Due to the near total ice cover of the Wilkes Land interior, the marine sedimentary record on the SCCS provides some of the most complete and unreworked geologic sections of the late Mesozoic to Cenozoic morphologic evolution of the ASB region and associated Totten Glacier catchment. Given recent evidence of accelerating mass loss of Totten Glacier [*Chen et al.,* 2009; *Pritchard et al.,* 2012], geologic/geophysical evidence of the climatic transition from fluvial to temperate/polythermal glacial and then to polar glacial regimes remains paramount. Unfortunately, historical marine geophysical records from the East Antarctic continental margin did not include shelf data due to sea ice constraints, and MCS data from the slope and rise have proven inconclusive in delineating this climate transition due in part to lower MCS resolution resulting from requisite increases in seismic source energy required at significantly deeper bathymetric depth, and significant sedimentary reworking mechanics complicating sequence stratigraphic analysis.

In this paper, I present an interpretation MCS megasequence stratigraphy and internal features shedding light on the multitude of dynamic pre and post glacial processes impacting the morphology of the SCCS and the ASB interior across epoch to millennial time scales. Sediment volumes, areas, and depositional controls are introduced to provide new quantitative constraints as to the evolutionary history and dynamics of this area of the Wilkes Land margin. Through the use of marine MCS, gravity, and multibeam bathymetry data, I present evidence for large fluvial-deltaic deposition, temperate/polythermal subglacial hydraulics, and a regional angular unconformity marking the onset of polar glacial conditions. Such quantitative and interpretive sequence stratigraphic estimates are introduced here in the context of prior regional Totten Glacier catchment associated basin analysis surveys completed along the proximal

Budd Coast continental margin and in the ASB interior by Close et al. [2007, 2009] and Frederick et al. [in review], respectively.

5.2 REGIONAL SETTING

5.2.1 Morphologic Setting

The ASB and associated SCCS have been dominated since at least the late Miocene by polar glacial conditions significantly different from more recognized temperate/polythermal glacial conditions (e.g. modern day Alaska and Scandanavia). The evolution of fluvial to temperate/polythermal to polar denudation processes over tens of millions of years, including the associated oscillatory ice dynamics across this margin across epoch to millennial time scales, and the establishment of a permanent EAIS has had profound geomorphologic impact along this section of the Wilkes Land from the interior ASB out to the continental margin. The latest Bedmap2 gridded subglacial and submarine topography compilation [*Fretwell et al.*, 2013] for the region (Figure 5.2) depicts the distinct interior ASB and associated fjords first illustrated by Young et al. [2011], as well as the Totten Glacier catchment and potential subglacial hydraulic pathways [*Wright et al.,* 2012] to the SCCS. The present-day SCCS morphology is dominated by the isostatic impact of ice cap loading and recent erosion and deposition features associated with glacial ice advance and retreat cycles extending out to the shelf break.

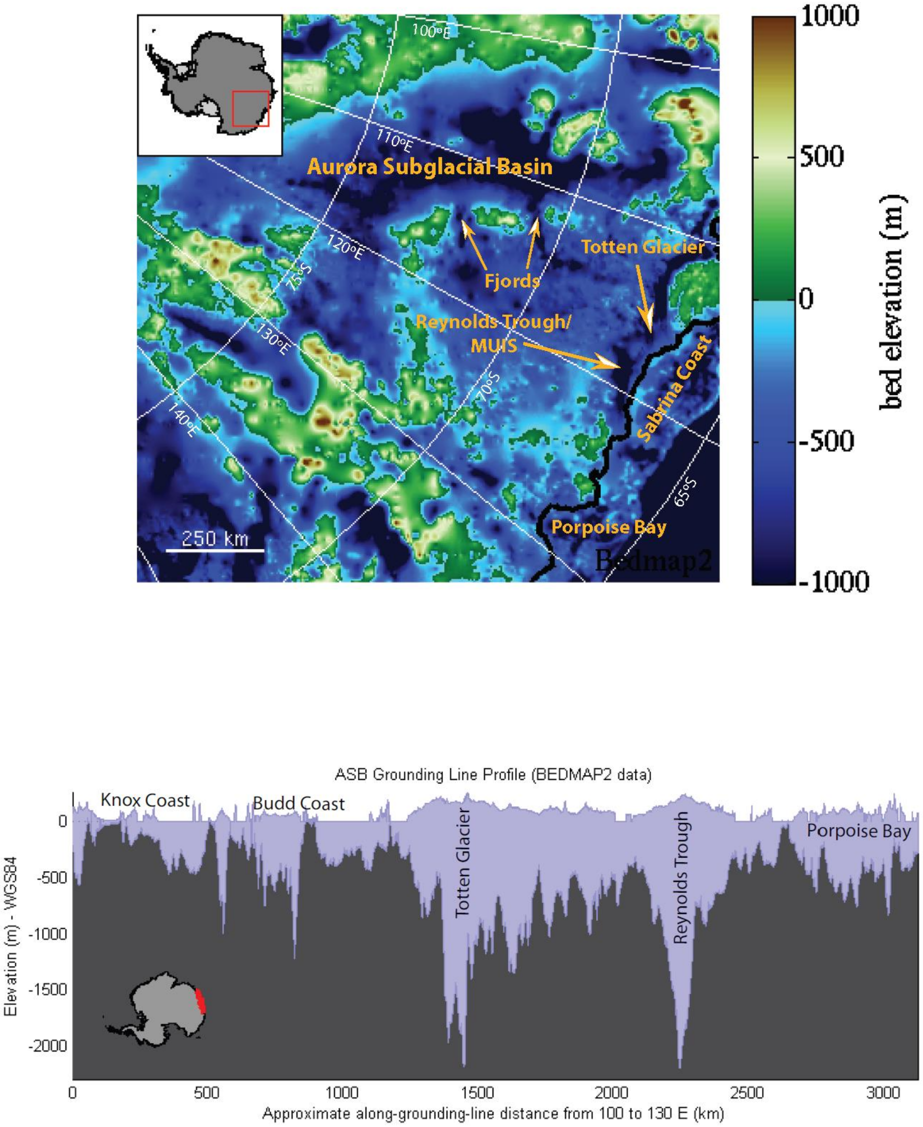

0

Figure 5.2: Bedmap2 contour map depicting the interior ASB relative to the Sabrina Coast continental shelf and shelf break (upper). Lower map indicates 2D bed elevation at the grounding line of the ice sheet margin.

The SCCS varies from 170 km in width in front of the MUIS to only 40 km in front of Law Dome and the vicinity of the Budd Coast Basin [*Close et al.*, 2009]. The shelf bathymetric surface is characterized by interior sloping depths ranging from about 400 m at the shelf break (occurring between 65°S to 65.5°S) to over 1200 m proximal to the ice front. Recent scientific efforts to more accurately quantify the bathymetric surface through aerogeophysical data inversions in this ice-covered region of the continental shelf have raised the possibility of continental shelf channels providing conduits for warm modified circumpolar deep water (MCDW) incursions past the shelf break and Dalton rise to the Totten Glacier grounding line [*Orsi et al.*, 1995; *Gwyther et al.*, 2014; *Greenbaum et al.*, 2015].

5.2.2 Geologic & Climatic History

The geomorphology of this portion of the Wilkes Land continental shelf has been profoundly impacted by dynamic preglacial, interglacial, and glacial climate cycles since the Late Cretaceous breakup of Antarctica and Australia [*Sayers et al.,* 2001]. While initial seafloor spreading was thought to be amagmatic and extremely slow with a half rate of approximately 5 mm/yr along a NW-SE azimuth [*Veevers,* 2012; *Tikku & Cande*, 1999; *Colwell et al.,* 2006], subsequent spreading rate changes by the middle Eocene were estimated to progressively increase from 15 mm/yr, to 24 mm/yr from the late Eocene to early Oligocene, and finally to the present day estimates of 34 mm/yr [*Royer and Rollet*, 1997].

Perhaps the most significant global climatic impact occurred with a Paleogene tectonic event and the opening of the Australian-Antarctic seaway about 30 Ma, specifically the detachment of the South Tasman Rise from the margin of East Antarctica, and the opening of the Drake Passage. Both tectonic events were major factors in the development of the ACC that prompted the thermal isolation of East Antarctica [*Kennett et al.*, 1974], and the development of a continental-scale EAIS at the Eocene-Oligocene boundary [*DeConto and Pollard*, 2003]. From the late Eocene to the mid Miocene, Wilkes Land geomorphology was dramatically impacted by multiple glacial advance/retreat cycles brought about by orbital oscillations [*Naish et al.*, 2001; *Young et al.*, 2011]. Hence, the resultant climatic setting since the early Paleogene would have evolved from a cool, temperate preglacial climate, to temperate/temperate/polythermal glacial conditions, to that of present day polar glacial conditions initiated about 13.8 Ma amidst a global climatic cooling trend [*Zachos et al.*, 2001] caused by declining atmospheric carbon dioxide concentrations and an interval of Southern driving increased carbon dioxide sequestration [*Shevenell et al.*, 2004, 2008]. Although it has long been understood that large-scale glaciation has existed on Antarctica since at least the early Oligocene [*Barrett*, 1996], the nature and timing of these nascent ice sheet fluctuations across Wilkes Land has been the subject of considerable debate [*Siegert et al.*, 2008].

Marine geologic and geophysical records can be particularly useful for providing constraint for numerical models, determining geologic facies, sedimentation volumes and rates during associated global climate oscillations impacting Wilkes Land and the SCCS. Overall sediment flux associated with the geomorphologic evolution of the ASB interior could be expected to have fluctuated across longer time scales with large sediment flux associated with initial tectonic rifting in the Cretaceous, followed by more moderate rates through the Paleocene – early Eocene characterized by fluvial-deltaic denudation [*Powell*, 1984], and finally a substantial increase in sediment flux during temperate/polythermal glacial periods of the mid Eocene through the Miocene [*Koppes* *and Montgomery*, 2009]. During polar glacial conditions, lower basal velocities and minimal meltwater activity would be expected to dominate through the Pliocene-Pleistocene epoch with significantly lower overall sedimentation rates compared the earlier Cenozoic [*Domack,* 1988; *Donda et al.,* 2003; *Anderson & Domack,* 1991]. Yet despite this broad understanding of glaciomarine geologic facies and associated ice and fluvial dynamics, little is known about the initiation, growth and development of the EAIS across the ASB, the Totten Glacier-Reynolds Trough catchment, and SCCS. Marine seismic, potential fields and geologic sampling records provide greater precision and constraint for global climate models with respect to the development of the early EAIS, while establishing the first SCCS geologic/geophysical record linking subglacial, interior ASB sedimentary basins with the Budd Coast and Sabrina Coast offshore continental margin deposits [*Close et al.*, 2009].

5.3 DATA

5.3.1 Bathymetry

Multibeam bathymetry data were collected continuously during the NBP14-02 cruise from January 29, 2014 to March 16, 2014 using the shipboard Kongsberg EM-120 multibeam echosounder as part of the Sabrina Coast Marine Record of Cryosphere – Ocean Dynamics project to examine seafloor morphology and bedforms in more detail. The EM-120 has an operating frequency of 12 kHz and 191 beams producing a maximum coverage area per swath of 25 km. The transducer is located along the NBP keel with the receiver array located in the athwart ship direction. Multibeam bathymetry data were processed onboard using CARIS HIPS and SIPS software (http://www.caris.com/products/hips-sips) package and gridded and rendered to 1 km^2 resolution using ESRI ArcGIS® mapping software (http://esri.com/software/arcgis). The gridded multibeam bathymetry data with multi-channel seismic shiptrack lines are displayed in Figure 5.3.

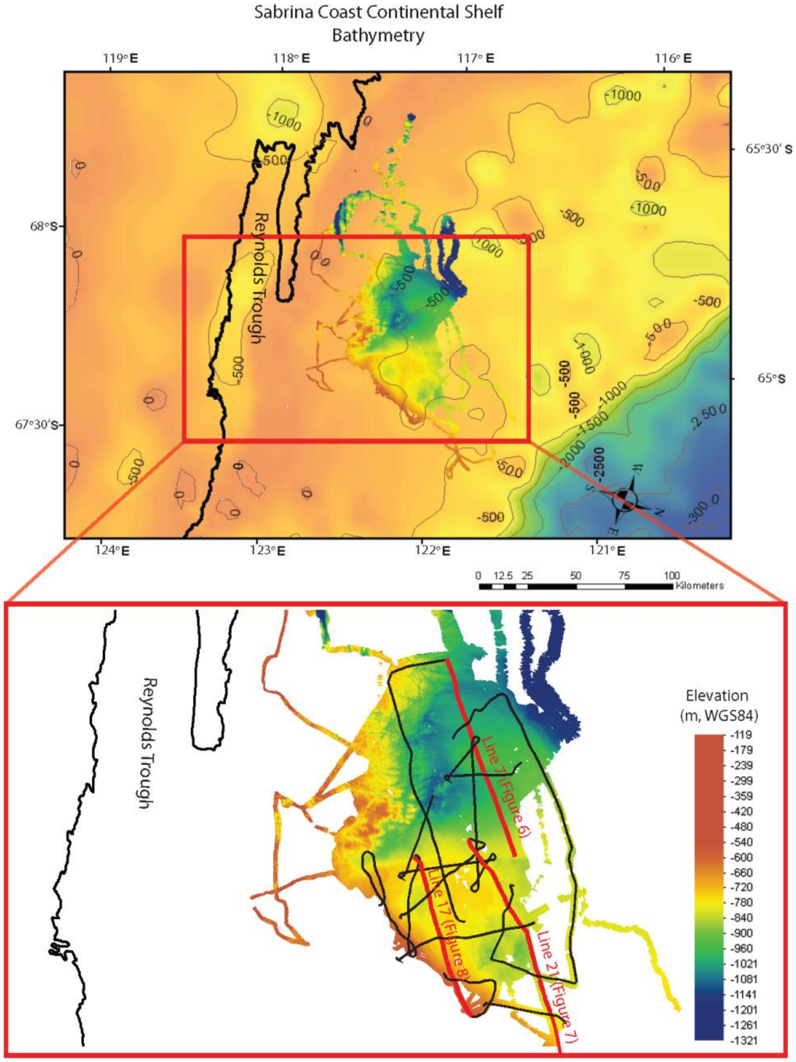

Figure 5.3: Multibeam bathymetry of the Sabrina Coast continental shelf overlain on Bedmap-RTOPO subglacial/submarine topography (upper figure) depicting the improved resolution of bathymetry and identification of a trough trending northwest in front of Totten Glacier. The 500 m contour interval for Bedmap-RTOPO data is shown. Lower figure exhibits bedform character in more detail including scoured bedrock to the west, moraine deposits, and significant sedimentary basin infill to the east associated with the Reynolds Trough. 2D seismic lines shown in figures represented in red.

5.3.2 2D Multichannel Seismic Reflection (MCS)

Taking advantage of minimal sea ice conditions in front of the MUIS due to a consistent seasonal polyna gyre, over 750 km of high-resolution 2D MCS data were collected aboard the NBP between February 4, 2014 and March 7, 2014 using combined components of the University of Texas Institute for Geophysics (UTIG) high resolution hydrophone streamer and the NBP shipboard acquisition systems and seismic source. The seismic source was a dual Sercel G.I. airgun array configured in harmonic mode at 45/45 in^3 with an in-line separation of 2 meters; this array was towed with a hot spare at depths of 2.5-3 m. The in-line center of the source was 29 m from the stern and fired every 5 seconds for a nominal shot spacing of 12.5 m. Source frequency content was estimated at 20-300 Hz with maximum power generated at 100-160 Hz. MCS data were acquired using the UTIG 100 meter gel-filled Teledyne 24-channel streamer with a channel spacing of 3.125 m and 3 hydrophones per channel. Common depth point (CDP) spacing selected was 3.125 m with a nominal fold of 6, a trace spacing of 3.125 m, and an approximate vertical resolution of 3 m. The data sampling rate was 1 ms and the record length was 2.5 s.

Following application of an initial shipboard “brute” stack processing sequence, MCS data were corrected for geometric acquisition offset using a Matlab (http://www.mathworks.com/) script to account for a) the offset of the G.I. guns with respect to the ship’s center of gravity by projecting shotpoint locations into Universal Transverse Mercator (UTM) 50S coordinates, and b) the ship’s crab angle. The MCS data were then processed to poststack time migration using Paradigm’s FOCUS software (http://www.pdgm.com/solutions/seismic-processing-and-imaging/seismic-processing) using the following processing workflow: SEG-Y convert, polarity reversal, bandpass filter, geometry definition, F/K filter, spherical divergence correction, trace balance, noise reduction, CDP sort, velocity analysis, NMO correction, offset mute, seafloor mute, CDP stack, F/K migration (using 1480 m/s constant velocity). For the majority of the MCS lines, the seafloor multiple appeared below the target sequence stratigraphy such that extensive multiple attenuation processing was not required which is fortuitous due to the short streamer length. That the multiple was largely deeper than the imaged section is a consequence of relatively deep SCCS water depths (~750 m), as compared to the worldwide average continental shelf water depth of 150 m [*Pinet*, 2013].

5.3.3 Marine Gravity

Over 5,230 km of dual-instrument marine gravity data were collected continuously during the six-week NBP14-02 cruise using two gravimeter platforms: a) a Bell Aerospace BGM3 on semi-permanent loan to the NBP from the University National Oceanographic Laboratory and serviced by Wood Hole Oceanographic Institute, and b) a Gravimetric Technologies-2 Marine edition (GT-2M) provided by CMG-Operations of Perth, Australia in partnership with the UTIG. The primary marine gravity data results used in this study were collected using the BGM3 marine gravimeter for consistent ties and correlation with prior regional BGM3 aerogravity data collected as part of the ICECAP aerogeophysical program. Two pre- and post-cruise gravity ties were completed before the NBP left port in Hobart, Australia, with a computed instrument drift of 2.4 mGals deemed acceptable. Fundamental corrections for instrument drift, latitude, instrument elevation (relative to sea level) and the Eötvös effect were completed and the resultant marine free-air gravitational response gridded at 1 km^2 using the minimum curvature method (Figure 5.4).

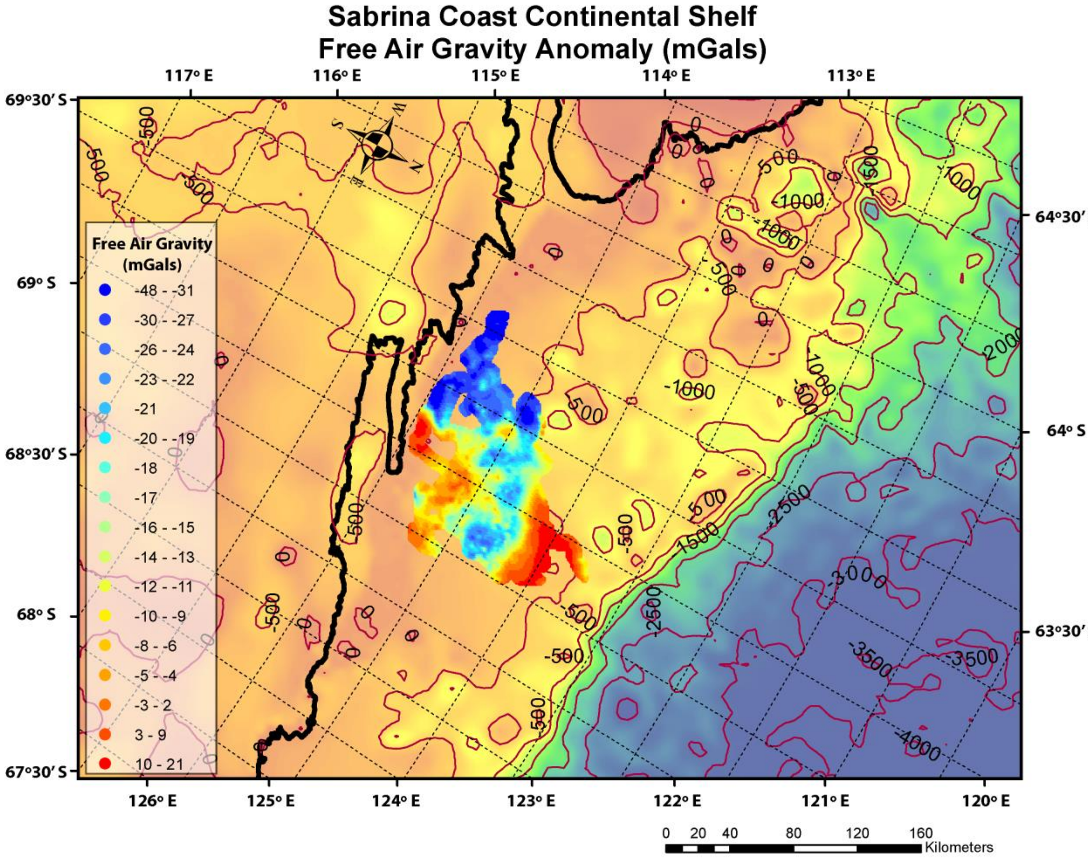

Figure 5.4: Marine free-air gravity data (mGals) of the Sabrina Coast continental shelf direct gridded at 1 km with Bedmap and RTopo-1 compilation of subglacial bed elevation and bathymetry (500 m contours) in the background [*Lythe and Vaughan*, 2001; *Timmerman et al.*, 2010].

Bouguer gravity corrections were completed using coincident multibeam bathymetry data and an assumed constant terrain density of 2.0 g/cc iteratively as a priori data input into Geosoft's GM-SYS® 3D modeling package. The resultant marine

Bouguer anomaly was also gridded at 1 km^2 using the minimum curvature method (Figure 5.5).

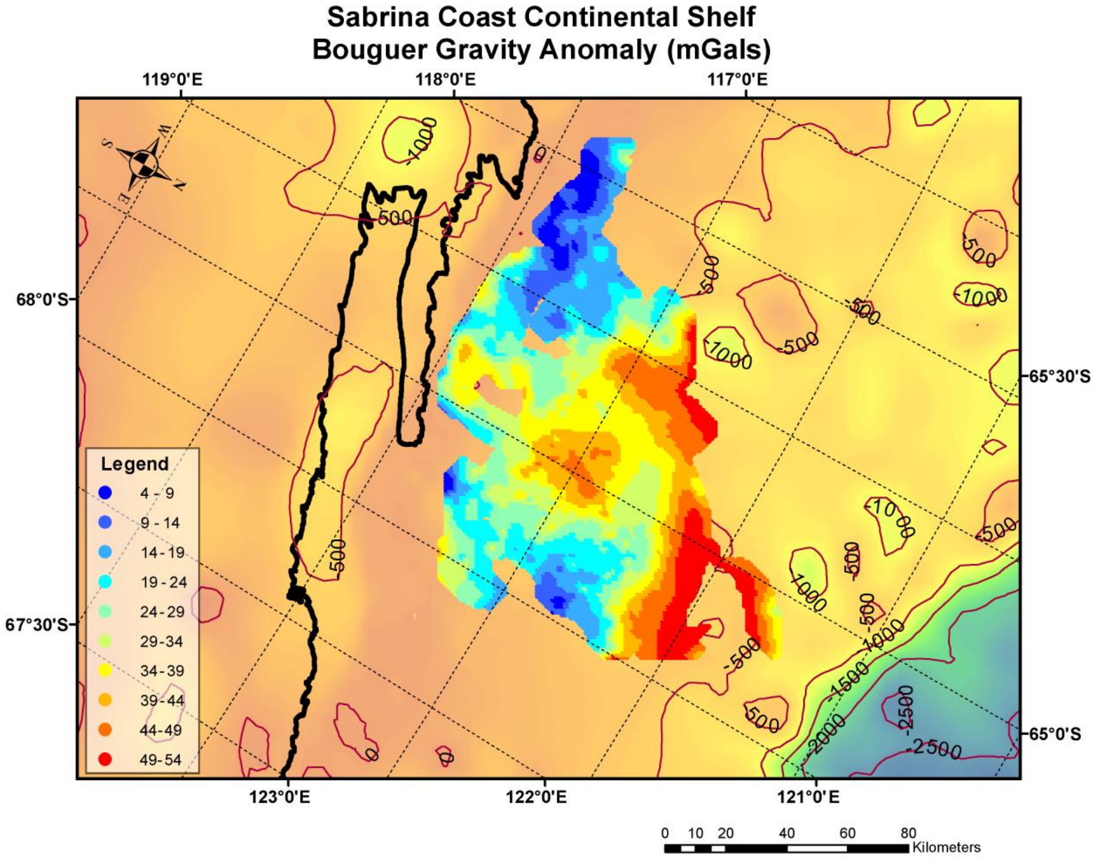

Figure 5.5: Marine Bouguer gravity data (mGals) of the Sabrina Coast continental shelf direct gridded at 1 km with Bedmap and RTopo-1 compilation of subglacial bed elevation and bathymetry (500 m contours) in the background [Lythe and Vaughan, 2001; Timmerman et al., 2010].

5.4 METHODS

Following processing, NBP14-02 MCS data were imported into Halliburton's Landmark OpenWorks (https://www.landmarksoftware.com) interpretation software. The majority of seismic interpretation was completed using the DecisionSpace® Desktop module. Multibeam bathymetry data, gridded and rendered using ESRI ArcGIS® mapping software, were subsequently imported into DecisionSpace® Desktop to facilitate integration with MCS data interpretation.

Unconformable horizons and megasequence boundaries, including bathymetric and basement reflectors, were mapped. Most notable across every seismic line was a regional angular unconformity interpreted as the boundary between temperate/polythermal and polar glacial regimes. A number of additional unconformities were noted both above and below the regional angular unconformity including one horizon that was determined to represent the boundary between preglacial and temperate/polythermal glacial facies. Gridded isopachs, calculated in two-way travel time (TWTT), were generated for the preglacial, temperate/polythermal, and polar SCCS megasequences using DecisionSpace® desktop software. For the preglacial megasequence, the lower basement boundary had to be estimated for many of the MCS lines as the seafloor multiple masked the basement reflector as it dipped steeply northward toward the continental margin boundary. Basement TWTT reflector estimations beyond where imaged on NBP14-02 data were calculated through regional interpolation with basement reflectors from historic seismic data collected along the Sabrina Coast continental margin to estimate basement extend under the NBP14-02 study area.

Marine gravity data, including free-air and Bouguer anomaly corrections and 3D Euler deconvolution DTB methods, were all calculated using Geosoft's Oasis montaj® software suite to assess density variations in sedimentary units on the SCCS as well as confirm basement depth to ultimately provide for greater vertical control for preglacial sediment volume estimates. Horizontal and vertical derivatives of the free-air gravity anomaly were first calculated and gridded at 1 km^2 using a minimum curvature technique. This step was followed by the application of Euler's homogeneous function theorem with the degree of homogeneity expressed as a structural index (SI). Figure 5.6 depicts the results of the 3D Euler deconvolution using marine free-air gravity data input, a window size of 12 x 12 (3,000 m), and a SI = 0.5.

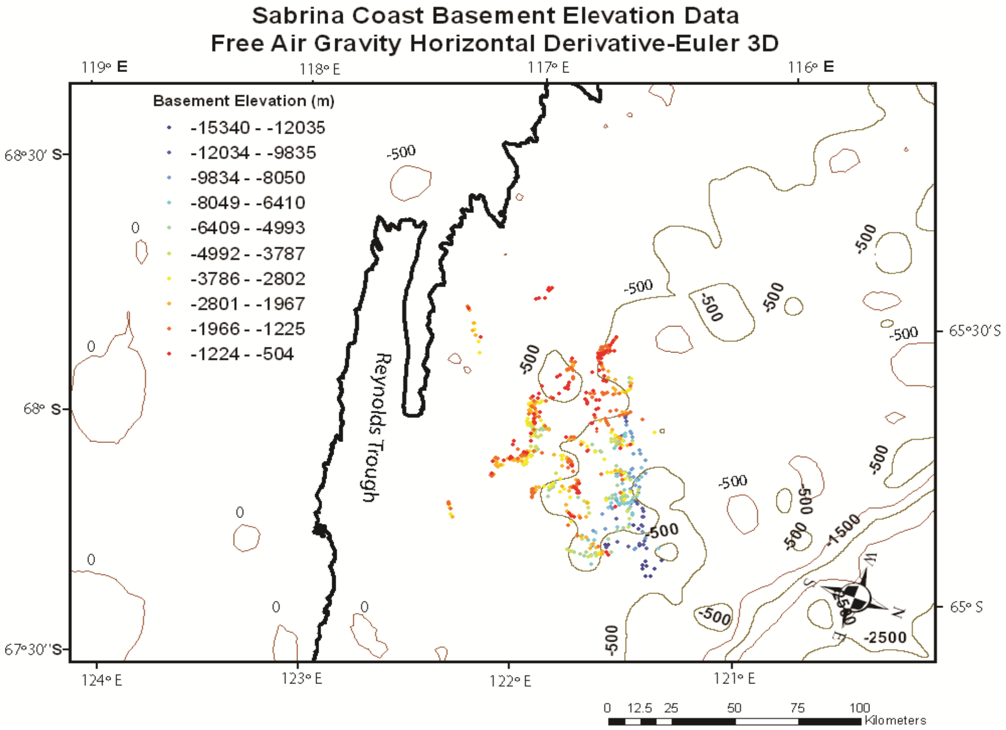

Figure 5.6: 3D Euler deconvolution results derived from marine free-air gravity data.

For each MCS megasequence identified on the SCCS, I geometrically calculated sediment volumes (Vol_{sed}) from the gridded TWTT isopach result of each megasequence using the following algorithm modified from Fernandez et al [2011]:

$$\mathrm{Vol}_{sed} = \Sigma_{ij}\ P_A(D_{ij}\text{-}B_{\ ij}) \qquad (1)$$

where

P_A = pixel area of surface (m^2);

D_{ij} = pixel (i,j) depth relative to WGS84 mean sea level of the seismic horizon (m);

B_{ij} = pixel (i,j) sea floor depth derived from multibeam swath bathymetry survey (m).

Expanding the equation to account for water depth/velocity based on 3D raster surfaces yields:

$$\mathrm{Vol}_{sed} = [P_{A2}V_p^{sed1}\ \Sigma_{ij}\ T_{ij}^{s}] + [P_{A1}V_p^{w}\ \Sigma_{ij}\ T_{ij}^{w}) - P_{A1}(\Sigma_{ij}\ B_{ij})], \qquad (2)$$

where

T_{ij}^{w} = pixel (i,j) one-way travel time from sea level to bathymetric surface (s);

T_{ij}^{s} = pixel (i,j) one way travel time between seismic horizons (s);

V_p^{w} = one-layer equivalent compressional wave velocity (P) of seawater (m/s);

V_p^{sed} = one-layer equivalent compressional wave velocity (P) of seismic megasequence.

Subsequently deeper megasequence units were calculated by amending the above equations to account for increasing compressional wave velocities with depth:

$$\mathrm{Vol}_{sed} = [P_{A3}V_p^{sed2}\ \Sigma_{ij}\ T_{ij}^{s2})] + [P_{A2}V_p^{sed1}\ \Sigma_{ij}\ T_{ij}^{sl} - P_{A2}\ V_p^{sed1}(\Sigma_{ij}\ T_{ij}^{sl})] + [P_{A1}V_p^{w}\ \Sigma_{ij}\ T_{ij}^{w}) - P_{A1}(\Sigma_{ij}\ B_{ij})] \qquad (3)$$

And

$$\mathrm{Vol}_{sed} = [P_A V_p^{sed3} \Sigma_{ij} T_{ij}^{s3}] + [P_{A3} V_p^{sed2} \Sigma_{ij} T_{ij}^{s2}) - P_{A3} V_p^{sed2}(\Sigma_{ij} T_{ij}^{s2})] + [P_{A2} V_p^{sed1} \Sigma_{ij} T_{ij}^{sl} - P_{A2} V_p^{sed1}(\Sigma_{ij} T_{ij}^{sl})] + [P_{A1} V_p^{w} \Sigma_{ij} T_{ij}^{w}) - P_{A1}(\Sigma_{ij} B_{ij})] \qquad (4)$$

Because such quantification methods include Vp (*P wave velocity*) as the sole control parameter, estimated sediment volumes include porosity. This dependence is illustrated in equations (2-4) as sediment volume in a particular pixel unit is derived from travel times obtained from along 2D seismic profiles. The latter portion of the equations represent the ability of the interpolation method to replicate the bathymetry obtained from the multibeam independent of the depth of the horizon identified in seismic section.

Simplified rock-equivalent volumes ($\mathrm{Vol}_{rx)}$ were concurrently calculated by estimating the volume of source rock equating to the specific volume of sediment: $\mathrm{Vol}_{rx} = (\rho_{sed}/\rho_{source})^* \mathrm{Vol}_{sed}$. For ρ_{sed} I established 1800 kg/m^3, 2050 kg/m^3, and 2200 kg/m^3 for the polar, temperate/polythermal and preglacial megasequence sediments, respectively, based on prior sound velocity analysis work by Orsi and Dunn [1991] on glacio-marine sediments in the Barents Sea. While Barents Sea glacio-marine sediments were compacted under 3 km of polar ice similar to SCCS deposits [*Lambeck*, 1996], Orsi and Dunn [1991] collected all samples from the upper 10 cm of cores. Hence, for the preglacial sediment deposits on the shelf, a more conservative 2200 kg/m^3 was projected given estimated effective sub-ice pressures on the order of 70-90 MPa with 15-18% porosity [*Bahr et al.,* 2001; *Zoback,* 2010]. This density estimate was of similar magnitude to prior modeled subglacial sediment densities in the Wilkes Subglacial Basin [*Ferraccioli et al.,* 2001], and initial field testing of marine jumbo piston core (JPC) samples of outcropped preglacial tills. The density of the parent rock in this case was assumed to be 2670 kg/m^3 which is a typical value for metasedimentary and igneous rock and mimicked the value used in regional aerogeophysical potential field modeling for the ASB [*Frederick et al,* in press]. Porosity uncertainties were difficult to quantify, but were estimated at +\- 10% based upon geologic results from the shallow NBP1402 geologic piston core results and deeper porosity measurements obtained during IODP Expedition 318 at the Wilkes Land Antarctic margin [*Escutia et al.,* 2011].

To estimate the areal error associated with our sediment volumes estimates, I quantified variation in sediment volume estimates given uncertainty in different interpolation methods used to generate grids including spline, nearest neighbor, and cubic (Table 5.1). Megasequence area (km^2) was quantified across all MCS lines using seismic sequence stratigraphic methods, reflector character, and geologic constraints. Ultimately, spline (tension) interpolation methods were used to create isopach maps from sediment volumes because the method was shown to best mimic bathymetry without exaggerated interpolation artifacts in areas of low 2D MCS coverage resulting in more accurate volume estimates. Input parameter uncertainty was constrained by a priori information as to the respective interval of likely values.

Vertical thickness uncertainties, including MCS errors of +\- 1 vertical MCS resolution and manual MCS reflector picking or vertical velocity errors (+\- 25 ms in TWTT), were also estimated to assess potential associated sediment volume estimate errors. Vertical uncertainties can introduce substantial vertical thickness and hence volume estimate errors varying from 33.5% in the thin polar megasequence drape to 5.6% for the thicker, but less expansive temperate-polythermal megasequence (Table

5.1). Fortunately, the more substantial vertical velocity picking errors were minimized through a combination of high-resolution acquisition and detailed processing of MCS datasets with no need for water-bottom multiple suppression.

Horizontal components of volume estimate uncertainty can also arise from different interpolation methods used to generate grids, including spline, nearest neighbor, and cubic interpolation. Standard deviation of sediment volumes as a result of horizontal error components ranged from 19.9% in the thin, expansive polar megasequence to 3.5% for the less extensive temperate-polythermal megasequence (Table 5.1).

Facies	Vp (m/s)	Average Thickness (TWTT)	Area (km^2)	Sediment Volume (km^3)	Horizontal component of Error (km^3)	Vertical component of Error (km^3)
Polar	1600	63.2	5,579	278.6	55.5	93.3
Temperate-polythermal	1700	240.5	2,751	570.6	20.1	31.8
Preglacial	1800	418.1	4,408	1,658	136.9	252.9

Table 5.1: Estimated sediment volumes for megasequences on the Sabrina Coast Continental Shelf.

5.5 OBSERVATIONS AND INTERPRETATION

Sequence stratigraphic analysis of SCCS has revealed three predominant megasequences each associated with a preglacial, temperate/polythermal glacial, and polar glacial environment of sedimentary deposition, respectively. The lowermost megasequence contains evidence of Eocene age fluvial, and potential glacio-fluvial sedimentation. The second megasequence indicates the advance of Oligocene-Miocene temperate/polythermal glacial conditions with substantial evidence of meltwater and development of subglacial tunnel valley systems. The last megasequence to be deposited represented the advance of Miocene polar glacial conditions overlying a prominent regional angular unconformity. Montelli et al. (in preparation) also provides a detailed analysis of the timing of these events and a sequence stratigraphic comparison with the paleo-glaciology of the Bering Trough system in Alaska.

In certain areas on the SCCS, the glacial sequence record is notably incomplete as evidenced by the scoured swath multibeam bathymetry results and exposed bedrock in many areas (Figure 5.3). Late Paleogene-early Neogene polar glacial advance-retreat cycles scoured the shelf free of sediment in the mid-shelf, creating an embayment leading to a wide trough trending to the northwest in front of Totten Glacier. Deeply incised, subparallel channels and ridges appear across the western portion of the study area, potentially representing subglacial groundwater conduits during glacial episodes and the northern streaming advance of ice in this region as it extended out toward the shelf margin. In the central and eastern sector of the study area, sedimentary bedforms reveal a complex series of grounding zone wedges, recessional moraine banks, dune forms, megawaves, and slide-block terrains each indicating a complex and dynamic glacial and deglacial history [*Domack et al* (in preparation) and *Fernandez et al* (in preparation)]. Closer inspection of data collected from the hull-mounted 3.5 kHz sub-bottom profiler revealed that the seafloor was in fact generally covered with an approximately 3 m uniform drape of glacial marine silty clay, as revealed by kasten core sampling, representing the final deglaciation across the SCCS [*Domack et al*, in preparation].

Marine free air gravity measurements indicated some correlation with bathymetry as might be expected in the inner shelf; this correlation was especially apparent where the bathymetric surface had been scoured to bedrock in the south and western portions of the study area. To the east, a strong anticorrelation developed with a negative free air gravity anomaly corresponding to the thick accumulation of preglacial and glacial sediment deposition in front of Reynolds Trough. Correspondingly, the Bouguer low anomaly response in the east is also indicative of lower density sediments as identified in the MCS data. This low free air gravity anomaly extends to the west with the associated polar glacial moraine deposition. A distinct Bouguer high centered at 120°E indicates a potential change in bedrock character beneath the sediments, either resulting from a significant change in topographic or density character warranting additional longer wavelength MCS or well data constraint in this area. Another notable free air gravity feature is the strong positive gravity anomaly to the north, characteristic of the top of the continental slope, as crust is substantially thinning and water depths begin to increase substantially at the Antarctic continental margin. A multitude of smaller free air anomalies are apparent in the study area particularly in the region of sedimentary deposition between latitude 66°S and 66.5°S, either resulting from inhomogeneities in the basement or particular bedforms. Unfortunately, without more comprehensive MCS basement surface resolution, the exact cause of these smaller free air gravity anomalies is difficult to determine at this time.

Assessing the current bathymetric surface in seismic section, I observe asymmetric grounding zone wedges identifying the staged successive retreat of the ice margin beneath which lies a regional angular unconformable surface (Figure 5.7). This regional angular unconformity extends across every NBP14-02 MCS section and is believed to represent the regional advance of the EAIS to the shelf edge, coincident with the formation of polar glaciation in the ASB. JPC sampling at an outcropped location of this regional angular unconformity identified the substantial acoustic impedance contrast at the sampling location as a stratified diatomite and gravel-rich diatom-bearing sandstone with a sharp transition to a sandy diamictite [*Gulick et al,* in preparation].

Initial review of the diatom fauna inherent to this lithology identifies the facies as late Miocene in age [*Gulick et al,* in preparation]. I hypothesize that this distinct regional angular unconformity on the SCCS may be coincident with the early Pliocene unconformity WL-U8, identified in IODP 318 coring operations off the Wilkes Land margin, that demarcated the transition to a permanent EAIS [*Escutia et al.*, 2005, 2011].

Within the polar megasequence lie multiple unconformities, represented by distinct, isolated horizons, each erosional boundary representing a successive glacial advance across a prior depositional retreat moraine. These polar glacial stratigraphic sequences symbolize late Miocene-Pleistocene glacial advance-retreat cycles across the shelf including the last glacial maximum (LGM) and the most recent deglacial episodes.

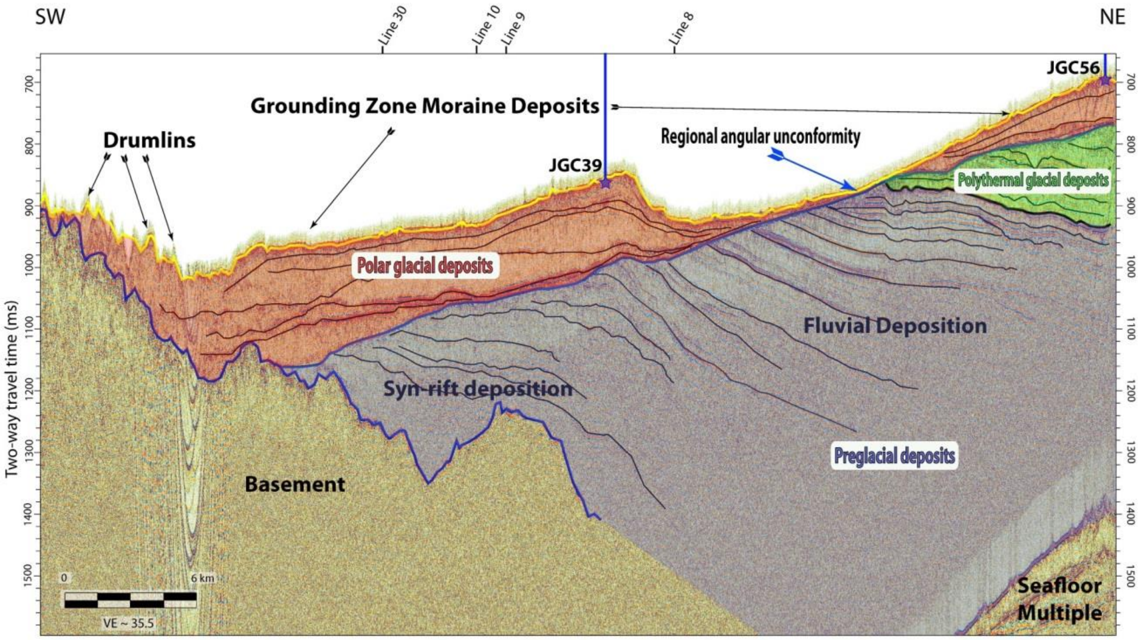

Figure 5.7: Seismic reflection Line 7 exhibiting three primary megasequences. Exposed bedrock, drumlins, moraine deposits, regional angular unconformity, and jumbo gravity core (JGC) sampling locations also shown.

In the eastern portion of the study area, distinct temperate/polythermal subglacial tunnel valley features are readily identifiable in seismic section with broad, deep seismic channel facies containing relatively unstratified, hummocky character with overlying stratified deposits (Figure 5.8). Subglacial tunnel valley complexes are indicative of temperate/polythermal glacial conditions, commonly associated with significant groundwater flux and/or catastrophic subglacial water release through subglacial till deposits [*Huuse & Lykke-Andersen,* 2000]. Current hypotheses suggest that the valley formation stems from subglacial channels during glacial advance that are subsequently infilled in a multistage process during glacial retreat. Several of the more prominent channel geometries identified in the Sabrina Coast MCS section range from 510 m to 3.2 km in width and 52 – 74 m in depth, consistent with subglacial tunnel valley complexes mapped globally from the Ordovician to the Quaternary [*Huuse & Lykke-Andersen,* 2000; *Le Heron,* 2009].

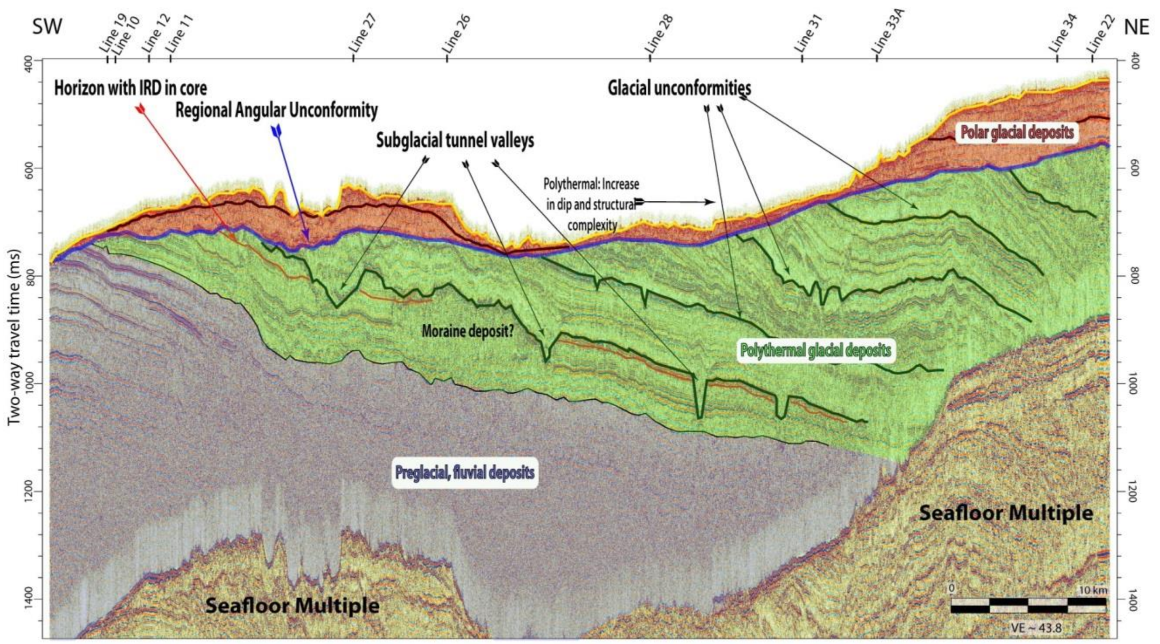

Figure 5.8: Seismic reflection Line 21 exhibiting regional angular unconformity, subglacial tunnel valleys, all three megasequences.

Upsection within the temperate/polythermal megasequence, the high amplitude reflectors increase in dip with less evidence of subglacial tunnel valleys. I hypothesize that the progressively younger northern dipping strata likely experienced a combination isostatic adjustment associated with glacial unloading during ice sheet retreat, given the lack of tunnel valley development, and changes in sediment supply and climate associated with the mid-Miocene climatic optimum. Near the base of the temperate/polythermal megasequence in MCS Line 21, and immediately below a substantial tunnel valley reflector, a target horizon that outcropped near the bathymetric surface in MCS Line 17 (Figure 5.9) was sampled using JPC methods (JPC-54) to reveal angular crystalline clasts in a fine grained, well sorted sandy silt.

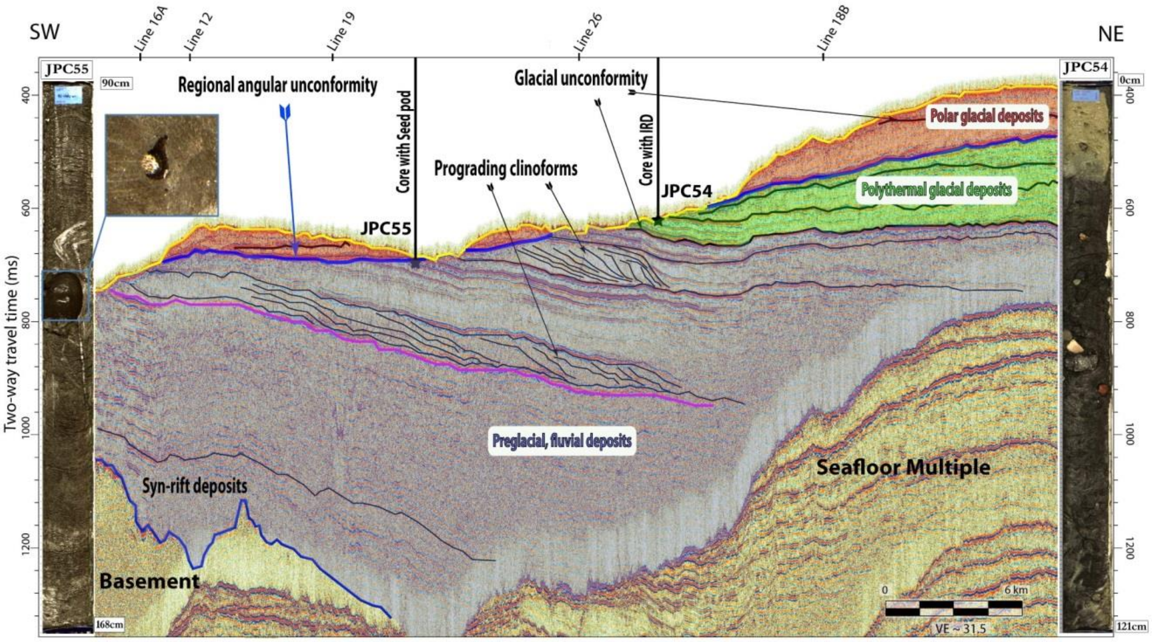

Figure 5.9: Seismic reflection Line 17 with seismic line location inset map - exhibiting moraine deposits, clinoforms, and regional angular unconformity.

These angular clasts represent initial evidence of IRD on the SCCS marking the stratigraphic transition from fluvial or ephemeral proglacial facies to a more permanent temperate/polythermal glacial facies similar to present-day SE Alaska [*Gulick et al.*, in preparation]. Immediately below the IRD marker horizon in MCS Line 17 lie two distinct clinoforms with the characteristic prograding, strata representing a deltaic depositional environment. An additional JPC sample was collected (JPC-55) from outcropping strata in between the 2 clinoforms (Figure 5.8) to reveal similar, but slightly less well sorted and coarser grained lithology than JPC-54 indicating a slightly higher energy depositional environment closer to the fluvial or tidewater glacial source. JPC-55 did not show any evidence of IRD, but did contain an unusual flowering plant macrofossil preserved in the center of a round calcareous concretion. Pollen data support a middle to late Eocene age for both JPC-54 and JPC-55 [*Gulick et al.,* in preparation]; this unique finding supports a preglacial environment and begins to constrain the upper limit of the preglacial seismic megasequence as perhaps proglacial, but not yet tidewater to temperate glacial facies.

The base of the preglacial megasequence is characterized by syn-rift seismic sequences and constrained by basement in a limited number of MCS sections to the south-southwest. With basement dipping steeply to the north, the pronounced reflection either quickly exceeded the penetration depth of the high resolution MCS, or was masked by the seafloor multiple as bathymetric depths shoaled to the north-northeast (Figures 5.7-5.9). Assessing the Sabrina Coast continental margin structure contours in more detail from the basement up section to the present day bathymetric surface, allows for characterization of continental shelf-margin progradation and sedimentary basin evolution across geologic time (Figure 5.10). Northerly basement dip coincided with a general decrease in free air gravity results (Figure 5.4) away from the Sabrina Coast ice front, and showed an increase associated with the Antarctic continental margin. Initial Bouguer gravity results mimic the Polar-Polythermal structure contour (A) with a low corresponding to significant deposition of sedimentary material comprising the Preglacial and Temperate/Polythermal megasequences in front of Reynolds Trough and in the vicinity of the present-day Dalton Rise.

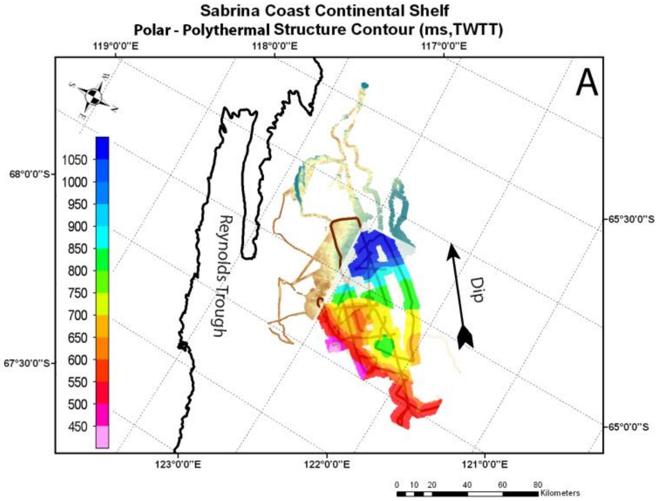
Sabrina Coast Continental Shelf
Polar - Polythermal Structure Contour (ms,TWTT)

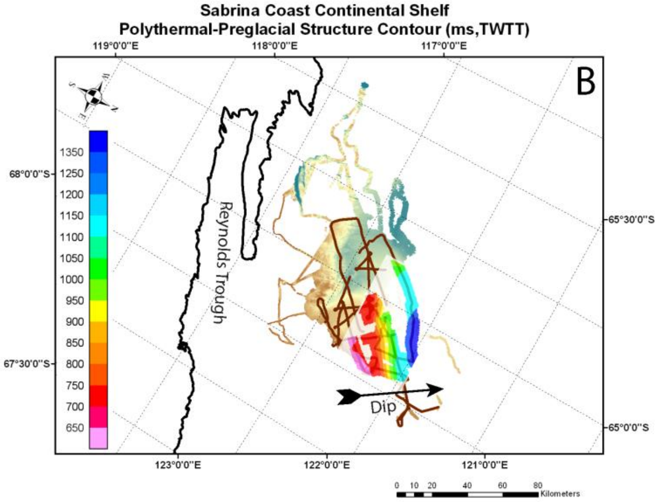
Sabrina Coast Continental Shelf
Polythermal-Preglacial Structure Contour (ms,TWTT)

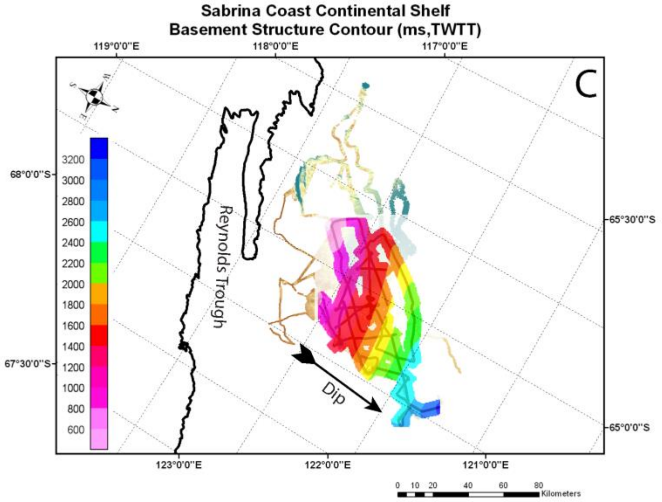
Sabrina Coast Continental Shelf
Basement Structure Contour (ms,TWTT)

Figure 5.10: Structure contour maps for seismic horizons gridded at 500 m two-way travel time (TWTT) in milliseconds (ms) with swath multibeam bathymetry and multi-channel seismic (MCS) track lines shown in the background for context; WGS84-based Polar Stereographic Latitude 71 degrees (PS71) grid (meters). A – Regional unconformable surface at base of interpreted polar glacial deposits (50 ms contour interval), B – Preglacial-Temperate/polythermal glacial unconformable surface (50 ms contour interval), C – MCS basement surface (200 ms contour interval).

Utilizing structure contour maps derived from MCS data for the three main megasequence boundaries, namely the seafloor, the regional angular unconformity at the base of the interpreted polar deposits, and the preglacial-temperate/polythermal boundary (indicated by a high amplitude reflector between the clinoform and the IRD sample), isopach maps were constructed in TWTT (Figure 5.11) consistent with the interpretations made by Montelli et al [in preparation]. The basement structure contour and associated megasequence isopach calculations were derived from a combination of MCS structure and DTB results due to the fact that in many of the MCS lines, the basement reflector either dipped below the 2.5 s vertical resolution of the section or was masked by the seafloor multiple.

Sabrina Coast Continental Shelf
Totten Preglacial Megasequence Isopach (ms)

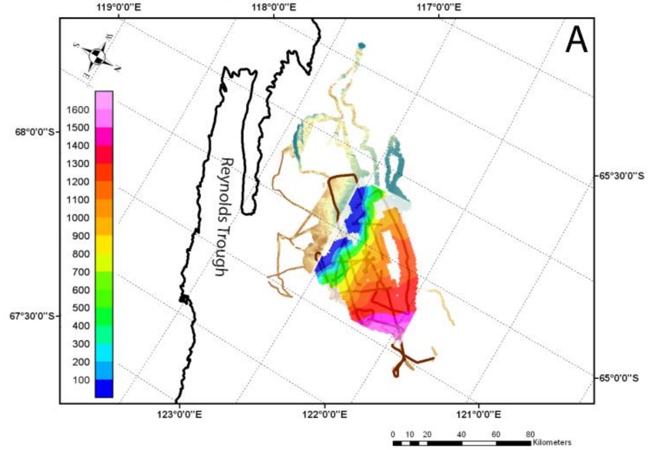

Sabrina Coast Continental Shelf
Totten Polythermal Megasequence Isopach (ms)

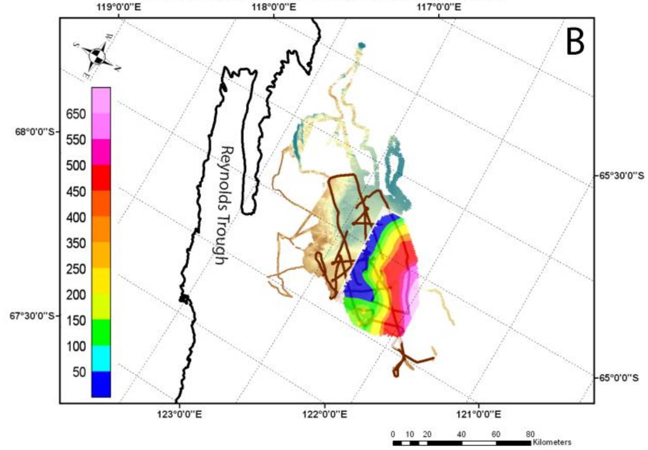

Sabrina Coast Continental Shelf
Totten Polar Megasequence Isopach (ms)

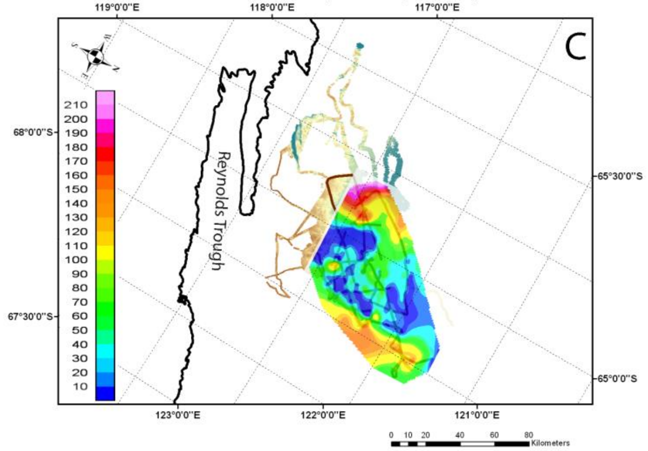

Figure 5.11: Megasequence isopach maps gridded at 1 km two-way travel time (TWTT) in milliseconds (ms) with swath multibeam bathymetry and multi-channel seismic (MCS) track lines shown in the background for context; WGS84-based Polar Stereographic Latitude 71 degrees (PS71) grid (meters). A – Preglacial glacial isopach (100 ms contour interval), B – Temperate/polythermal glacial isopach (50 ms contour interval), C – Polar isopach (10 ms contour interval).

From the steep northward-dipping basement structure indicative of the Cretaceous rifting of this passive margin with Australia; the basin accommodation space filled in through the Paleocene to late Eocene with fluvial sediment influx from Reynolds Trough associated with ASB denudation and tectonics. The resultant preglacial, possibly including a period of pro-glacial, megasequence isopach and associated fluvial-temperate/polythermal structure contour boundary thereby extends out to the north-northeast with an axis trending parallel to Reynolds Trough and present-day Dalton Ice Tongue. I hypothesize that the genesis of the present-day Dalton (bathymetric) Rise and the Dalton Ice Tongue (a mass of grounded icebergs and multiyear sea ice) has been established with a foundation of preglacial Cretaceous to Eocene sedimentation likely in turn reflecting tectonic basement fabric [*Aitken et al.*, 2014]. Hence the western edge of the preglacial sedimentary basin in front of the MUIS (represented by the fluvial to temperate/polythermal unconformity structure contour map), when compared to the eastern edge, depicts a more gradual north-northwesterly dip. Using a combination of MCS-interpreted basement reflectors (where evident in the seismic sequence) and basement elevation obtained from 3D Euler deconvolution methodologies using marine gravity, preglacial sedimentary facies were discovered to thicken toward the SCCS margin and away from the present-day ice front. With significant preglacial sediment loading and lithospheric extension/thinning at the margin, the down-warped SCCS basin averaged an estimated 418.1 ms in TWTT thickness over an expanse of 4,408 km^2. Total preglacial sediment volume, assuming an average megasequence velocity of 1800 m/s, was then calculated to be 1,658 +/- 389 km^3 (Table 5.1).

As alpine and temperate/polythermal glacial conditions developed/expanded near the Eocene-Oligocene boundary, basin sedimentation rates increased along with physical glacial denudation and subglacial outwash, but are hypothesized to have been largely confined to tributaries associated with the Totten and Reynolds Trough catchment. The first ephemeral ice sheets in the ASB and Totten Glacier catchment are thought to have exhibited at least two ice flow regimes between 34-14 Mya causing the overdeepening of existing topographic channels, carving the interior ASB fjords and reversing valley floor slopes [*Young et al.*, 2011].

Temperate/polythermal glacial conditions, associated subglacial meltwater, tunnel valley development, and the advance-retreat cycles of ephemeral ice sheets through the Miocene resulted in the development of a significant sediment isopach exhibiting thicker section to the north (Figure 5.10). The temperate/polythermal isopach averaged an estimated 240.5 ms in TWTT thickness over an expanse of 2,751 km^2. Total temperate/polythermal sediment volume, assuming an average megasequence velocity of 1700 m/s, was then calculated to be 570.6 +/- 51.9 km^3 (Table 5.1).

With the development of a more expansive, permanent, polar EAIS by the late Miocene, represented by the regional angular unconformity (i.e. the inferred polar to temperate/polythermal megasequence boundary), deeper seismic sequence boundaries were truncated and all subsequent reflectors maintained similar broad-scale geomorphologic features as the bathymetric surface. Reflectors below this regional unconformity show little correlation with the bathymetric surface or the unconformity above. Polar glacial MCS reflectors indicate shoaling to the east in front of the Reynolds Trough and an overall dip trending west toward the aforementioned bathymetric trough that strikes northwest in front of Totten Glacier and out towards the Budd Coast continental margin. I hypothesize that the morphology of regional polar ice sheets advancing out toward the Sabrina Coast continental margin during this time encountered conditions favorable to streaming ice flow across the western portion of the SCCS with slower flow across the Dalton Rise, resulting from: 1) lateral topographic forcing between Law Dome and the 124°E subglacial highlands, 2) the presence of calving margins and ice shelves (Figure 5.1), and 3) topographically controlled subglacial meltwater drainage [*Winsborro et al*, 2010; *Boyce & Eyles,* 2000].

Estimated polar glacial sediment volumes were significantly lower than the preglacial conditions, but better preserved than the temperate/polythermal glacial facies as erosional processes dominated the polar facies. Polar ice sheet modulation across the SCCS, a primarily erosional erosional environment, redistributed much of the prior temperate/polythermal deposition from the study area to the continental margin [*Siegert et al.,* 2004]. The relative thin veneer of polar glacial sediment in the SCCS study area (with an average thickness of 63.2 ms in TWTT), as evidenced in seismic section between the bathymetric surface and the regional angular unconformity, resulted in estimated at 278.6 +/- 148.8 km^3 assuming an average sequence velocity of 1600 m/s (Table 5.1). With polar glacial scouring evident across the SCCS through extensive sedimentary unconformities and bedrock exposure, polar glacial bedforms (including moraine, swales, and drumlins) are also clearly evident in multibeam swath bathymetry and indicative of ice retreat dynamics (Figure 5.3) as detailed by Domack et al [in preparation] and Fernandez et al [in preparation].

5.6 DISCUSSION

While polar glacial advance cycles generated unconformities in sequence, recent observations suggest that bedform deposition in this region occurred on the margins of ice sheet flow as the Totten Glacier and MUIS backstepped across an inner shelf of exposed bedrock and interconnected subglacial meltwater channels similar to the paleo-Pine Island Glacier retreat across the Amundsen Sea Embayment (ASE) shelf [*Kirshner et al.*, 2012; *Witus et al.*, 2014]. With braided or distributed subglacial drainage networks typifying upper glacial catchments (Figure 5.12), more arborescent or channelized subglacial drainage characterize the lower catchment region [*Clark and Walder*, 1994; *Boyce and Eyles*, 2000]. Schroeder et al. [2013] recently suggested that the transition between the two subglacial hydrologic systems occurs at the point of increasing surface slope, melt-water flux and basal shear stress distinguished by a hydrostatic equilibrium threshold with the overlying ice.

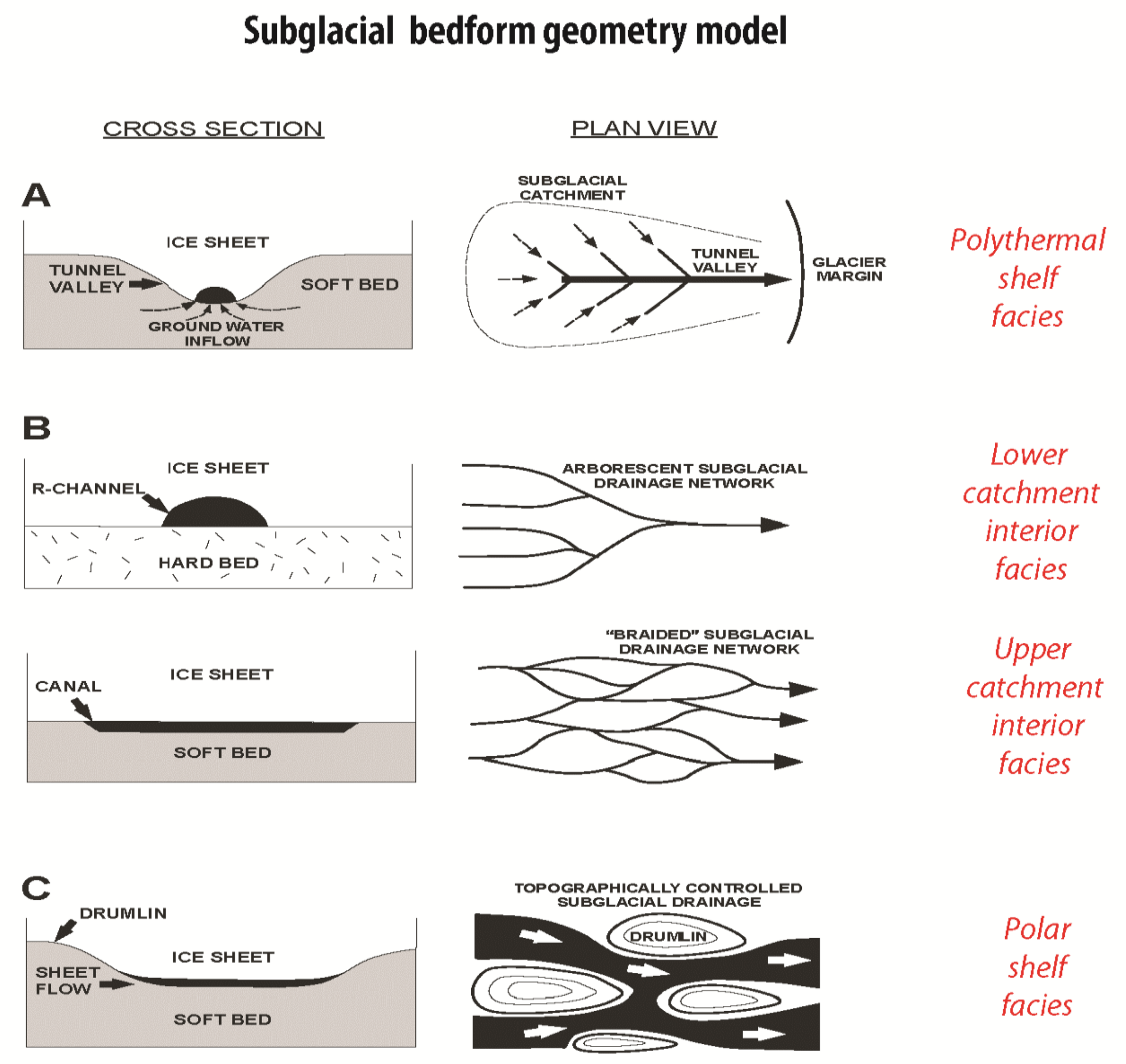

Figure 5.12: Model for Polar to Temperate/polythermal subglacial sediment facies–Modified from *Boyce and Eyles* [2000]. Cross sectional geometry and subglacial drainage pattern: A) sediment-floored tunnel valleys [*Boulton and Hindmarsh*, 1987], B) R-channels developed over bedrock (upper) and sediment-floored subglacial canals (lower) incised into sediments [*Clark and Walder*, 1994], and C) sheet flows moving in broad inter-drumlin swales during episodic nondeposition and ice-bed separation events [*Boyce and Eyles*, 2000].

While the initial retreat and extent of the polar ice front regress from the outer shelf across the inner shelf would have ultimately been determined by a combination of eustasy [*Alley and Whillans*, 1984; *Alley et al.*, 2005; *Anderson*, 2007], geothermal flux [*Pollard et al.*, 2005], bed topography [*Schoof*, 2007; *Jamieson et al.*, 2012], lateral topography and subglacial meltwater [*Winsborrow et al.*, 2010] forcing on Totten Glacier, the rate and dynamics with which these occur are highly dependent upon subglacial geology [*Alley et al.,* 2007; *Alley et al.,* 1986; *Blankenship et al.,* 1986]. Building upon these models, I suggest that the polar subglacial sedimentary bedforms are the product of initial distributed subglacial drainage networks under hydrostatic equilibrium with over lying ice developing into more channelized networks as the transition migrates into the basin interior with melt-water flux and surface slope changes resulting from the aforementioned glacial forcing mechanisms. Channelized subglacial drainage networks are especially apparent across bedrock (Figure 5.3), whereas topographically controlled subglacial flow prevailed in the central and eastern portion of the study area dominated by till and preexisting sedimentary bedforms established during glacial maxima when distributed subglacial drainage networks dominated amidst hydrologic equilibrium [*Boyce and Eyles*, 2000]. This marine geophysical hypothesis for the SCCS is consistent with shallow marine geologic data and limited age control to date, however, more expansive drilling data is warranted to confirm results.

5.7 CONCLUSIONS

A quantitative analysis of the first-ever high-resolution MCS data collected on the SCCS has revealed a detailed sequence stratigraphic framework illustrating preglacial, temperate/polythermal glacial, and polar glacial facies depicted substantial transitions in the evolution of the EAIS across the Totten Glacier catchment. An expansive preglacial megasequence lies atop an irregular basement surface dipping steeply to the north and shows definitive evidence of fluvial deposition. This preglacial megasequence, deposited during a geologic time interval spanning from the Cretaceous rift tectonics to late Eocene, represents over 66% of SCCS sediment by volume in the NBP14-02 study area (Table 5.1).

The overlying megasequence, representing an Oligocene-Miocene temperate/polythermal glacial-interglacial facies characterized by extremely efficient erosion rates [*Koppes and Montgomery*, 2009] with a sizeable amount of supra and subglacial meltwater flux [*Domack*, 1988], appears more diminished in the SCCS stratigraphic record comprising only 22.7% sediment by volume potentially due in part to subsequent remobilization of temperate/polythermal sediments to the continental margin during polar ice sheet modulation episodes. The onset of continental scale Antarctic glaciation at the Eocene-Oligocene boundary, including the development of temperate/polythermal ice sheets in the SCCS area, appear to coincide with a major unconformity (WL4) along the Wilkes Land margin [*Leitchenkov et al.,* 2007] coincident with the development of channel-levee systems across the continental margin.

The third and uppermost sedimentary megasequence represents polar glacial conditions, a predominantly erosive facies without evidence of subglacial meltwater, comprising only 11.1% of sedimentary deposition encountered in the SCCS study area. A multitude of glacial unconformities throughout both the polar and temperate/polythermal megasequences, including the first evidence of subglacial tunnel valleys on the Antarctic shelf and a variety of bedforms preserved on the bathymetric surface during the last glacial retreat, suggest a much more dynamic Neogene to Quaternary EAIS than has previously been modeled for the Wilkes Land margin [*DeConto and Pollard*, 2003]. The appraisal of these three primary megasequence sediment volumes with subglacial bedform models put forth by Boyce and Eyles [2000], Clark and Walder [1994], Boulton & Hindmarsh [1987], and Schroeder et al [2013, 2014] provide critical bed configuration and basal condition constraints required to model an ASB interior catchment that drains more than 1/8 of all East Antarctica.

Chapter 6: Conclusions and Future Work

6.1 CONCLUSIONS

In this dissertation, I investigate the distribution, thickness, and character of subglacial sedimentary basins contained within the ASB, WSB, and on the SCCS in front of the MUIS and associated Reynolds Trough. In doing so, I seek to provide additional basal ice dynamic constraint for climate models as well as a first-order estimation of subglacial and submarine sediment volumes for the ASB, WSB and a portion of the SCCS. In Chapter 3, initial ASB aerogeophysical data inversion workflows are established to reveal the first subglacial sedimentary basin isopach for the ASB. A series of interior sedimentary subbasins, of variable thickness from approximately 3.7 km to potentially as much as 12.5 km, are identified whose respective morphologies were associated with adjacent subglacial highlands (Ridge B and Dome C). These findings reinforced the Young et al [2011] hypothesis of EAIS advance retreat from a minimum of two ice sheet configurations from 34-14 Ma ago. Sediment distribution and volumes for the ASB subbasins suggested that high-sedimentation rates associated with post-middle Eocene temperate/polythermal glacial cycles substantially impacted geomorphologic development of the Wilkes Land topographic lowlands, particularly in subbasins VSB, ASB, and KSB, which would have had a reciprocal feedback on the nature of the EAIS oscillations during this time.

In Chapter 4, aerogeophysical data inversion workflows reveal the first complete subglacial sedimentary basin isopach for the entire WSB. Using a combination of radar, gravity and magnetic reduction techniques, a series of sub-basins (first identified by Ferraccioli et al [2009]) leading to the Southern WSB interior were mapped in the

Northern WSB with subglacial sediment thicknesses exceeding 2.5 km. The central and western basins, particularly, appear to coalesce to the south leading to a broad interior basin in the Southern WSB characterized by a low isostatic residual anomaly, low basal roughness, deep magnetic DTB response, and sediment thicknesses averaging 1.6 km and exceeding 6 km in certain locations.

Comparing sediment isopachs of the northern versus southern ASB and WSB regions, the northern subbasins are on the whole characterized by more isolated, channelized deposits including the SSB in the ASB region and the central and western basins in the WSB region. These restricted sedimentary subbasin deposits also appear directly associated with major outlet glacier catchments including the Totten Glacier in the ASB and the Cook and Mertz Glaciers in the WSB. Overall thicker sedimentary sequences were noted as coincident with preglacial drainage and tectonic structures in the Northern and Southern WSB and areas of selective linear erosion as modeled by Jamieson et al. [2014] who further suggested that the long term impact along regional hydraulic and ice flow and erosion pathways may give rise to further ice sheet instability such areas below present day sea level. Sediment deposition in the more northern ice margin proximal areas of the ASB and WSB was undoubtedly impacted by denudative effects of EAIS oscillations on more finite time scales.

Based upon these ASB and WSB subglacial sedimentary basin isopach results, a more dynamic EAIS hypothesis was suggested for the Wilkes Land region during polar glacial periods characterizing the Pliocene-Pleistocene. This hypothesis remains in stark contrast to the relatively stable ice models for this area that had been previously proposed [*Ritz et al.,* 2001; *Huybrechts,* 2002; *DeConto and Pollard,* 2003; *Pollard and DeConto,* 2009; *Nowicki,* 2013], but is reinforced by a multitude of glacial advance-retreat cycles detailed in the SCCS MCS sequence stratigraphy of Chapter 5. Recent dynamic WSB ice volume models by Cook et al [2013] and Mengel and Levermann [2014] support this contention for Pliocene EAIS instability in Wilkes Land during an epoch characterized by low atmospheric CO_2 concentrations [*Pollard et al.,* 2015].

Chapter 5 specifically sought to examine the character of Wilkes Land glacial sedimentation in more detail, specifically evaluating dynamic ice hypotheses proposed based on aerogeophysical investigations in the EAIS interior, through detailed assessment of SCCS sequence stratigraphy and sediment volumes associate with the Totten Glacier catchment. The uppermost SCCS stratigraphic record, reinforced the dynamic EAIS hypothesis with evidence of several polar glacial ice advance-retreat cycles topped by a complex bathymetric geometry of glacially carved bedforms including constructional grounding line wedges, dune forms, drumlins, megawaves, and lineated/corrugated subglacial surfaces. Three primary megasequences in all were identified, constrained by targeted geologic sampling of outcropping strata, to represent polar glacial, temperate/polythermal glacial, and fluvial/pre-glacial facies presumably extending back to syn-rift deposition associated with the Cretaceous separation of Wilkes Land from South Australia.

The unconsolidated glacial diamictite characterizing the temperate/polythermal and polar glacial megasequences were separated by a regional angular unconformity of stratified diatomite and gravel-rich diatom-bearing sandstone with a sharp transition to a sandy diamictite representing the Late Miocene evolution of temperate/polythermal to polar-based conditions and the advance of the EAIS to the Wilkes Land continental margin. The temperate/polythermal megasequence, indicative of the dynamic cyclicity of the EAIS from 34-14 Ma ago, contained at least seven distinct glacial advance-retreat episodes as resultant glacial unconformities with extensive subglacial tunnel valleys indicative of temperate/polythermal glacial conditions and catchment groundwater flux. Preglacial megasequence sedimentation was distinguished with two distinct clinoforms evident in the MCS record and paleobotanical evidence from geologic cores. This fluvial-dominated preglacial megasequence represented over 66% by volume of the limited SCCS area able to be surveyed during the Austral Summer of 2014-2015 aboard the NBP14-02 scientific cruise due to sea ice conditions. The preglacial sediment volumes can be compared to just 11.1% and 22.7% by volume for the polar and temperate/polythermal megasequences, respectively.

Ultimately, the high-resolution, limited scope marine geologic and geophysical evidence presented in Chapter 5 illustrated the complex fluvial to glacial basin-scale geomorphologic dynamics that must be incorporated into any regional model. As such, this dissertation has provided provide critical bed configuration and basal condition constraints required for accurate global and regional climate models over an area draining more than 1/8 of the EAIS.

6.2 FUTURE WORK

An additional avenue of future work will include a detailed assessment of benthic geology characterization in an effort to establish either a terrestrial or marine forcing mechanism prompting the last glacial cycle across the SCCS. Projected completion of this work has been delayed with noisy and potentially corrupted multibeam backscatter data adding to processing delays and coordinated intercollegiate efforts to expedite publication of the detailed NBP14-02 swath multibeam bathymetry interpretation. As initially proposed, statistical quantification of bathymetry and backscatter data can be associated with seafloor geology and a degree of similarity calculated for separate features [*Mitchell and Clarke,* 1994]. Complimentary geophysical information from high-resolution MCS and the Knudsen 3.5 kHz chirp sub-bottom profiles may be utilized to reinforce the model. Additionally, geologic core and dredge sample data can be used to ground-truth the geophysical interpretations. Finally, geochemical analysis of glacial till porewaters may provide further evidence as to the relative timing of marine incursion during glacial retreat [*Rayne and Domack,* 1996].

Appendix A

A1.0: ICECAP SURVEY

To better understand the basal conditions and configuration of the EAIS across much of Wilkes Land, the International Polar Year (IPY) ICECAP project was launched in 2008, representing multiyear international collaborative effort of seven nations to explore the ASB, WSB, and associated subglacial basins residing below present day sea level. Given the thick, expansive ice cap across the study area, the ICECAP survey was designed as an aerogeophysical survey using a Basler BT-67 aircraft (Figure A1.1) equipped with a HiCARS coherent 60-MHz ice-penetrating radar [*Peters et al.,* 2005], laser range-finder, gravity meter, and magnetometer.

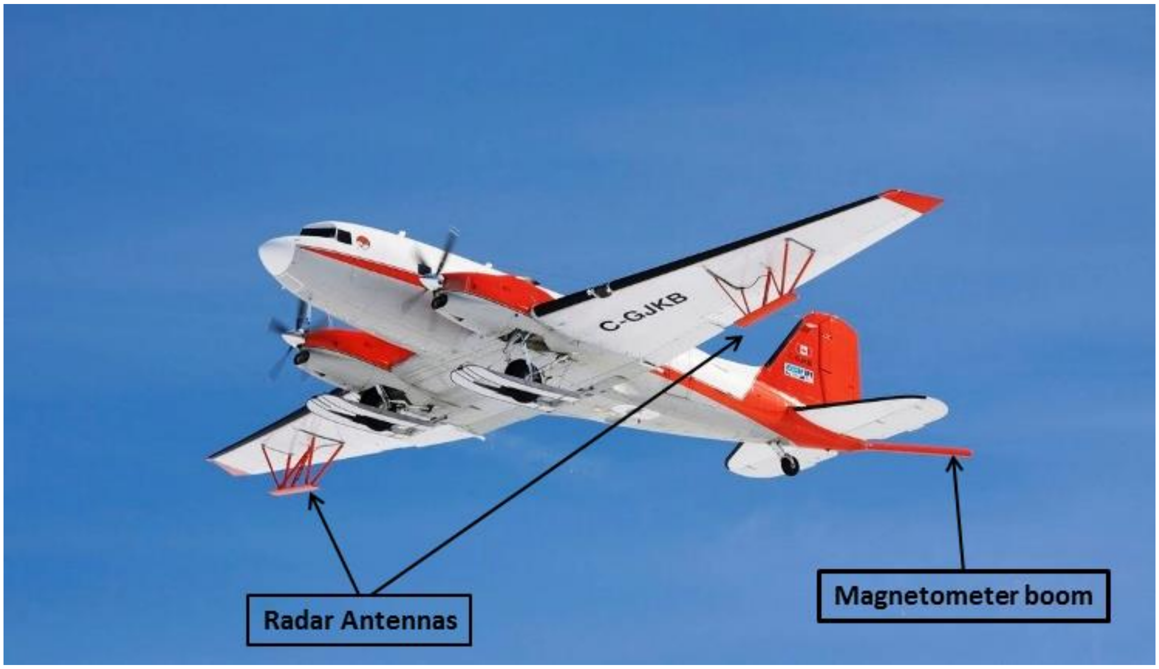

Figure A1.1: Basler BT-67 (a version of a Douglas DC-3 retrofitted with turboengines). Maximum survey distance = 2,000 km (7 hrs flight time).

ASB and WSB ICECAP surveys utilized consistent gravity, magnetic, GPS, and laser altimeter instrumentation with the exception of the addition of a LIDAR system starting during the 2010-2011 field season, as part of the ICEBRIDGE program, and a gravity meter upgrade during the final 2012-2013 field season. Equipment specifications are presented in Tables A1.1-A1.6 with the exception of the LIDAR system whose data is not presented herein.

System Name	Coherency	Frequency (MHz)	Bandwidth (MHz)	Along-track Sampling Rate (Hz)
HiCARS	Coherent	Center Chirp 60	15	200

Table A1.1: Radar Instrumentation Specifications

Make/Model	Track-line sampling distance (m)	Max Range (m)	Accuracy (cm)
Riegel LD90-3800 HiP-LR	15	>2000	25

Table A1.2: Laser Altimeter Instrumentation Specifications

Make/Model	Measurement Method	Sample Rate (Hz)	Precision (nT)
Geometrics 823A	Cesium vapor	10	0.1

Table A1.3: Magnetometer Instrumentation Specifications

Make/Model	Sampling Rate (Hz)	Navigation Accuracy (m)
Ashtech GG-24 GLONASS/GPS	1	10
Trimble Trimflight differential GPS Navigation System	1	5

Table A1.4: GPS Receiver Timing and Navigation Instrumentation Specifications

Make/Model	Sampling Rate (Hz)
Ashtech Z-surveyor	1
Trimble 5700	1

Table A1.5: GPS Receiver Positioning Instrumentation Specifications

System Name	Platform Period (sec)	Sampling Rate (Hz)
Bell Aerospace BGM-3 (2 axis)	533	1
GT1A (3 axis)	Schuler-tuned	1

Table A1.6: Gravity Instrumentation Specifications

A.1.1 Survey Locations

During five austral summers stretching from 2008-2013, more than 113,000 km of new aerogeophysical data were collected across the ASB and over 75,000 km across the adjacent WSB (Figure A1.2). Radial flights from Casey Station were undertaken to maximize coverage of the interior ASB, with similar radial flight plans emanating from McMurdo Station to cover much of the southern WSB. Reflights of ICESAT orbital tracks and coast-parallel tie lines were also completed as part of a concurrent NASA Operation ICEBRIDGE research effort.

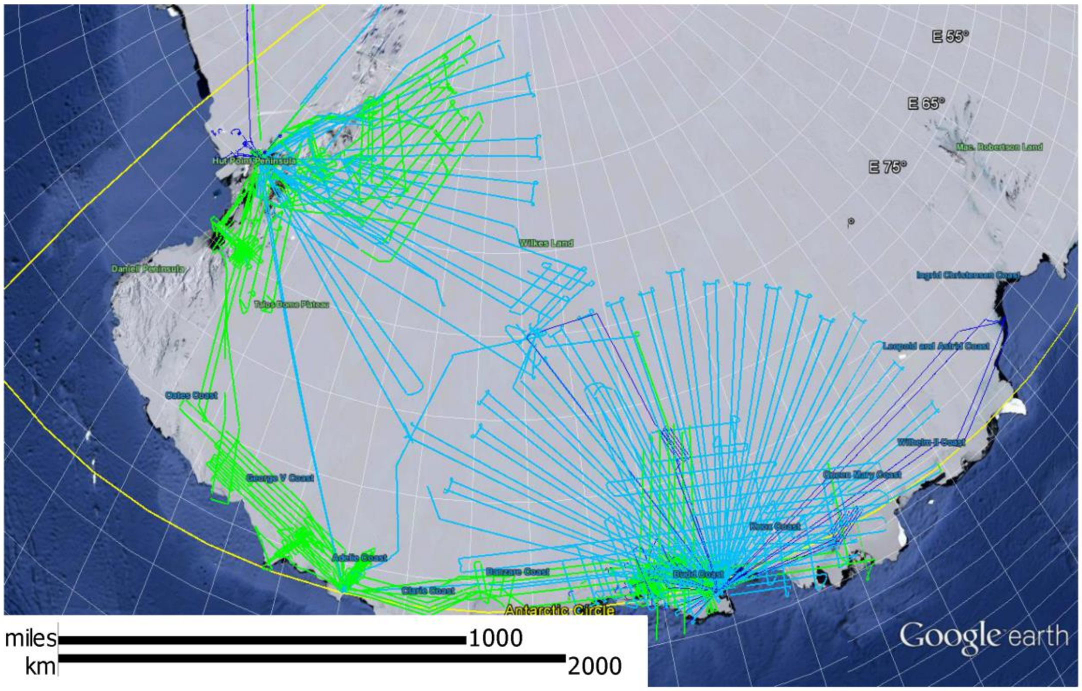

Figure A1.2: ICECAP-ICEBRIDGE Survey Flight Paths: Austral Field Seasons 2008-2013.

A1.2 Gravimeter Operation, Specs & Preprocessing

The gravity data were collected using a Bell Aerospace BGM-3 gravimeter on loan from the U.S. Naval Oceanographic Office (Figure A1.3). Originally developed for marine surveys, the BGM-3 was modified for airborne surveying by lengthening its natural oscillation period from the default setting. The BGM-3 uses an electronically levitated proof mass to quantify vertical acceleration [*Filina et al.*, 2006].

Figure A1.3: Interior of Basler BT-67 with UTIG aerogeophysical suite.

The raw gravity data were subsequently processed at UTIG adjusting for non-gravitational accelerations including aircraft acceleration, elevation, pitch, yaw, tilt. Eötvös, latitude and instrument drift corrections were also applied based upon a GPS position solution. Resultant free-air gravity uncertainties were quantified following initial processing using repeat-track and grid crossover analysis to achieve an estimated 3 mGal free-air RMS accuracy [*Holt et al.*, 2006; *Richter, et al.,* 2001].

A1.3 Magnetometer Operation, Specs, & Preprocessing

Magnetic field strength measurements were concurrently collected during ICECAP surveys using a Geometrics 823A Cesium Magnetometer. Magnetic data were collected at 10 Hz with an estimated precision of 0.001 nT. Magnetic field strength data were processed using standard methods, including corrections for the IGRF, the diurnal field and leveling and crossover gridding. Diurnal corrections were applied using permanent observatories at Casey Station, Dome C (Concordia), and Dumont d'Urville

Stations. Because magnetic readings at any one point in time varied considerably, flight data were linearly weighted according to the distance of the data from the respective permanent observatory [*Ferraccioli et al.*, 2013].

A1.4 Ice-Penetrating Radar Operation, Specs & Preprocessing

Radar data were collected using a coherent ice-penetrating 60 MHz radar system with a 15 MHz bandwidth [*Schroeder et al.,* 2013; *Peters et al.,* 2007; *Peters et al.*, 2005]. Radar data were pulse-compressed and processed using a short synthetic-aperture radar aperture to retain energy; with this level of processing, range distortions are not significant on length scales greater than 400 m [*Young et al.,* 2011]. The ice thickness was found using a speed of light in ice of 169 m/µs, and the bed elevation was calculated using the radar-determined surface elevation. Radar data were down-sampled to 1 Hz to coincide with recorded gravity and down-sampled magnetic datasets.

A2.0 WLK SURVEY

The WLK campaign of 1999-2000 used a Twin Otter aircraft platform operated by the National Science Foundation's (NSF) Support Office for Aerogeophysical Research (SOAR). Aerogeophysical survey equipment used in the WLK campaign is outlined in Table 4.1 and described in further detail in the following sections. The WLK survey extended from the TAM to the subglacial Adventure Trench, covering a 133,400 km^2 swath of the WSB interior (Figure A2.1). The WLK survey was flown in a gridded pattern with flight lines 10.6 km apart and tie lines every 31.8 km, totaling more than 21,000 line kilometers of airborne gravity, magnetic and ice-penetrating radar data. Survey grids were flown as two blocks in the eastern and western portions of the survey area, respectively; the eastern grid was flown at a constant altitude of 3050 m, and the western grid was flown at a constant elevation of 3750 m with additional profiles supplemented resulting in a final line spacing of 5.3 km.

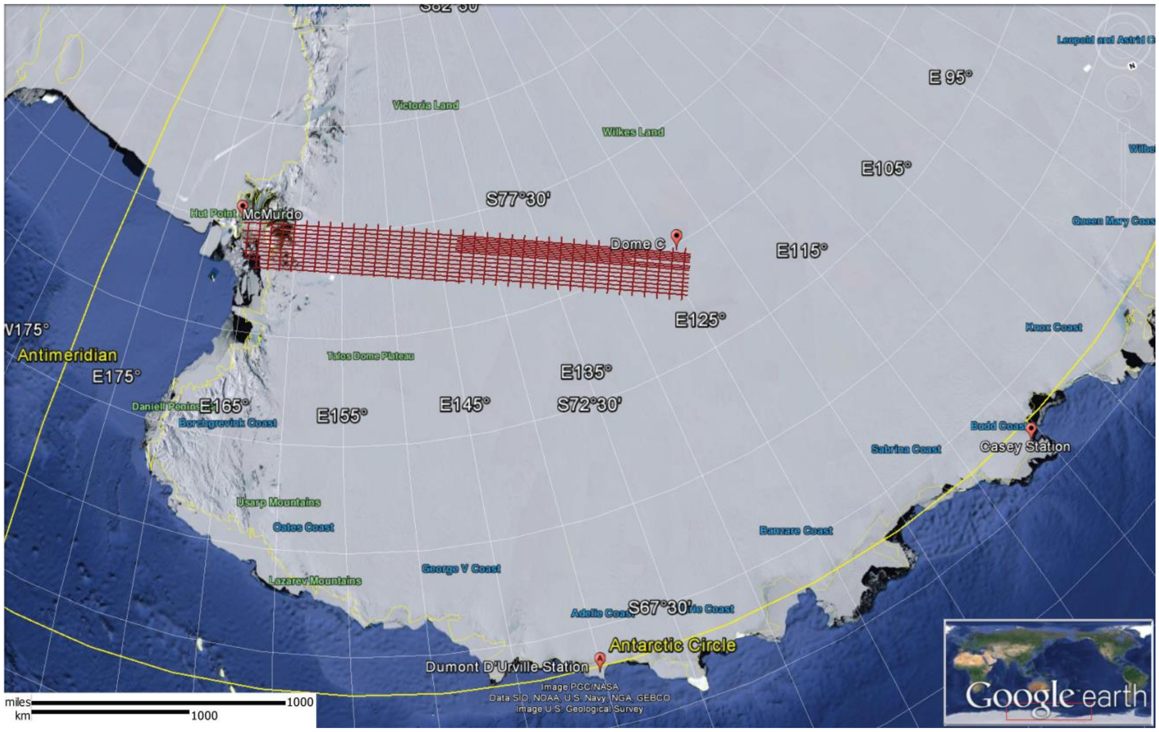

Figure A2.1 WLK Survey Flight Paths: Austral Field Season 1999-2000.

A2.1 WLK Gravity Specs & Preprocessing

Similar to the aforementioned ICECAP aerogeophysical survey, gravity data were collected using a Bell Aerospace BGM-3 gravimeter mounted on a gyro-stabilized platform. Post-acquisition airborne gravity measurements were corrected for vertical acceleration, pitch, yaw and roll of the aircraft using dual-frequency carrier phases of GPS data collected simultaneously by three receivers on the aircraft and at the base station at a 1-Hz sampling rate. Noise was removed from the raw gravity data by employing a low-pass cosine taper filter in the frequency domain. Corrections for instrument drift, latitude, Eötvös, and altitude were subsequently employed to yield free-air gravity (Figure 4.2). Cross-over errors were minimized by linear trend removal to achieve a standard deviation of <3 mGals [*Studinger et al.,* 2004]. The free air gravity results from both eastern and western survey grid blocks were upward continued to 3950 m in the frequency domain to facilitate a constant elevation with the composite data from the ICECAP and WISE-ISODYN surveys.

A2.2 WLK Magnetometer Operation, Specs, & Preprocessing

Total magnetic intensity was recorded by Geometrix 823A Cesium vapor magnetometer towed behind the Twin Otter aircraft similar to the ICECAP survey. Although magnetic data were collected at 10 Hz with a precision estimated at 0.001 nT, the data were down-sampled to 1 Hz to coincide with gravity and down-sampled radar datasets. Diurnal corrections were applied using the permanent observatory at McMurdo Station with subsequent IGRF removal to obtain the total magnetic field anomaly.

A2.3 WLK Ice-Penetrating Radar Operation, Specs & Preprocessing

Radar data were collected using a coherent ice-penetrating 60 MHz radar system with a 15 MHz bandwidth [*Schroeder et al.,* 2013; *Peters et al.,* 2007; *Peters et al.,* 2005]. Radar data were pulse-compressed and processed using a short synthetic-aperture radar aperture to retain energy; with this level of processing, range distortions are not significant on length scales greater than 400 m [*Young et al.,* 2011]. The ice thickness was found using a speed of light in ice of 169 m/μs, and the bed elevation was calculated using the radar-determined surface elevation. Radar data were down-sampled to 1 Hz to coincide with recorded gravity and down-sampled magnetic datasets.

A3.0 WISE-ISODYN SURVEY

The WISE-ISODYN campaign of 2005-2006 was an international collaborative effort between the British and Italian Antarctic programs to fly over 60,000 line kilometers of aerogeophysical data over the Northern WSB [*Bozzo and Ferraccioli,* 2007] to better constrain regional crustal structure and Neogene dynamics of the EAIS. Aeromagnetic, gravity and ice-penetrating radar equipment was mounted on a British Antarctic Survey (BAS) Twin Otter platform (Figure A3.1). Some 68 survey flights were flown in a gridded pattern over an area of 767,300 km^2 at constant nominal elevation of 2400 m (Figure A3.2). Flight line spacing was generally set at 8.8 km, with the exception of the western portion of the grid flown at 26.4 km due to fuel logistical constraints, tie lines were flown every 44 km [*Ferraccioli et al.,* 2009].

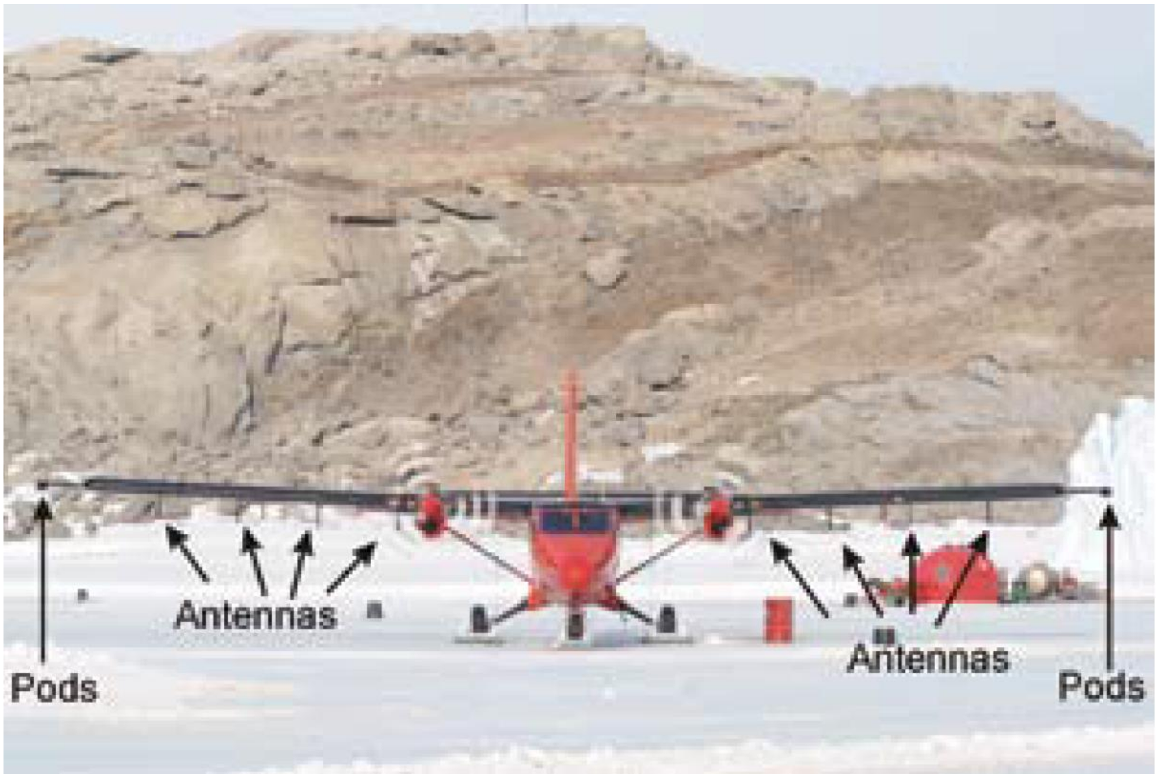

Figure A3.1: WISE-ISODYN BAS Twin Otter configuration. Maximum survey distance = 1,000 km.

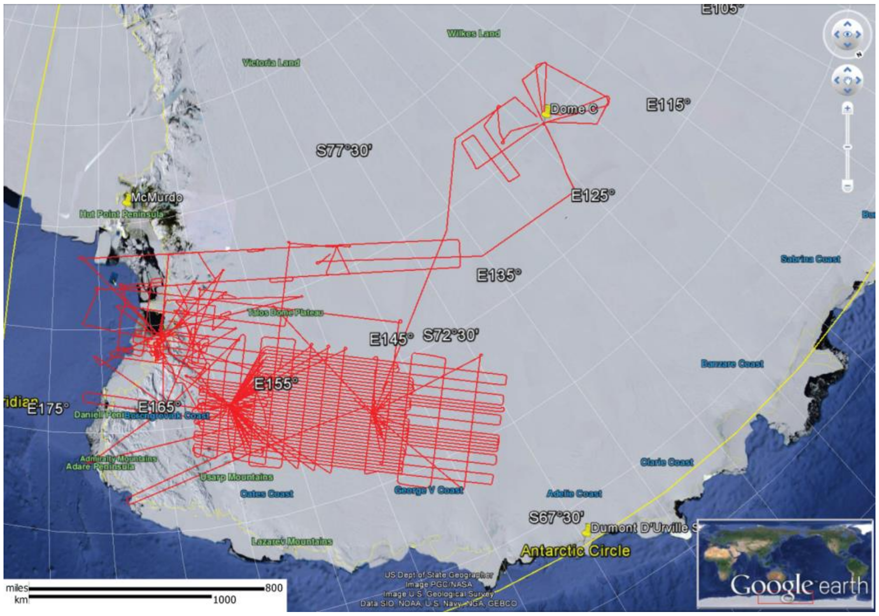

Figure A3.2: WISE-ISODYN Survey Flight Paths: Austral Field Season 2005-2006.

A3.1 WISE-ISODYN Gravity Specs & Preprocessing

A LaCoste and Romberg air-sea gravimeter [*LaCoste,* 1967], modified by Zero Length Spring (ZLS) Corporation [*Vallient,* 1992], was equipped with a gyro-stabilized platform and an external control system and mounted at the center of motion of the BAS Twin Otter aircraft [*Ferraccioli et al.,* 2007]. Post-acquisition airborne gravity measurements were corrected for vertical acceleration, pitch, yaw and roll of the aircraft using dual-frequency differential GPS data collected simultaneously by three receivers on the aircraft. Noise was removed from the raw gravity data by employing a low-pass cosine taper filter in the frequency domain. Corrections for instrument drift, latitude, Eötvös, and altitude were subsequently employed to yield free-air gravity.

A3.2 WISE-ISODYN Magnetometer Operation, Specs, & Preprocessing

Two Scintrex Cs3 optically-pumped Cesium magnetometers were installed in pods and mounted on each wing-tip of the BAS Twin Otter (Figure A3.1) to record the total magnetic field intensity with an accuracy of 0.001 nT [*Ferraccioli et al.,* 2007]. The optical portion of the Scintrex magnetometer system was set at a 45° gimble orientation to reduce data spikes and noise associated with the magnetic dead zone characteristic in high latitudes. To assist in post-acquisition processing, a Billingsley 3-axis fluxgate magnetometer was installed in the tail of the aircraft to compensate for the airframe-induced magnetic field. Pico Envirotec magnetic compensation algorithms were subsequently employed to correct the raw magnetic data for airframe-induced magnetic fields including pitch, yaw, roll, and heading (PEIComp, 2004). Magnetic base stations, consisting of Scintrex MP3 and Geometrics G856AX instrumentation, were also deployed at Mario Zucchelli, Sitry, and Talos Dome to subsequently correct for diurnal magnetic field variations [*Ferraccioli et al.,* 2007].

A3.3 WISE –ISODYN Ice-Penetrating Radar Operation, Specs & Preprocessing

The BAS ice-penetrating radar system operates on a carrier frequency of 150 MHz with a bandwidth of 10 MHz. It is designed as a dual-pulse system with a short-single frequency pulse to yield high-resolution imaging of the near surface ice layers and a longer, high power chirped pulse for subglacial bed imaging. Along-track resolution is estimated at 10 cm pre-processed and 1 m post-processing based on an average aircraft velocity of 70 m/s, a sample period of 64 μs and stacking at 25. The subglacial bed resolution, based on chirp, period and bandwidth is estimated at 8 m [*Ferraccioli et al.*, 2007].

A4.0 TOTTEN GLACIER SYSTEM AND MARINE RECORD OF CRYOSPHERE-OCEAN DYNAMICS (AKA WILCO) SCIENTIFIC RESEARCH CRUISE NBP14-02

The WILCO project was the first investigation consigned to investigate the cryosphere-ocean dynamics specifically impacting the Totten Glacier and MUIS in Western Wilkes Land, East Antarctica. More broadly, the WILCO project complemented regional ASB investigations, including ICECAP and IceBridge, to more accurately constrain basal ice conditions and potential forcing mechanisms across geologic time. Substantially enhancing meager oceanographic and marine geology/geophysical records on the SCCS, the WILCO expedition leveraged the scientific capacity of the RVIB *Nathaniel B. Palmer* ice breaker (Figure A4.1) to collect marine gravity, magnetics, multi-channel seismic, and geologic and physical oceanographic data to better assess present and past sensitivity of this glacial system to environmental forcing. Swath multibeam, marine gravity and MCS data were the primary datasets utilized in this study and are thereby discussed in further detail below.

Figure A4.1: WILCO Survey: RVIB *Nathaniel B. Palmer* ice breaker

A4.1 WILCO Gravity Specs & Preprocessing

A 2-axis gyro-stabilized Bell BGM3 gravimeter replaced a malfunctioning LaCoste and Romberg Air-Sea ZLS gravimeter for the NBP14-02 scientific cruise (Figure A4.2). Similar to the Bell BGM3 gravimeters utilized during the ICECAP, IceBridge, and WLK airborne surveys, the gyro-stabilized platform facilitated filtering of the raw gravity data according to the speed and acceleration of the NBP (specifically, the pitch and roll) such that vertical accelerations due to variations in the gravity field could be isolated. A total of 5,230 km of continuous gravimetry data were collected over the SCCS. Gravity ties were completed pre and post cruise in Hobart, Tazmania at several locations to calculate and correct for instrument drift. The base station gravity tie loops closed well with a drift of ~2.4 mGals and as such were deemed acceptable [*Leventer et al.,* 2014]. Subsequently corrections for instrument drift, latitude, and Eötvös were subsequently employed to yield free-air gravity. Noise was removed from the raw gravity data by employing a low-pass cosine taper filter in the frequency domain.

Figure A4.2: WILCO Survey: Bell BGM3 gravimeter platform – Electronics module (left) and gyro-stabilized platform (right) shown here.

A4.2 WILCO Multichannel Seismic Specs & Preprocessing

High-resolution 2D MCS data were collected using two Sercel G.I. airguns and a hot spare configured at 45/45 in^3 (harmonic mode), a Real-Time Systems HotShot shotbox, and a gel-filled Teledyne 24-channel streamer with 3.125 m channel spacing and 3 hydrophones per channel [*Leventer et al.*, 2014]. The air source was towed at approximately 3 m depth and fired every 5 seconds for a nominal shot spacing over the bathymetric surface of an estimated 12.5 m. The geometry of the towed array is shown in Figure A4.3. The source frequency content was 20-300 Hz with a maximum power between 100-160 Hz.

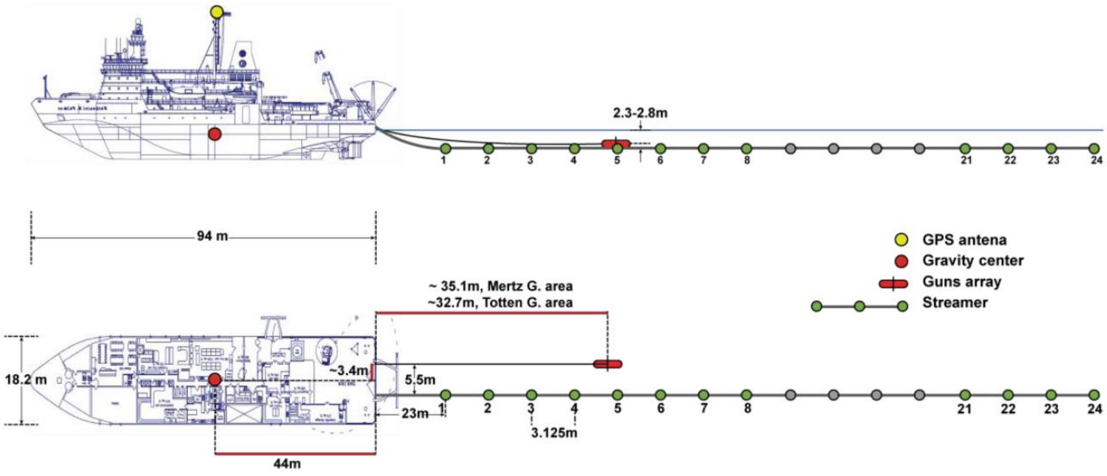

Figure A4.3: WILCO Survey: NBP14-02 seismic array geometry.

Analog signal response from the streamer was fed into a Geometrics Geode, digitized, and recorded to a laptop in SEGY format. Real-time MCS processing was then performed onboard using Paradigm's Echos® software to establish a "brute" stack for quality control. Following initial processing more advanced shotpoint geometry corrections were made utilizing the shipboard GPS receivers and shot data to correct for the offset of the G.I. guns with respect to the NBP center of gravity and the NBP crabbing. A UTM 50S coordinate system was utilized for all Sabrina Coast scientific data collection activities. Following shotpoint geometry correction, final shipboard MCS processing sequences (detailed in Table A4.1) were completed prior to final MCS data export to Halliburton's Landmark DecisionSpace® interpretation software.

1. Conversion of Geode data from SEGY format*
2. Polarity Reversal* (streamer input polarity is reversed from convention)
3. Bandpass Filter* (Butterworth 30-450 Hz)
4. Geometry Correction
5. F/K Filter (removes water velocity arrivals)
6. Spherical Divergence Correction (velocity pick based)
7. Trace Balance
8. Noise Reduction
9. CDP Sort*
10. Velocity Analysis
11. NMO Correction*
12. Offset Mute
13. Seafloor Mute
14. CDP Stack (6 fold nominal)*
15. F/K Migration*
16. SEGY Output*

* - Denotes preliminary "brute" MCS processing sequence

Table A4.1: WILCO Survey: Shipboard MCS Processing Sequence Summary. Additional detail provided in NBP14-02 Cruise Report authored by Leventer et al. [2014].

A4.3 WILCO Swath Multibeam Specs & Preprocessing

A hull-mounted Kongsberg Maritime Simrad EM 120 multibeam echosounder with 191 beams and an open-angle of 120°, corresponding to a swath 3.5 times water depth, was utilized to map seafloor bathymetry throughout the NBP14-02 cruise (Figure 5.3). Operating at 12 kHz, the multibeam swath soundings were automatically corrected for vessel heave, pitch, roll, heading and position with two Seatex MRU-5 motion sensors and a Kongsberg Seapath 330 processing unit, as well as surface seawater salinity and temperature though integrated shipboard GPS and underway acoustic Doppler current profiler (ADCP) sensors. Raw multibeam data were logged and transferred real-time to a Caris HIPS/SIPS® software (http://www.caris.com) processing machine. Bad data points (bed reflections) outside the valid depth range were edited out for each hour of data collected and subsequently exported in XYZ format for display in ESRI's ArcGIS® platform (http://www.arcgis.com).

Appendix B

The following publically available datasets were utilized as supplemental regional data in construction of Wilkes Land structural and potential field models.

B1.0 BEDMAP2

Perhaps the most prominent recent example of ICECAP data contribution (field seasons 2008-2009 & 2009-2010) to expanded scientific knowledge was the recent Bedmap2 compilation of Antarctic geophysical and cartographic data to produce comprehensive grids of surface elevation, ice thickness, bathymetry and subglacial bed elevations [*Fretwell et al,* 2013]. ICECAP airborne surveys across the ASB and WSB provided Fretwell et al [2013] with some of the first GPS-corrected aerogeophysical data constraints across much of the vast Wilkes Land interior. In turn, Bedmap2 data (Figure B1.1) was used extensively during this research particularly to generate 3D layered models used during forward and inverse calculations of potential field response.

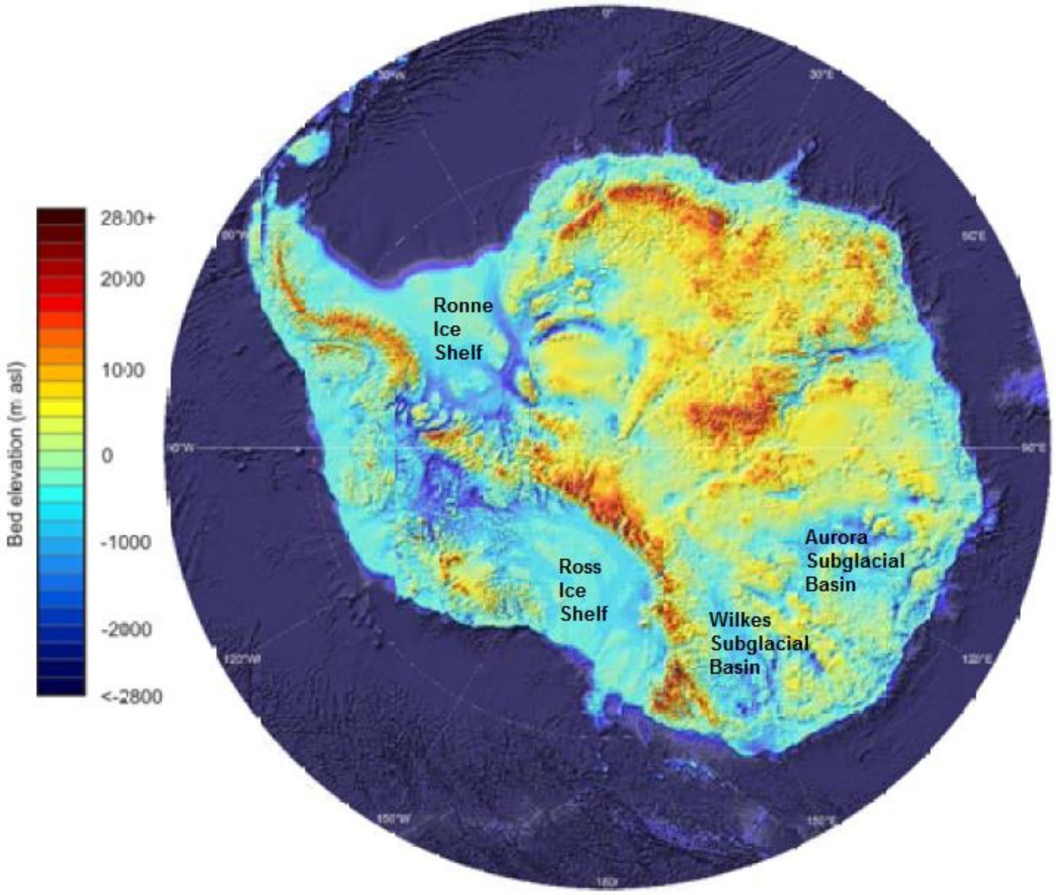

Figure B1.1: Bedmap2 Subglacial Bed Elevation Data [*Fretwell et al,* 2013].

B2.0 GOCE SATELLITE GRAVITY DATA

The GOCE mission was launched in 2009 by the European Space Agency (ESA) and tasked with mapping the Earth's gravity field in unprecedented detail. A measurement accuracy of 1 mGal and an improved spatial resolution of 100 km were achieved by combining a low orbit in the upper thermosphere (260 km altitude versus 500 km altitude of the Gravity Recovery and Climate Experiment [GRACE]) and a highly sensitive gravity gradiometer with 3-axis accelerometers resulting in a geoid accuracy of 1-2 cm. GOCE's higher frequency data provided for better estimates of polar ice sheet thickness and flux, ocean current and heat transport, and lithosphere geodynamics including uplift, subduction and sedimentary basin regions [*Drinkwater. et al.,* 2008]. GOCE satellite data were used in this study when appropriate as a guide for identifying regional gravity signals in airborne gravity datasets [*Muller and Smith,* 1993; *Kern et al.,* 2003].

References

Aitken, A. R. A., D. A. Young, F. Ferraccioli, P. G. Betts, J. S. Greenbaum, T. G. Richter, J. L. Roberts, D. D. Blankenship, and M. J. Siegert (2014), The subglacial geology of Wilkes Land, East Antarctica, *Geophys. Res. Lett.*, *41*, 2390–2400, doi:10.1002/2014GL059405.

Alley, R., and D. Blankenship (1987), Till beneath ice stream B: 4. A coupled ice-till flow model, *J. Geophys. Res.*, *92*(B9), 8931–8940.

Alley, R., S. Anandakrishnan, and T. Dupont (2007), Effect of sedimentation on ice-sheet grounding-line stability, *Science (80-.).*, *315*(5820), 1838–41, doi:10.1126/science.1138396.

Alley, R. B., and I. A. N. M. Whillans (1984), Response of the East Antarctica Ice Sheet to Sea-Level Rise, *J. Geophys. Res.*, *89*(C4), 6487–6493.

Alley, R. B., D. Blankenship, C. Bentley, and S. T. Rooney (1986), Deformation of till beneath ice stream B, West Antarctica, *Nature*, *322*, 57–59.

Alley, R. B., D. D. Blankenship, and C. R. Bentley (1987), Till Beneath Ice Stream B, *J. Geophys. Res.*, *92*(89), 8921–8929.

Alley, R. B., P. U. Clark, P. Huybrechts, and I. Joughin (2005), Ice-Sheet and Sea-Level Changes, *Science (80-.).*, *310*, 456–460.

Amos, J. (2006), Survey targets "ghost" mountains, *BBC News*.

Anandakrishnan, S. and Winberry, J. P. (2004), Influence of Subglacial Sedimentary Layer Thickness from Receiver Function Analysis, *Glob. Planet. Chang.*, *42*, 167–176.

Anderson, J. (2007), Ice sheet stability and sea-level rise, *Science (80-.).*, *315*, 1803–1804.

Anderson, J. B. (1991), The Antarctic Continental Shelf: results from marine geological and geophysical investigations, in *The Geology of Antarctica*, edited by R. J. Tingey, pp. 285–326, Oxford, U.K.

Anderson, J. B., and E. W. Domack (1991), Foreward, in *Glacial Marine Sedimentation: Paleoclimatic significance*, edited by J. B. Anderson and G. M. Ashley, pp. v–vii, Geological Society of America.

Bahr, D. B., E. W. H. Hutton, J. P. M. Syvitski, and L. F. Pratson (2001), Exponential approximations to compacted sediment porosity profiles, *Comput. Geosci.*, *27*(6), 691–700, doi:10.1016/S0098-3004(00)00140-0.

Bamber, J. L., R. E. M. Riva, B. L. A. Vermeersen, and A. M. Lebrocq (2009), Reassessment of the Potential of the West Antarctic Ice Sheet, *Science*, *324*(5929), 901–904.

Bannister, S., J. Yu, B. Leitner, and B. L. N. Kennett (2003), Variations in crustal structure across the transition from West to East Antarctica, Southern Victoria Land, *Geophys. J. Int.*, *155*, 870–880.

Baranov, A., and A. Morelli (2013), The Moho depth map of the Antarctica region, *Tectonophysics*, *609*(SI), 299–313, doi:10.1016/j.tecto.2012.12.023.

Barrett, P. J. (1996), Antarctic palaeoenvironment through Cenozoic times-a review, *Terra Antart.*, *3*, 103–119.

Barrett, P. J. (2013), Resolving views on Antarctic Neogene glacial history – the Sirius debate, *Earth Environ. Sci. Trans. R. Soc. Edinburgh*, *104*(01), 31–53, doi:10.1017/S175569101300008X.

Bentley, C. (1964), Research in Geophysics, edited by H. Odishaw, pp. 335–389, Massachusetts Institute of Technology, Cambridge, US.

Blankenship, D., C. Bentley, S. T. Rooney, and R. B. Alley (1986), Seismic measurements reveal a saturated porous layer beneath an active Antarctic ice stream, *Nature*, *322*, 54–57.

Blankenship, D. D., D. A. Young, T. G. Richter, and J. S. Greenbaum (2014), *IceBridge CMG GT-1A Gravimeter L2 Geolocated Free Air Gravity Disturbances*, NASA National Snow and Ice Data Center Distributed Active Archive Center, Boulder, Colorado USA.

Bo, S., M. Siegert, S. Mudd, and D. Sugden (2009), The Gamburtsev mountains and the origin and early evolution of the Antarctic Ice Sheet, *Nature*, *459*(7247), 690–3, doi:10.1038/nature08024.

Boger, S. (2011), Antarctica—before and after Gondwana, *Gondwana Res.*, *19*(2), 335–371, doi:10.1016/j.gr.2010.09.003.

Boulton, G. S., and R. C. A. Hindmarsh (1987), Sediment deformation beneath glaciers: Rheology and geological consequences, *J. Geophys. Res.*, *92*(B9), 9059, doi:10.1029/JB092iB09p09059.

Boyce, J. I., and N. Eyles (2000), Architectural element analysis applied to glacial deposits: Internal geometry of a late Pleistocene till sheet, Ontario, Canada, *Geol. Soc. Am. Bull.*, *112*(1), 98–118, doi:10.1130/0016-7606(2000)112<98:AEAATG>2.0.CO;2.

Bozzo, E., and F. Ferraccioli (2007), The Italian-British Antarctic Geophysical and Geological Survey in Northern Victoria Land 2005/2006-toward the International Polar Year 2007/2008, *Terra Antarct. Reports*, (13), 1–6.

Ten Brink, U., and T. A. Stern (1992), Rift Flank Uplifts and Hinterland Comparison of the Transantarctic Mountains With the Great Escarpment of Southern Africa, *J. Geophys. Res.*, *97*(B1), 569–585.

Carson, C. J., S. McLaren, J. L. Roberts, S. D. Boger, and D. D. Blankenship (2013), Hot rocks in a cold place: high sub-glacial heat flow in East Antarctica, *J. Geol. Soc. London*, 1–4, doi:10.1144/jgs2013-030.

Carter, S. P., D. D. Blankenship, M. E. Peters, D. a. Young, J. W. Holt, and D. L. Morse (2007), Radar-based subglacial lake classification in Antarctica, *Geochemistry, Geophys. Geosystems*, *8*(3), doi:10.1029/2006GC001408.

Carter, S. P., D. D. Blankenship, D. A. Young, and J. W. Holt (2009), Using radar-sounding data to identify the distribution and sources of subglacial water: Application to Dome C, East Antarctica, *J. Glaciol.*, *55*(194), 1025–1040, doi:10.3189/002214309790794931.

Chen, J., C. Wilson, D. Blankenship, and B. Tapley (2009), Accelerated Antarctic ice loss from satellite gravity measurements, *Nat. Geosci.*, *2*(12), 859–862, doi:10.1038/ngeo694.

Childers, V., R. Bell, and J. Brozena (1999), Airborne gravimetry: An investigation of filtering, *Geophysics*, *64*(1), 61–69.

Clark, P. U., and J. S. Walder (1994), Subglacial drainage , eskers , and deforming beds beneath the Laurentide and Eurasian ice sheets, *Geol. Soc. Am. Bull.*, *106*, 304–314.

Close, D., H. Stagg, and P. O'Brien (2007), Seismic stratigraphy and sediment distribution on the Wilkes Land and Terre Adélie margins, East Antarctica, *Mar. Geol.*, *239*(1-2), 33–57, doi:10.1016/j.margeo.2006.12.010.

Close, D., A. Watts, and H. Stagg (2009), A marine geophysical study of the Wilkes Land rifted continental margin, Antarctica, *Geophys. J. Int.*, *177*(2), 430–450, doi:10.1111/j.1365-246X.2008.04066.x.

Colwell, J. B., H. M. J. Stagg, N. G. Direen, G. Bernardel, and I. Borissova (2006), The structure of the continental margin off Wilkes Land and Terre Adelie, East Antarctica, in *Antarctica: Contributions to Global Earth Science2*, edited by D. K. Futterer, D. Damaske, G. Kleinschmidt, H. Miller, and F. Tessensohn, pp. 327–340, Springer-Verlag, Berlin.

Cook, C. P. et al. (2013), Dynamic behaviour of the East Antarctic ice sheet during Pliocene warmth, *Nat. Geosci.*, *6*(9), 765–769, doi:10.1038/ngeo1889.

Cooper, A. K. and O'Brien, P. E. (2004), Leg 188 Synthesis: Transitions in the Glacial History of Prydz Bay Region, East Antarctica from ODP drilling, *Proc. Ocean Drill. Program, Sci. Results*, *188*, 1–42.

Damaske, D., F. Ferraccioli, and E. Bozzo (2003), Aeromagnetic anomaly investigations along the Antarctic coast between Yule Bay and Mertz Glacier, *Terra Antart.*, *10*(3), 85–96.

Damiani, T. M., T. A. Jordan, F. Ferraccioli, D. A. Young, and D. D. Blankenship (2014), Variable crustal thickness beneath Thwaites Glacier revealed from airborne gravimetry, possible implications for geothermal heat flux in West Antarctica, *Earth Planet. Sci. Lett.*, *407*, 109–122, doi:10.1016/j.epsl.2014.09.023.

DeConto, R., and D. Pollard (2003), Rapid Cenozoic glaciation of Antarctica induced by declining atmospheric CO2, *Nature*, *421*(6920), 245–249.

Diehl, T. M. (2008), Gravity Analyses for the Crustal Structure and Subglacial Geology of West Antarctica, Particularly Beneath Twaites Glacier, *Univ Texas-Austin PhD Diss.*, 237pp.

Domack, E. W. (1988), Biogenic facies in the Antarctic glaciamarine environment: Basis for a polar glacimarine summary, *Palaeogeogr. Palaeoclimatol. Palaeoecol.*, *63*, 357–372.

Donda, F., G. Brancolini, L. De Santis, and F. Trincardi (2003), Seismic facies and sedimentary processes on the continental rise off Wilkes Land (East Antarctica): evidence of bottom current activity, *Deep Sea Res. Part II Top. Stud. Oceanogr.*, *50*(8-9), 1509–1527, doi:10.1016/S0967-0645(03)00075-4.

Drewry, D. J. (1976), Sedimentary Basins of the East Antarctic Craton from Geophysical Evidence, *Tectonophysics*, *36*, 301–314.

Drewry, D. J. (1983), *Antarctica: Glaciological and Geophysical Folio*, University of Cambridge, Cambridge, UK.

Drinkwater, M., H. R., M. Kern, D. Muzi, and R. Floberghagen (2008), GOCE: Obtaining a portrait of Earth's Most Intimate Features, *ESA Bull.*, *133*, 4–13.

Ehrmann, W. U., H. Grobe, and D. K. Futterer (1991), Ice rafted debris of ODP Hole 119-746A, in *Proceedings of the Ocean Drilling Program, Scientific Results*, edited by J. Barron and B. et al. Larsen, pp. 239–260, Texas A&M University, College Station, TX.

Escutia, C., L. De Santis, F. Donda, R. B. Dunbar, A. K. Cooper, G. Brancolini, and S. L. Eittreim (2005), Cenozoic ice sheet history from East Antarctic Wilkes Land continental margin sediments, *Glob. Planet. Change*, *45*(1-3), 51–81, doi:10.1016/j.gloplacha.2004.09.010.

Escutia, C., M. A. Bárcena, R. G. Lucchi, O. Romero, A. M. Ballegeer, J. J. Gonzalez, and D. M. Harwood (2009), Circum-Antarctic warming events between 4 and 3.5Ma recorded in marine sediments from the Prydz Bay (ODP Leg 188) and the Antarctic Peninsula (ODP Leg 178) margins, *Glob. Planet. Change*, *69*(3), 170–184, doi:10.1016/j.gloplacha.2009.09.003.

Escutia, C., H. Brinkhuis, and A. Klaus (2011), IODP Expedition 318: From Greenhouse to Icehouse at the Wilkes Land Antarctic Margin, *Sci. Drill.*, (12, September 2011), 15–23, doi:10.2204/iodp.sd.12.02.2011.

Escutia, C., Brinkhuis, H., Klaus, A., and the Expedition 318 Scientists, 2011. (2011), Cenozoic East Antarctic Ice Sheet Evolution from Wilkes Land Margin Sediments, in *Integrated Ocean Drilling Program Expedition 318 Scientific Prospectus*, Tokyo, Japan.

Fairhead, J.D. and Okereke, C. S. (1988), Depths to major density contrasts beneath the West African rift system in Nigeria and Camaroon based on the spectral analysis of gravity data, *J. African Earth Sci.*, *7*(5-6), 769–777.

Fanning, C. M., D. H. Moore, V. C. Bennett, S. J. Daly, R. P. Menot, J. J. Peucat, and R. L. Oliver (1999), The Mawson Continent: the East Antarctic Sheld and Gawler Craton, Australia, in *8th International Symposium on Antarctic Earth Sciences*, edited by D. N. B. Skinner, p. 103, Royal Society of New Zealand, Wellington, N. Z.

Featherstone, W. E. (1995), On the use of Australian geodetic datums in gravity field determination, *Aust. J. Geod. Photogramm. Surv.*, *62*, 17–36, doi:10.1108/eb045337.

Ferraccioli, F., F. Coren, and E. Bozzo (2001), Rifted (?) crust at the East Antarctic Craton margin: gravity and magnetic interpretation along a traverse across the Wilkes Subglacial Basin region, *Earth Planet. …*, *192*(3), 407–421.

Ferraccioli, F., T. A. Jordan, A. Armadillo, E. Bozzo, H. Corr, G. Caneva, C. Robinson, N. Frearson, and I. E. Tabacco (2007), Collaborative aerogeophysical campaign targets the Wilkes Subglacial Basin, the Transantarctic Mountains and the Dome C region., in *The Italian-British Antarctic Geophysical and Geological Survey in Northern Victoria Land 2005-06 - Towards the International Polar Year 2007-08*, edited by E. Bozzo and F. Ferraccioli, pp. 1–36, Terra Antarctica Reports.

Ferraccioli, F., E. Armadillo, T. Jordan, E. Bozzo, and H. Corr (2009), Aeromagnetic exploration over the East Antarctic Ice Sheet: a new view of the Wilkes Subglacial Basin, *Tectonophysics*, *478*(1-2), 62–77, doi:10.1016/j.tecto.2009.03.013.

Ferraccioli, F., C. Finn, and T. Jordan (2011), East Antarctic rifting triggers uplift of the Gamburtsev Mountains, *Nature*, *479*(7373), 388–92, doi:10.1038/nature10566.

Filina, I., D. Blankenship, M. Thoma, V. V. Lukin, V. N. Masolov, and M. K. Sen (2008), New 3D bathymetry and sediment distribution in Lake Vostok: Implication for pre-glacial origin and numerical modeling of the internal processes within the lake, *Earth Planet. Sci. Lett.*, *276*(1-2), 106–114, doi:10.1016/j.epsl.2008.09.012.

Filina, I. Y., D. D. Blankenship, L. Roy, M. K. Sen, T. G. Richter, and J. W. Holt (2006), Inversion of airbourne gravity data over subglacial lakes East Antarctica, in *Antarctica: Contributions to Global Earth Science*, pp. 129–133.

Fitzgerald, P. G., and E. Stump (1997), Cretaceous and Cenozoic episodic denudation of the Transantarctic Mountians, Antarctica: New Constraints from apatite fission track thermochronology in the Scott Glacier region, *J. Geophys. Res.*, *102*(B4), 7747–7765.

Von Frese, R. R. B., W. J. Hinze, L. W. Braile, and A. J. Luca (1981), Spherical earth gravity and magnetic anomaly modeling by Gauss-Legendre quadrature integration, *J. Geophys.*, *49*, 234–242.

Fretwell, P. et al. (2013), Bedmap2: improved ice bed, surface and thickness datasets for Antarctica, *Cryosph.*, *7*(1), 375–393, doi:10.5194/tc-7-375-2013.

Galloway, W. E., and T. A. Williams (1991), Sediment accumulation rates in time and space - Paleogene genetic stratigraphic sequences of the Northwestern Gulf of Mexico Basin, *Geology*, *19*(10), 986–989.

Gibson, G. M., J. M. Totterdell, L. T. White, C. H. Mitchell, A. R. Stacey, M. P. Morse, and A. Whitaker (2013), Pre-existing basement structure and its influence on continental rifting and fracture zone development along Australia ' s southern rifted margin, *J. Geol. Soc.*, *170*(2), 365–377, doi:10.1144/jgs2012-040.

Gomez, N., J. X. Mitrovica, M. E. Tamisiea, and P. U. Clark (2010), A new projection of sea level change in response to collapse of marine sectors of the Antarctic Ice Sheet, *Geophys. J. Int.*, *180*(2), 623–634, doi:10.1111/j.1365-246X.2009.04419.x.

Goodge, J. W. (2007), Metamorphism in the Ross Orogen and its bearing on Gondwana margin tectonics, *Geol. Soc. Am. Spec. Pap.*, *419*, 185–203.

Greenbaum, J. S., D. D. Blankenship, D. A. Young, T. G. Richter, J. L. Roberts, and A. R. A. Aitken (2015), Ocean access to a cavity beneath Totten Glacier in, *Nat. Geosci.*, *8*, 294–298, doi:10.1038/NGEO2388.

Gueguen, Y. and Palciauskas, V. (1994), *Introduction to the Physics of Rocks*, Princeton University Press, Princeton, N. J.

Gwyther, D. E., B. K. Galton-Fenzi, J. R. Hunter, and J. L. Roberts (2014), Simulated melt rates for the Totten and Dalton ice shelves, *Ocean Sci.*, *10*(3), 267–279, doi:10.5194/os-10-267-2014.

Hallet, B., L. Hunter, and J. Bogen (1996), Rates of erosion by glaciers_alpine-warm_et al_1996.pdf, *Glob. Planet. Change*, 213–235.

Harwood, D. M. (1986), Diatom biostratigraphy and paleoecology with a Cenozoic History of Antarctic Ice Sheets, Ohio State University.

Le Heron, D. P. (2009), Interpretation of Late Ordovician glaciogenic reservoirs from 3-D seismic data: an example from the Murzuq Basin, Libya, *Geol. Mag.*, *147*(01), 28–41, doi:10.1017/S0016756809990586.

Hill, D.J., Haywood, A.M., Hindmarsh, R.C.A., & Valdes, P. J. (2007), *Deep Time Perspectives on Climate Change*, edited by D. Williams, M., Haywood, A.M., Gregory J., & Schmidt, The Geological Society of London, London.

Holt, J. W., T. G. Richter, S. D. Kempf, D. L. Morse, and D. D. Blankenship (2006), Airborne gravity over Lake Vostok and adjacent highlands of East Antarctica, *Geochemistry, Geophys. Geosystems*, *7*(11), 1–15, doi:10.1029/2005GC001177.

Huuse, M., and H. Lykke-Andersen (2000), Overdeepened Quaternary valleys in the eastern Danish North Sea : morphology and origin, *Quat. Sci. Rev.*, *19*, 1233–1253.

Huybrechts, P. (2002), Sea-level changes at the LGM from ice-dynamical reconstructions of the Greenland and Antarctica ice sheets during the glacial cycles, *Quat. Sci. Rev.*, *21*, 203–231.

IPCC (2013), Climate Change 2013: The physical science basis, in *Contributions of working group 1 to the fifth assessment report of the Intergovernmental Panel on Climate Change*, edited by T. F. Stocker, D. Qin, G. K. Plattner, M. Tignor, S. K. Allen, J. Boschung, A. Naules, Y. Xia, V. Bex, and P. M. Midgley, Cambridge, UK and New York, NY, USA.

Jachens, R.C. and Griscom, J. J. (1985), An Isostatic Residual Gravity Map of California, in *The Utility of Regional Gravity and Magnetic Anomaly Maps*, edited by Hinze, pp. 347–360, SEG Press.

Jamieson, S. S. R., N. R. J. Hulton, and M. Hagdorn (2008), Modelling landscape evolution under ice sheets, *Geomorphology*, *97*(1-2), 91–108, doi:10.1016/j.geomorph.2007.02.047.

Jamieson, S. S. R., D. E. Sugden, and N. R. J. Hulton (2010), The evolution of the subglacial landscape of Antarctica, *Earth Planet. Sci. Lett.*, *293*(1-2), 1–27, doi:10.1016/j.epsl.2010.02.012.

Jamieson, S. S. R., A. Vieli, S. J. Livingstone, C. Ó. Cofaigh, C. Stokes, C. D. Hillenbrand, and J. A. Dowdeswell (2012), Ice-stream stability on a reverse bed slope, *Nat. Geosci.*, *5*(11), 799–802, doi:10.1038/ngeo1600.

Jamieson, S. S. R., C. R. Stokes, and N. Ross (2014), The glacial geomorphology of the Antarctic ice-sheet bed., *Antarct. ...*, *26*(6), 1–38, doi:10.1017/S0954102014000212.

Jordan, T. A., F. Ferraccioli, E. Armadillo, and E. Bozzo (2013), Crustal architecture of the Wilkes Subglacial Basin in East Antarctica, as revealed from airborne gravity data, *Tectonophysics*, *585*, 196–206, doi:10.1016/j.tecto.2012.06.041.

Kane, M. F. (1962), A Comprehensive System of Terrain Corrections using a Digital Computer, *Geophysics*, *27*(4), 455–462.

Karner, G. D., and A. B. Watts (1983), Gravity anomalies and flexure of the lithosphere at mountain ranges, *J. Geophys. Res.*, *88*(B12), 10449–10477, doi:10.1029/JB088iB12p10449.

Kennett, A. J. P., R. E. Houtz, P. B. Andrews, A. R. Edwards, V. A. Gostin, M. Hajos, M. A. Hampton, D. G. Jenkins, S. V Margolis, and A. T. Ovenshine (1974), Development of the Circum-Antarctic Current, *Science (80-.).*, *186*(4159), 144–147.

Kern, M., K. K. P. P. Schwarz, and N. Sneeuw (2003), A study on the combination of satellite, airborne, and terrestrial gravity data, *J. Geod.*, *77*(3-4), 217–225, doi:10.1007/s00190-003-0313-x.

Kilty, K. T. (1983), Werner deconvolution of profile potential field data, *Geophysics*, *1*(2), 234–237.

Kirshner, A. E., J. B. Anderson, M. Jakobsson, M. O’Regan, W. Majewski, and F. O. Nitsche (2012), Post-LGM deglaciation in Pine Island Bay, West Antarctica, *Quat. Sci. Rev.*, *38*, 11–26, doi:10.1016/j.quascirev.2012.01.017.

Koppes, M. N., and D. R. Montgomery (2009), The relative efficacy of fluvial and glacial erosion over modern to orogenic timescales, *Nat. Geosci.*, *2*(9), 644–647, doi:10.1038/ngoe616.

Krassay, A. A., D. L. Cathro, and D. Ryan (2004), A regional tectonostratigraphic framework for the Otway Basin, in *Eastern Australasian Basins Symposium II, Petroleum Exploration Society of Australia, Special Publication*, edited by P. J. Boult, D. R. Johns, and S. C. Lang, pp. 97–116.

Ku, Chao C. & Sharp, J. A. (1983), Werner deconvolution for automated magnetic interpretation and its refinement using Marquardt's inverse modeling, *Geophysics*, *48*(6), 754–774, doi:10.1190/1.1441505.

Kumar, P., X. Yuan, M. R. Kumar, R. Kind, X. Li, and R. K. Chadha (2007), The rapid drift of the Indian tectonic plate., *Nature*, *449*(7164), 894–7, doi:10.1038/nature06214.

LaCoste, L. J. B. (1967), Measurement of gravity at sea and in the air, *Rev. Geophys.*, *5*, 477–526.

LaFehr, T. R. (1991), An exact solution for the gravity curvature (Bullard B) correction, *Geophysics*, *56*(8), 1179–1184, doi:10.1190/1.1443138.

Lambeck, K. (1996), Limits on the areal extent of the Barents Sea ice sheet in Late Weichselian time, *Glob. Planet. Change*, *12*(1-4), 41–51, doi:10.1016/0921-8181(95)00011-9.

Lawrence, J.F., J.W. van Wijk, and N. W. D. (2007), Tectonic Implications for the Uplift of the Transantarctic Mountains, *USGS Natl Acad. Ext. Abstr.*, 1–4.

Lawver, L. A., and L. M. Gahagan (2003), Evolution of Cenozoic seaways in the circum-Antarctic region, *Palaeogeogr. Palaeoclimatol. Palaeoecol.*, *198*(1-2), 11–37, doi:10.1016/S0031-0182(03)00392-4.

Lawver, L. A., L. M. Gahagan, and M. F. Coffin (1992), The development of paleoseaways around Antarctica, in *The Antarctic Paleoenvironment: A Perspective on Global Change, Part 1*, edited by J. P. Kennett and D. A. Warnke, pp. 7–30, American Geophysical Union, Washington, DC.

Leao, J. W. D., P. T. L. Menezes, J. F. Beltrao, and J. B. C. Silva (1996), Gravity inversion of basement relief constrained by knowledge of depth at isolated points, *Geophysics*, *61*, 1702–1714.

Lees, C. H. (1910), On the shapes of the isogeotherms under mountain ranges in radio-active districts, *Proc R. Soc. London Ser. A*, *83*, 339–346.

Leitchenkov, G. L., V. V Gandyukhin, Y. B. Guseva, and A. Y. Kazankov (2007), Crustal structure and evolution of the Mawson Sea , western Wilkes Land margin , East Antarctica, *USGS Short Res. Pap. 028*, 3–6, doi:10.3133/of2007-1047.srp028.

Leventer, A. et al. (2014), *Sabrina Coast Marine Record of Cryosphere-Ocean Dynamics Cruise Report*.

Lisiecki, L. E., and M. E. Raymo (2005), A Pliocene-Pleistocene stack of 57 globally distributed benthic O18 records, *Paleoceanography2*, *20*, PA1003, doi:10.1029/2004PA001071.

Lisker, F. (2002), Review of fission track studies in northern Victoria Land, Antarctica - passive margin evolution versus uplift of the Transantarctic Mountains, *Tectonophysics*, *349*(1-4), 57–73.

Lloyd, A. J., A. A. Nyblade, D. A. Wiens, S. E. Hansen, M. Kanao, P. J. Shore, and D. Zhao (2013), Upper mantle seismic structure beneath central East Antarctica from body wave tomography: Implications for the origin of the Gamburtsev Subglacial Mountains., *Geochemistry, Geophys. Geosystems*, *14*(4), 902–920, doi:10.1002/ggge.20098.

Llubes, M., C. Lanseau, and F. Rémy (2006), Relations between basal condition, subglacial hydrological networks and geothermal flux in Antarctica, *Earth Planet. Sci. Lett.*, *241*(3-4), 655–662, doi:10.1016/j.epsl.2005.10.040.

Lythe, M. B., and D. G. Vaughan (2001), BEDMAP- A new ice thickness and subglacial topographic model of Antarctica, *J. Geophys. Res.*, *106*(B6), 11335–11351.

McMillan, M., H. Corr, A. Shepherd, A. Ridout, S. Laxon, and R. Cullen (2013), Three-dimensional mapping by CryoSat-2 of subglacial lake volume changes, *Geophys. Res. Lett.*, *40*(16), 4321–4327, doi:10.1002/grl.50689.

Mengel, M., and A. Levermann (2014), Ice plug prevents irreversible discharge from East Antarctica, *Nat. Clim. Chang.*, *4*(6), 451–455, doi:10.1038/nclimate2226.

Mercer, J. H. (1978), West Antarctic ice sheet and CO2 greenhouse effect: a threat of disaster, *Nature*, *271*, 321–325.

Miller, K. G., J. D. Wright, J. V. Browning, a. Kulpecz, M. Kominz, T. R. Naish, B. S. Cramer, Y. Rosenthal, W. R. Peltier, and S. Sosdian (2012), High tide of the warm Pliocene: Implications of global sea level for Antarctic deglaciation, *Geology*, *40*(5), 407–410, doi:10.1130/G32869.1.

Minty, B. R. S. (1991), Simple micro-leveling for aeromagnetic data, *Explor. Geophys.*, *22*, 591.

Mitchell, N. C., and J. E. H. Clarke (1994), Classification of seafloor geology using multibeam sonar data from the Scotian Shelf, *Mar. Geol.*, *121*(3-4), 143–160, doi:10.1016/0025-3227(94)90027-2.

Morgan, W. J. (1971), Convenction plumes in the lower mantle, *Nature*, *203*(5288), 42–43.

Muller, R. D. and Smith, H. F. (1993), Deformation of the Oceanic Crust Between the North American and South American Plates, *J. Geophys. Res.*, *98*(B5), 8275–8291.

Nagy, D. (1966), The Prism Method for Terrain Corrections using Digital Computers, *Pure Appl. Geophys.*, *63*, 31–39.

Naish, T. R. et al. (2001), Orbitally induced oscillations in the East Antarctic ice sheet at the Oligocene/Miocene boundary., *Nature*, *413*(6857), 719–723, doi:10.1038/35099534.

Nowicki, S. et al. (2013), Insights into spatial sensitivities of ice mass response to environmental change from the SeaRISE ice sheet modeling project I: Antarctica, *J. Geophys. Res. Earth Surf.*, *118*, 1002–1024.

Nyblade, A. A. (1999), Heat flow and the structure of Precambrian lithosphere, *Dev. Geotecton.*, *24*(C), 81–91, doi:10.1016/S0419-0254(99)80006-8.

Oldenburg, D. W. (1974), The Inversion and Interpretation of Gravity Anomalies, *Geophysics*, *39*(4), 526–536.

Orsi, H., T. Whitworth III, and W. D. Nowlin Jr. (1995), On the meridional extent and fronts of the Antarctic Circumpolar Current Pronounced meridional gradients in surface properties separate waters of the Southern Ocean from the warmer and saltier waters of the subtropical circulations . Deacon (1933 , the S, *Deep Sea Res. I*, *42*(5), 641–673.

Orsi, T. H., and D. A. Dunn (1991), Correlations between Sound Velocity and Related Properties of Glacio-Marine Sediments : Barents Sea, *Geo-Marine Lett.*, *11*, 79–83.

Parker, R. L. (1973), The Rapid Calculation of Potential Anomalies, *Geophys. J. R. Astr. Soc.*, *31*, 447–455.

Pearson, P. N., and M. R. Palmer (2000), Atmospheric carbon dioxide concentrations over the past 60 million years, *Nature*, *406*, 695–699.

PEIComp (2004), *Program for calculation of the coefficients used for magnetic compensation*, PicoEnvirotec Inc., Concord, Ontario, Canada.

Peters, L. E., S. Anandakrishnan, R. B. Alley, J. P. Winberry, D. E. Voight, A. M. Smith, and D. L. Morse (2006), Subglacial sediments as a control on the onset and location of two Siple Coast ice streams, West Antarctica, *J. Geophys. Res.*, *111*(B01302), DOI: 10.1029/2005JB003766.

Peters, M., and D. Blankenship (2007), Along-track focusing of airborne radar sounding data from West Antarctica for improving basal reflection analysis and layer detection, *IEEE Trans. Geosci. Remote Sens.*, *45*(9), 2725–2736.

Peters, M. E. (2005), Analysis techniques for coherent airborne radar sounding: Application to West Antarctic ice streams, *J. Geophys. Res.*, *110*(B6), B06303, doi:10.1029/2004JB003222.

Peucat, J. J., R. P. Menot, O. Monnier, and C. M. Fanning (1999), The Terre Adelie basement in the East-Antarctica Shield: geological and isotopic evidence for a major 1.7 Ga thermal event; comparison with the Gawler Craton in South Australia, *Precambrian Res.*, *94*, 205–224.

Pinet, P. R. (2013), *Invitation to Oceanography*, 6th editio., Jones & Bartlett, Sudbury, MA.

Pollard, D., and R. M. DeConto (2009), Modelling West Antarctic ice sheet growth and collapse through the past five million years., *Nature*, *458*(7236), 329–332, doi:10.1038/nature07809.

Pollard, D., R. M. DeConto, and A. A. Nyblade (2005), Sensitivity of Cenozoic Antarctic ice sheet variations to geothermal heat flux, *Glob. Planet. Change*, *49*(1-2), 63–74, doi:10.1016/j.gloplacha.2005.05.003.

Pollard, D., R. M. DeConto, and R. B. Alley (2015), Potential Antarctic Ice Sheet retreat driven by hydrofracturing and ice cliff failure, *Earth Planet. Sci. Lett.*, *412*, 112–121, doi:10.1016/j.epsl.2014.12.035.

Powell, R. D. (1984), Glacimarine processes and inductive lithofacies modelling of ice shelf and tidewater glaciers sediments based on Quaternary examples, *Mar. Geol.*, *57*, 1–52.

Pritchard, H. D., S. R. M. Ligtenberg, H. A. Fricker, D. G. Vaughan, M. R. van den Broeke, and L. Padman (2012), Antarctic ice-sheet loss driven by basal melting of ice shelves., *Nature*, *484*(7395), 502–5, doi:10.1038/nature10968.

Rayne, T. W. and E. W. Domack (1996), Porewater chemistry of Ross Sea diamictons: a till or not a till?, *Antarct. J. United States*, *31*(2), 97–98.

Reading, A. (2004), The seismic structure of Wilkes Land/Terre Adelie, East Antarctica and comparison with Australia: first steps in reconstructing the deep lithosphere of Gondwana, *Gondwana Res.*, (1), 21–30.

Richter, T., J. Holt, and D. Blankenship (2001), Airborne gravity over East Antarctica, in *Proc Intl Symposium Kinematic Systems Geodesy, Geomatics, Navigation*, pp. 576–585, Banff, Alberta, Canada.

Ritz, C., V. Rommelaere, and C. Dumas (2001), Moeling the evolution of Antarctic ice sheet over the last 420,000 years: implications for altitude changes in the Vostok region, *J. Geophys. Res.*, *106*(D23), 31943–31964.

Roland, N. W. (1991), The boundary of the East Antarctic craton on the Pacific margin, in *Geological Evolution of Antarctica*, edited by M. R. A. Thomson, J. A. Crame, and J. W. Thomson, pp. 161–165, Cambridge Univ. Press, New York, NY.

Roy, L., M. Sen, D. Blankenship, P. Stoffa, and T. Richter (2005), Inversion and uncertainty estimation of gravity data using simulated annealing: An application over Lake Vostok, East Antarctica, *Geophysics*, *70*(1), 1–12.

Royer, J., and N. Rollet (1997), Plate tectonic setting of the Tasmanian region, *Aust. J. Earth Sci.*, *44*(5), 543–560, doi:10.1080/08120099708728336.

Sayers, J., P. A. Symonds, N. G. Direen, and G. Bernardel (2001), Nature of the continent-ocean transition on the non-volcanic rifted margin of the central Great Australian Bight., in *Continental Margins: a comparison of evidence from land and sea*, edited by R. C. L. Wilson, R. B. Whitmarsh, B. Taylor, and N. Froitzheim, pp. 51–77, Geological Society of London.

Scambos, T. A., T. M. Haran, M. A. Fahnestock, T. H. Painter, and J. Bohlander (2007), MODIS-based Mosaic of Antarctica (MOA) data sets: Continent-wide surface morphology and snow grain size, *Remote Sens. Environ.*, *111*(2-3), 242–257, doi:10.1016/j.rse.2006.12.020.

Schoof, C. (2007), Pressure-dependent viscosity and interfacial instability in coupled ice–sediment flow, *J. Fluid Mech.*, *570*, 227, doi:10.1017/S0022112006002874.

Schroeder, D. M., D. D. Blankenship, and D. A. Young (2013), Evidence for a water system transition beneath Thwaites Glacier, West Antarctica., *Proc. Natl. Acad. Sci. U. S. A.*, *110*(30), 12225–12228, doi:10.1073/pnas.1302828110.

Schroeder, D. M., D. D. Blankenship, D. A. Young, A. E. Witus, and J. B. Anderson (2014), Airborne radar sounding evidence for deformable sediments and outcropping bedrock beneath Thwaites Glacier, West Antarctica, *Geophys. Res. Lett.*, *41*, 7200–7208, doi:10.1002/2014GL061645.Received.

Shepard, M. K., B. A. Campbell, M. H. Bulmer, T. G. Farr, L. R. Gaddis, and J. J. Plaut (2001), A planetary and remote sensing perspective, *J. Geophys. Res.*, *106*(E12), 777–795.

Shevenell, A. E., J. P. Kennett, and D. W. Lea (2004), Middle Miocene Southern Ocean cooling and Antarctic cryosphere expansion, *Science (80-.).*, *305*(5691), 1766–1770, doi:10.1126/science.1100061.

Shevenell, A. E., J. P. Kennett, and D. W. Lea (2008), Middle Miocene ice sheet dynamics, deep-sea temperatures, and carbon cycling: A Southern Ocean perspective, *Geochemistry, Geophys. Geosystems*, *9*(2), doi:10.1029/2007GC001736.

Siegert, M. J., and J. A. Dowdeswell (1996), Spatial variations in heat at the base of the Antarctic ice sheet from analysis of the thermal regime above subglacial lakes, *J. Glaciol.*, *42*, 501–509.

Siegert, M. J., J. Taylor, A. J. Payne, and B. Hubbard (2004), Macro-scale bed roughness of the siple coast ice streams in West Antarctica, *Earth Surf. Process. Landforms*, *29*(13), 1591–1596, doi:10.1002/esp.1100.

Siegert, M. J., S. Carter, I. Tabacco, S. Popov, and D. D. Blankenship (2005), A revised inventory of Antarctic subglacial lakes, *Antarct. Sci.*, *17*(03), 453–460, doi:10.1017/S0954102005002889.

Siegert, M. J., P. Barrett, R. DeConto, R. Dunbar, C. Ó Cofaigh, S. Passchier, and T. Naish (2008), Recent advances in understanding Antarctic climate evolution, *Antarct. Sci.*, *20*(04), 313–325, doi:10.1017/S0954102008000941.

Smith, B. E., A. Fricker, Helen, R. Joughin, Ian, and T. Slawek (2009), An inventory of active subglacial lakes in Antarctica detected by ICESat (2003-2008, *J. Glaciol.*, *55*(192), 573–595, doi:10.3189/002214309789470879.

Spector, A. and Grant, F. S. (1970), Statistical Models for interpreting aeromagnetic data, *Geophysics*, *35*, 293–302.

Steed, R. H. N. (1983), Structural Interpretation of Wilkes Land, Antarctica, in *Antarctic Earth Science - Proc. Fourth Int. Symp. Antarct. Earth Sci.*, edited by J. B. Oliver, R.I., James, P.R., and Jago, pp. 567–572, Cambridge University Press, New York, NY.

Stern, T. A., and U. S. ten Brink (1989), Flexural uplift of the Transantarctic Mountains, *J. Geophys. Res.*, *94*(2), 10315–10330.

Storey, B. C., A. P. M. Vaughan, and T. R. Riley (2013), The links between large igneous provinces, continental break-up and environmental change: evidence reviewed from Antarctica, *Earth Environ. Sci. Trans. R. Soc. Edinburgh*, *104*(01), 17–30, doi:10.1017/S175569101300011X.

Stroud, A.H. and Secrest, D. (1966), *Gaussian quadrature formulas*, Prentice Hall, Englewood Cliffs, NJ.

Studinger, M., R. E. Bell, W. R. Buck, G. D. Karner, and D. D. Blankenship (2004), Sub-ice geology inland of the Transantarctic Mountains in light of new aerogeophysical data, *Earth Planet. Sci. Lett.*, *220*(3-4), 391–408, doi:10.1016/S0012-821X(04)00066-4.

Stump, E., and P. G. Fitzgerald (1992), Geology Episodic uplift of the Transantarctic Mountains, *Geology*, *20*, 161–164, doi:10.1130/0091-7613(1992)020<0161.

Sugden, D. E., D. R. Marchant, N. Potter Jr., R. A. Souchez, G. H. Denton, C. C. Swisher III, and J.-L. Tison (1995), Preservation of Miocene glacier ice in East antarctica, *Nature*, *376*, 412–414.

Tabacco, I. E., P. Cianfarra, a. Forieri, F. Salvini, and a. Zirizotti (2006), Physiography and tectonic setting of the subglacial lake district between Vostok and Belgica subglacial highlands (Antarctica), *Geophys. J. Int.*, *165*(3), 1029–1040, doi:10.1111/j.1365-246X.2006.02954.x.

Talwani, M., and M. Ewing (1960), Rapid computation of gravitational attraction of three-dimensional bodies of arbitrary shape., *Geophysics*, *25*, 203–225.

Thomas, R. H. (1979), The dynamics of marine ice sheets, *J. Glaciol.*, *24*, 167–177.

Tikku, A. A., and S. C. Cande (1999), The oldest magnetic anomalies in the Australian-Antarctic Basin: Are they isochrons?, *J. Geophys. Res. Earth*, *104*(B1), 661–677.

Timmerman, R. et al. (2010), A consistent dataset of Antarctic ice sheet topography, cavity geometry, and global bathymetry, , 261–273, doi:10.5194/essdd-3-231-2010.

Turcotte, D. L. (1997), *Fractals and Chaos in Geology and Geophysics*, 2nd Editio., Cambridge Univ. Press, Cambridge, UK.

Vallient, H. D. (1992), *LaCoste and Romberg Air/Sea Meters: An Overview*, 2nd ed., CRC Press, London, U.K.

Van der Veen, C. J., T. Leftwich, R. von Frese, B. M. Csatho, and J. Li (2007), Subglacial topography and geothermal heat flux: Potential interactions with drainage of the Greenland ice sheet, *Geophys. Res. Lett.*, *34*(12), 1–5, doi:10.1029/2007GL030046.

Veevers, J. J. (2000), Permian-Triassic Pangean basins and foldbelts along the Panthalassan margin of Gondwawa, in *Billion-year earth history of Australia and neighbors in Gondwanaland*, edited by J. J. Veevers, pp. 292–308, GEMOC Press - Macquarie Univ., New South Wales, Australia.

Veevers, J. J. (2012), Reconstructions before rifting and drifting reveal the geological connections between Antarctica and its conjugates in Gondwanaland, *Earth-Science Rev.*, *111*(3-4), 249–318, doi:10.1016/j.earscirev.2011.11.009.

Watson, D. (1992), *Contouring: A Guide to the Analysis and Display of Spatial Data*, Pergamon.

Watts, A. (2001), *Isostasy and Flexure of the Lithosphere*, Cambridge University Press, Cambridge, UK.

Webb, P. N., D. M. Harwood, B. C. McKelvey, J. H. Mercer, and L. D. Stott (1984), Cenozoic marine sedimentation and ice-volume variation on the East Antarctic craton, *Geology*, *12*, 287–291.

Wessel, P., and W. H. F. Smith (1998), New, improved version of generic mapping tools released, *Eos, Trans. Am. Geophys. Union*, *79*, 579–579, doi:10.1029/98EO00426.

White, L. T., G. M. Gibson, and G. S. Lister (2013), A reassessment of paleogeographic reconstructions of eastern Gondwana: Bringing geology back into the equation, *Gondwana Res.*, *24*(3-4), 984–998, doi:10.1016/j.gr.2013.06.009.

White, R. S., and D. P. McKenzie (1989), Magmatism at rift zones: the generation of volcanic continental margins and flood basalts, *J. Geophys. Res. Solid Earth*, *94*(B6), 7685–7729.

Whittaker, J. M., R. D. Müller, G. Leitchenkov, H. Stagg, M. Sdrolias, C. Gaina, and a Goncharov (2007), Major Australian-Antarctic plate reorganization at Hawaiian-Emperor bend time., *Science*, *318*(5847), 83–6, doi:10.1126/science.1143769.

Van Wijk, J. W., J. F. Lawrence, and N. W. Driscoll (2008), Formation of the Transantarctic Mountains related to extension of the West Antarctic Rift system, *Tectonophysics*, *458*(1-4), 117–126, doi:10.1016/j.tecto.2008.03.009.

Williams, R. S., and D. K. Hall (1993), Glaciers, in *Atlas of Satellite Observations Related to Global Change*, edited by R. J. Gurney, J. L. Foster, and C. L. Parkinson, pp. 401–422, Cambridge University Press, London, U.K.

Wingham, D. J., M. J. Siegert, A. Shepherd, and A. S. Muir (2006), Rapid discharge connects Antarctic subglacial lakes., *Nature*, *440*(7087), 1033–1036, doi:10.1038/nature04660.

Winsborrow, M. C. M., C. D. Clark, and C. R. Stokes (2010), What controls the location of ice streams?, *Earth-Science Rev.*, *103*(1-2), 45–59, doi:10.1016/j.earscirev.2010.07.003.

Witus, A. E., C. M. Branecky, J. B. Anderson, W. Szczuciński, D. M. Schroeder, D. D. Blankenship, and M. Jakobsson (2014), Meltwater intensive glacial retreat in polar environments and investigation of associated sediments: example from Pine Island Bay, West Antarctica, *Quat. Sci. Rev.*, *85*, 99–118, doi:10.1016/j.quascirev.2013.11.021.

Wright, A., and M. Siegert (2012), A fourth inventory of Antarctic subglacial lakes, *Antarct. Sci.*, *24*(06), 659–664, doi:10.1017/S095410201200048X.

Wright, A. P. et al. (2012), Evidence of a hydrological connection between the ice divide and ice sheet margin in the Aurora Subglacial Basin, East Antarctica, *J. Geophys. Res.*, *117*(F1), F01033, doi:10.1029/2011JF002066.

Wright, A. P., D. A. Young, J. L. Bamber, J. A. Dowdeswell, A. J. Payne, D. D. Blankenship, and M. J. Siegert (2014), Subglacial hydrological connectivity within the Byrd Glacier catchment, East Antarctica, *J. Glaciol.*, *60*(220), 345–352, doi:10.3189/2014JoG13J014.

Wright, A. and Siegert, M. J. (2011), The identification and physiographical setting of Antarctic subglacial lakes, in *Antarctic Subglacial Aquatic Environments*, pp. 9–26.

Young, D. A. et al. (2011), A dynamic early East Antarctic Ice Sheet suggested by ice-covered fjord landscapes., *Nature*, *474*(7349), 72–5, doi:10.1038/nature10114.

Zachos, J. C., N. J. Shackleton, J. S. Revenaugh, H. Pa, and B. P. Flower (2001), Climate Response to Orbital Forcing Across the Oligocene-Miocene Boundary, *Science (80-.).*, *292*, 274–278.

Zoback, M. D. (2010), *Reservoir Geomechanics*, Cambridge University Press, Cambridge, UK.

Vita

Bruce Child Frederick was born in Houston, Texas in February 1969 to John and Laverne Frederick. He was raised on St. Croix, US Virgin Islands with his sister, Paige Frederick-Pape where they attended the Good Hope School. Bruce graduated high school from Choate-Rosemary Hall in Wallingford, Connecticut where he competed on the men's varsity volleyball and crew teams. Bruce consistently made the Dean's List and was awarded the Coach's Award in men's crew before graduating from high school and attending Colgate University in Hamilton, New York. While at Colgate, Bruce was an instructor in the Outdoor Recreation Department where he led guided collegiate expeditions into the Adirondack Wilderness and surrounding areas of upstate New York. He was also very active in the Geology Department, volunteering for field research opportunities with Syracuse University, Hamilton College and Colgate University to the Boreal Peatlands of Northern Minnesota and the fjord-dominated landscape of the Antarctic Peninsula.

Bruce graduated with a bachelor's degree and high honors in geology from Colgate University in May 1991 after publishing his honors thesis on "Magnetic susceptibility measurements in Antarctic glacial-marine sediment from in front of the Muller Ice Shelf-Antarctic Peninsula". He subsequently attended the University of Miami – Rosentiel School for Marine and Atmospheric Sciences where he earned a Master of Science degree in May 1994 based upon his stratigraphic analysis of the Broad-Lostman's region in Everglades National Park.

Following more than a decade in the environmental consulting and financial services sectors, Bruce returned to Antarctic science and academia to pursue a PhD in geophysics with Dr. Donald D. Blankenship. While at the University of Texas-Austin, Bruce has had the pleasure to serve as treasurer and volunteer coordinator for the UT Geophysical Society and to teach two semesters of laboratory-based undergraduate geology classes, in addition to completion of the research presented in this dissertation.

Permanent address: 125 Harbor Ridge, Bath, Maine 04530

This dissertation was typed by Bruce Child Frederick.